Bacterial nanowires of *Shewanella oneidensis* MR-1: electron transport mechanism, composition, and role of multiheme cytochromes

by

Sahand Pirbadian

A Dissertation Presented to the
FACULTY OF THE GRADUATE SCHOOL
UNIVERSITY OF SOUTHERN CALIFORNIA
In Partial Fulfillment of the
Requirements for the Degree
DOCTOR OF PHILOSOPHY
(PHYSICS)

May 2015

ProQuest LLC.
789 East Eisenhower Parkway
P.O. Box 1346
Ann Arbor, MI 48106 - 1346

To my lovely wife, Pouye

Acknowledgments

I'd like to use this opportunity to thank my advisor and role model, Moh El-Naggar, who is both a wonderful person and a great mentor. Moh has inspired me in so many ways during my four years in his group and for that I will be forever in his debt. He has introduced me to an exciting subject, and has given me encouranegment to explore in the lab. He has always been extremely supportive, patient and positive which has especially helped me when things didn't go as planned. Moh, I don't think I can thank you enough! I wish long and healthy lives full of joy for you and your family.

I would like to thank all my labmates, I could never wish for a better group of people to work with and be around: Tom Yuzvinsky, Edmond (Kar Man) Leung, Matt (Shuai) Xu, Ben Gross, Ian McFarlane, Yamini Jangir and Hyesuk Byun. Thanks for always being helpful, supportive and cheerful!

I truly appreciate all the help and guidance that I received from Sarah Barchinger and John Golbeck during our work together. I hope we can continue our collaborations for years to come.

My special gratitude goes to the USC Center of Excellence in NanoBiophysics and the USC Center for Electron Microscopy and Microanalysis (CEMMA), and especially Paul Webster, formerly at USC and currently at Oak Crest Institute of Science, for preparation of TEM samples and TEM imaging.

Also, I would like to thank my collaborators Liang Shi, Rachida Bouhenni, Daad Saffarini, Bree Reed, Margie Romine, and Yuri Gorby for their help in the nanowire characterization project reported in this thesis.

I'm grateful to my parents, Parisima Parsaei and Ali Pirbadian, for their unconditional love and support and for introducing me to science and the wonderful joy in learning since my early childhood.

And most importantly, I thank my best friend, my life companion, my beautiful wife Pouye. Meeting you was the best thing that has ever happened to me and you have filled every day of my life with joy since that day. During my years in grad school, you have always been supportive, understanding and helpful. Words cannot express how grateful I am to have you as my wife and I look forward to spending the rest of my life by your side.

Last but not least, I would like to acknowledge the funding agencies that helped make this thesis happen: the Air force Office of Scientific Research (Young Investigator Research Program Grant FA9550-10-1-0144 to Moh El-Naggar) and the US Department of Energy (Grant DE-FG02-13ER16415 to Moh El-Naggar). I am also grateful to the graduate school at USC for their generous Provost Fellowship during my last two years in grad school.

Contents

Abstract

In this thesis, we discuss three topics concerning extracellular electron transfer in the Dissimilatory Metal Reducing Bacterium (DMRB) *Shewanella oneidensis* MR-1. One proposed strategy to accomplish extracellular charge transfer in *Shewanella* involves forming a conductive pathway to electrodes by incorporating redox components on outer cell membranes and along extracellular appendages known as bacterial nanowires within biofilms. In the first part of this dissertation, to describe extracellular charge transfer in microbial redox chains, we employed a model based on incoherent hopping between sites in the chain and an interfacial treatment of electrochemical interactions with the surrounding electrodes. Based on this model, we calculated the current-voltage (I-V) characteristics and found the results to be in good agreement with I-V measurements across and along individual microbial nanowires produced by the bacterium *S. oneidensis* MR-1. Based on our analysis, we propose that multistep hopping in redox chains constitutes a viable strategy for extracellular charge transfer in microbial biofilms.

In the second part, we report the first *in vivo* observations of the formation and respiratory impact of nanowires in the model metal-reducing microbe *S. oneidensis* MR-1. Live fluorescence measurements, immunolabeling, and quantitative gene expression analysis point to *S. oneidensis* MR-1 nanowires as extensions of the

outer membrane and periplasm that include the multiheme cytochromes responsible for EET, rather than pilin-based structures as previously thought. These membrane extensions are associated with outer membrane vesicles, structures ubiquitous in Gram-negative bacteria, and are consistent with bacterial nanowires that mediate long-range EET by our proposed multistep redox hopping mechanism. Redox-functionalized membrane and vesicular extensions may represent a general microbial strategy for electron transport and energy distribution.

In addition, to elucidate the membranous nature of *Shewanella* nanowires, we imaged these filaments using Transmission Electron Microscopy. The TEM images reported in this thesis also provide the most accurate estimates of bacterial nanowire dimensions to date. Future TEM and cryo-TEM imaging can establish the specific alignment and configuration of outer membrane cytochromes that facilitate electron transport along bacterial nanowires.

In the third part of this thesis, we focus on the molecular conductance of MtrF, the first decaheme outer membrane cytochrome with a solved crystal structure. Decaheme outer membrane cytochromes of *Shewanella* play a crucial role in all the suggested pathways of extracellular electron transfer. An understanding of the electron transfer properties in MtrF will therefore impact all aspects of extracellular electron transfer research. In this thesis, using purified MtrF, we form monolayers of the protein on atomically flat gold substrates and address the dry monolayer with a Scanning Tunneling Microscope (STM) tip. This technique can be used in the future to examine the conductivity of individual MtrF molecules within the monolayer in the form of I-V curves. This methodology will allow experimental comparison with recently developed simulations of MtrF conductance.

Chapter 1

Introduction

Electron transfer plays an important role in our everyday lives, most visibly in all solid state devices that we regularly use. But what may not be clear to many is that electron transfer is one of the most fundamental and crucial phenomena in sustaining life [1, 2]. In fact it is the flow of electrons that drives the energetics of life. In respiratory organisms, higher energy electrons start from an electron donor and move along several steps into and through a living cell and reach their destination, an electron acceptor. But what does life gain from escorting electrons from one molecule to another? The same way energy is harvested from water in a turbine in a dam, flowing electrons through living cells can give energy to organisms to sustain their lively functions [3].

In respiration, the electron flow in a cell is channeled through a series of molecules in the cellular inner membrane (or in the case of eukaryotes the mitochondrial inner membrane). A proton gradient is then created across the inner membrane, and is used to generate Adenosine Triphosphate (ATP), the energy currency of life [3]. ATP can later be used for various functions including biosynthesis and transportation of molecules in and out of cells. Although alternative strategies such as substrate level phosphorylation (SLP) can be the primary source of ATP production in some organisms under certain conditions (including in *Shewanella* [4]), electron transfer to electron acceptors must still continue to ensure that redox reactions in the cell are balanced.

While most organisms use some form of electron transport from an electron donor to an electron acceptor to store energy in the form of ATP, the specifics of the pathways for this process and the electron donors/acceptors used vary in nature. Aerobic organisms transfer the electrons generated by oxidizing organic molecules (their electron donor) to molecular oxygen available in soluble form inside the cell. Therefore aerobic organisms including humans require molecular oxygen to produce ATP and survive. Anaerobic organisms, on the other hand, are able to use alternative electron acceptors other than molecular oxygen to sustain the flow of electrons. Examples of anaerobic organisms are the bacteria that thrived on the Earth before the atmosphere had enough molecular oxygen to sustain aerobic life. In fact species of microbes exist today that have the same ability, *i.e.* to survive under anaerobic conditions. But the question is what do these microbes use instead of molecular oxygen as their electron acceptor?

Long before accumulation of molecular oxygen in the Earth atmosphere, iron and other metals would have served as terminal electron acceptors for microorganisms [5]. But to be able to reduce insoluble inorganic minerals such as iron oxide based rocks, a cell requires the machinery to transport its respiratory electrons outside the cellular outer membrane and perform extracellular electron transfer (EET). Dissimilatory metal-reducing bacteria (DMRBs) are the group of microbes existing on Earth today that have the capability of EET [6, 7].

The first DMRBs, *Geobacter* and *Shewanella* (Fig. 1.1), were discovered in the late 1980s [8–10], thus beginning the search into the mechanisms of extracellular electron transfer and understanding the long-range electron transport required to move electrons to cellular exterior for reduction of solid phase metal oxides. It was later discovered that multi-heme cytochromes (such as the one in Fig. 1.2) play a crucial role in enabling this long-range transport [11–14]. These proteins

Figure 1.1: Image of *Shewanella oneidensis* MR-1 cells on Fe_2O_3. Image credit: Alice Dohnalkova, Pacific Northwest National Lab, Richland, WA.

incorporate multiple electron carrier heme sites within their structure (Fig. 1.2). In fact periplasmic and outer membrane cytochromes form a complex along which electrons can move and cross the cellular membrane [14, 15]. Due to the central role of these multiheme cytochromes in extracellular electron transport, they have been the subject of numerous studies in the past two decades [12, 14–19].

Extracellular electron transfer has gathered a large amount of interest in the past few decades due to its applications in renewable energy conversion [20, 21], bioremediation [22, 23], and waste water treatment [24]. DMRBs are not only capable of reducing metal oxide rocks in the environment, but they are able to transfer electrons to synthetic solid state electrodes [25]. By providing enough

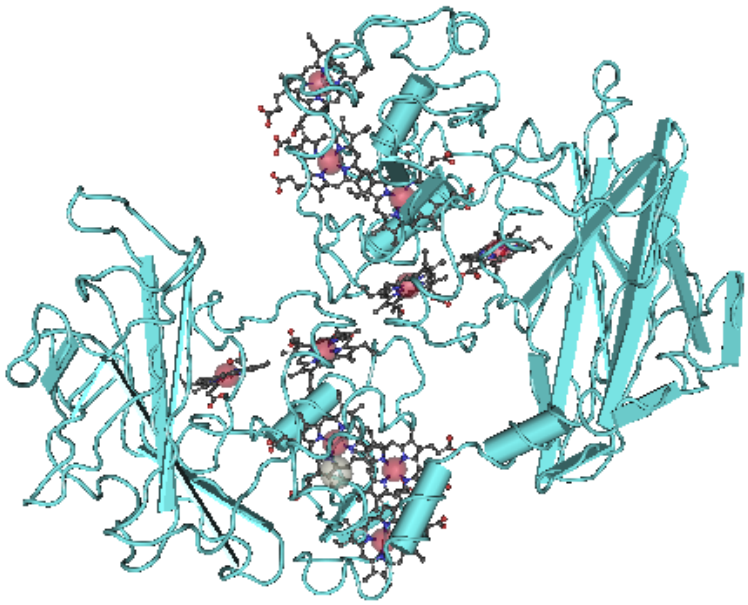

Figure 1.2: Crystal structure of MtrF, a decaheme outer membrane cytochrome of *S. oneidensis* MR-1. The hemes in this structure are positioned according to a 'staggered-cross' pattern. The small (<1nm) distance between adjacent hemes enables long range electron transfer in this outer membrane cytochrome [17].

soluble electron donor and tuning the redox potential of the electrode, the flow of respiratory electrons and therefore the cellular metabolism and growth can be controlled. As a result, a steady flow of electrons can be extracted and converted to electricity from a community of cells in microbial fuel cells (MFCs) [20] (Fig. 1.3). Another application of EET is microbial electrosynthesis in which bacteria perform the above process in reverse: they gain electrons generated by renewable energy sources such as solar cells to reduce soluble chemicals, resulting in the synthesis of biofuels [26].

DMRBs are also used for bioremediation by reducing soluble toxic chemicals that become insoluble upon reduction. Examples of such toxins are chromium or

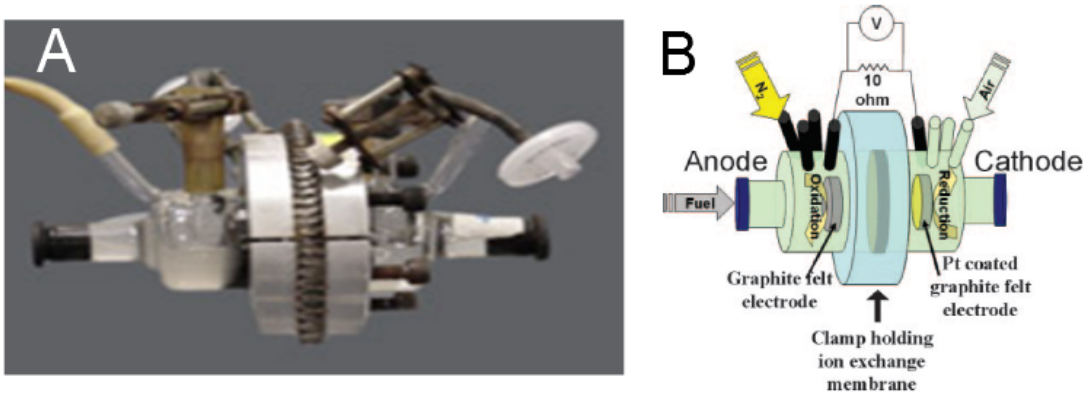

Figure 1.3: A) Photo and B) schematic of a microbial fuel cell (MFC). MFCs are are able to convert renewable energy from organic matter (or possibly organic contaminants) using dissimilatory metal-reducing bacteria such as *Shewanella* and *Geobacter*. In this dual-compartment MFC, bacteria are introduced in the anode compartment, they attach to the anode and transfer their respiratory electrons to it. These electrons are transferred to the cathode compartment, where oxygen is reduced to produce water. The separating membrane between the two compartments allows transfer of protons from the anode to the cathode compartment which completes the cell reaction. From [20].

uranium, soluble contaminants in water which become insoluble upon reduction by bacteria and therefore can be easily removed from water [22]. In addition, since waste water has a high organic content, DMRBs can be used for its treatment and for simultaeous production of electricity [24].

Research on extracellular electron transport may also have implications for astrobiology and the search for extraterrestrial life. Some of the minerals that MR-1 is known to use as electron acceptor are very abundant on other planets, *e.g.* iron oxides on the surface of Mars [27]. Thus a better understanding of the mechanisms of extracellular electron transport in DMRBs may familiarize us with possible extraterrestrial metabolisms on other planets including Mars.

The amazing level of sophistication in the design and manufacturing of the semiconductor devices we use every day is partially due to our deep quantitative

understanding of movements and flows of electrons in these devices. Similarly, quantitative knowledge of electron transfer processes in biology is essential in our ability to enhance and tap the energy conversion potential of living cells. The non-adiabatic electron transfer theory has typically been the starting point for any physical model of biological electron transfer in the past half century [28]. This semi-classical theory describes how electrons are transferred from a donor site to an acceptor site in solution and was later modified to also include quantum mechanical effects [2, 29]. This theory has been tested for systems in which the distance between the donor and acceptor is fixed, resulting in timetables for rates of electron transfer in various environments.

However, until about two decades ago investigation of biological electron transfer was limited to ET reactions occurring at nanometer length scales. The recent emergence of EET measurements in DMRBs has indicated the possibility of electron transfer phenomena in microns-long structures [30–33]. Therefore, the additional complexity of these larger scale systems calls for more intricate quantitative models that are still based on the fundamental theory of electron transfer, *i.e.* Marcus theory. For instance, rather than having a single step electron hopping event between a donor and an acceptor site, one may need to account for tens or hundreds of hopping events to model a single EET process [34].

Understanding the ET properties of individual multiheme cytochromes can serve as an important stepping-stone to the study of EET as a whole. For this reason, there has been a large amount of interest in physical modeling of EET in DMRBs in recent years [34–36]. Outer membrane cytochromes are the subject of many of these studies, especially after the publication of the first solved crystal structure of an outer membrane cytochrome [17, 19, 37–40].

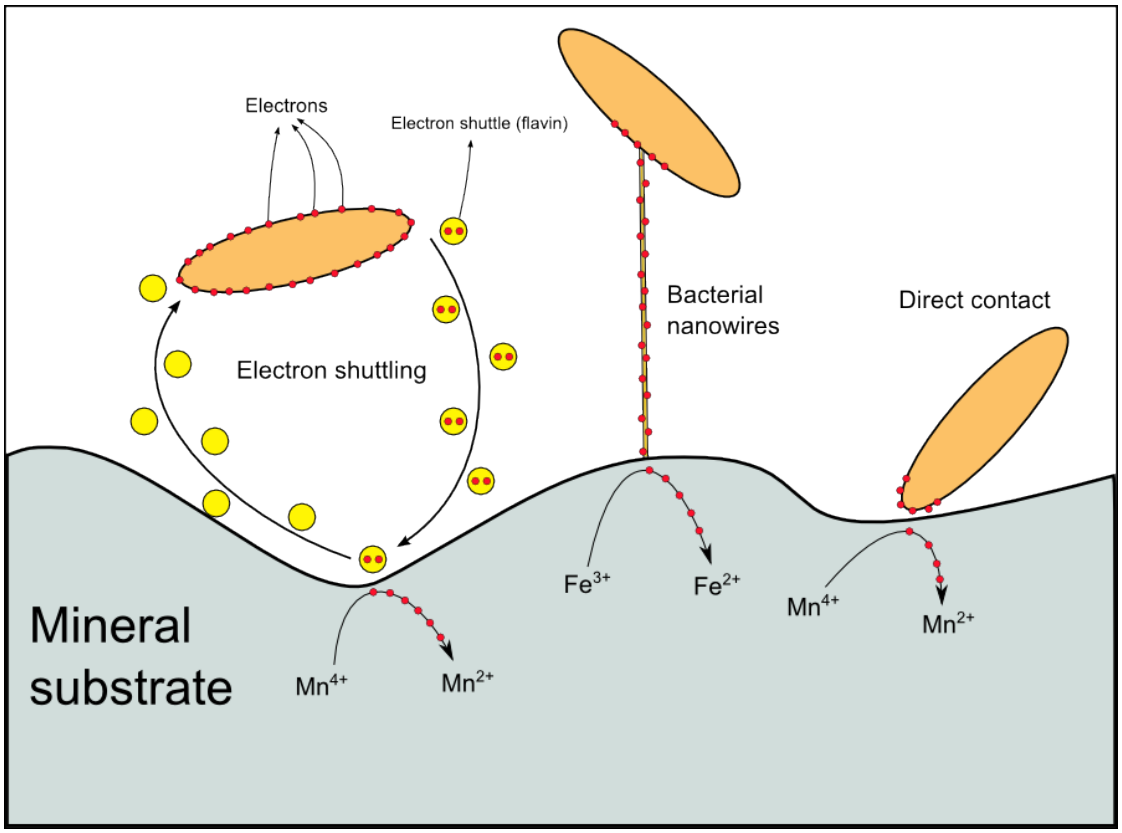

Figure 1.4: Pathways of extracellular electron transfer in *S. oneidensis* MR-1. The direct pathways include electron transfer via cell surface contact and through bacterial nanowires, whereas electron shuttling by flavins represents the indirect pathway.

Localization of cytochromes in the outer membrane of DMRBs facilitates direct electron transfer from the cellular inner membrane to the solid phase minerals directly in contact with the cell exterior. However, DMRBs have also devised strategies to reach insoluble electron acceptors located microns away from their surface. One method, specifically in the case of *Shewanella*, is to use electron shuttles, molecules that are reduced at the cell surface by the outer membrane cytochromes, diffuse in solution to reach the terminal electron acceptor and get oxidized at the metal oxide surface [41–43]. This process is suggested to repeat

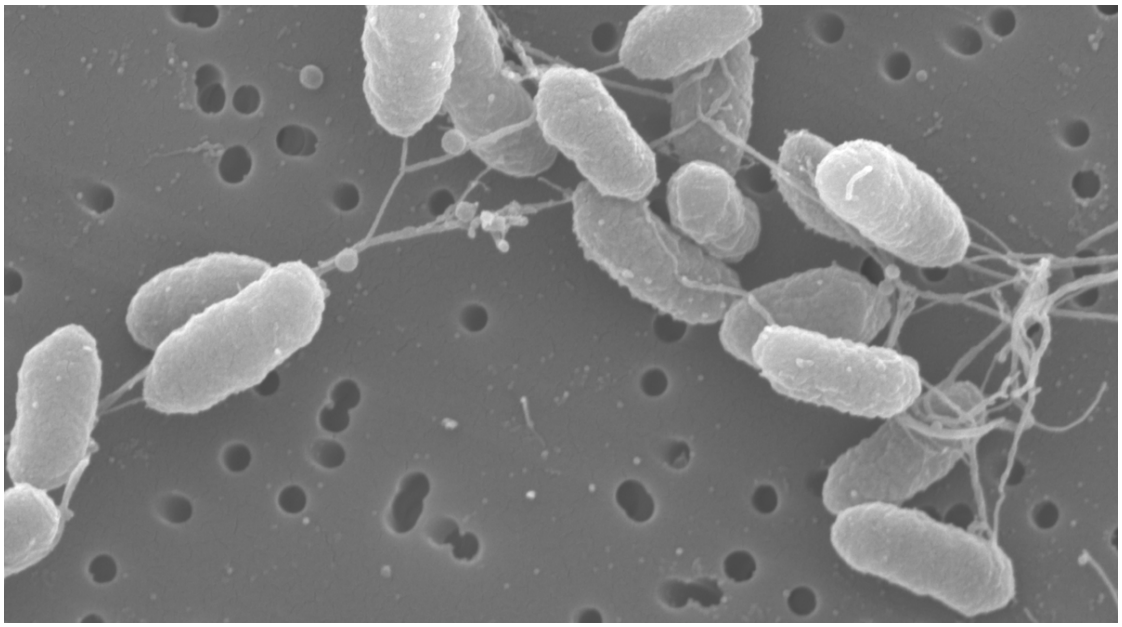

Figure 1.5: Scanning electron microscopy image of bacterial nanowires from *Shewanella oneidensis* MR-1. Image credit: Kar Man Leung, USC.

in cycles, transferring electrons at a fast enough rate to support the respiration rate of cells. However, for this mechanism to be feasible there needs to be a large concentration of shuttle molecules and relatively fast diffusion (*i.e.* large diffusion coefficient) in solution.

Bacterial nanowires represent another EET pathway (Fig. 1.5), in addition to cell surface contact and electron shuttling. The discovery of bacterial nanowires has opened a new chapter in extracellular electron transfer research [30, 31]. These filaments were first observed in *Geobacter sulfurreducens* and *Shewanella oneidensis* MR-1 in 2005 and 2006 respectively. Bacterial nanowires of both organisms were shown to be conductive across their width under non-physiological conditions [30, 31]. In addition, *Shewanella* nanowires (Fig. 1.5) were shown to conduct electrons at a rate of 10^9 e/s at 100 mV applied potential over a length of up to 2 μm

(*Shewanella* cells are about 2 μm in length), which is extremely long compared to typical biological electron transfer length scales, *i.e.* nanometers [32].

It was shown early on that *Geobacter* nanowires are type IV pili [30], *i.e.* protein filaments that are typically used for attachment and twitching motility in bacteria. Deletion of the genes encoding the pilin subunits of these pili produced strains that attached normally to iron oxide surfaces but were not able to reduce these minerals [30]. Therefore it was concluded that the role of *Geobacter* pili in reducing minerals is not in the form of cell attachment as previously believed, but rather pili are transferring electrons to the oxide surface. However, the true identity and composition of *Shewanella* nanowires was not clear from the beginning. The most widely accepted hypothesis was that *Shewanella* nanowires are also type IV pili [44].

The mechanism of electron transport in nanowires of *Geobacter* and *Shewanella* has been a topic of controversy since their discovery [34–36, 44–46]. It has been proposed that *Geobacter* nanowires conduct electrons through 'metallic-like' conductivity that is facilitated by overlapping of π-orbitals of the aromatic amino acids within the pilus structure [47]. On the other hand, *Shewanella* nanowires are proposed to incorporate outer membrane cytochromes along their length that facilitate the flow of respiratory electrons from the cell to the terminal electron acceptor by allowing hopping of electrons between adjacent hemes within each cytochrome and between neighboring cytochromes [32, 34–36]. This multistep hopping hypothesis was supported by the fact that the *Shewanella* mutant lacking genes encoding the outer membrane cytochromes MtrC and OmcA produced non-conductive nanowires [32].

One of the main goals of this dissertation is to present a quantitative evaluation of the two proposed ET mechanisms in bacterial nanowires. In chapter 3, the

experimental electron mobility values in bacterial nanowires are compared with the expected mobility in either of the proposed mechanisms, *i.e.* 'metallic-like' conductivity and multistep hopping. Based on this analysis and considering previous measurements indicating the importance of cytochromes in nanowire conductivity, we find that multistep hopping seems far more likely to be responsible for the observed ET rates in bacterial nanowires of *Shewanella*.

Also in chapter 3, we describe the multistep hopping model which is based on the proposed involvement of outer membrane cytochromes in *Shewanella* nanowire conductivity. In this model a chain of redox sites, *e.g.* hemes, is suggested to facilitate long-range electron transport by hopping between adjacent redox centers. We have combined the Marcus theory of ET to predict the rates of the non-adiabatic ET between the redox sites and the electrochemical form of Marcus theory to model the interfacial ET rates between the redox sites and the experimental electrodes addressing the nanowires. A master equation that includes all these rates is then presented and solved to give the predicted current-voltage behavior of the nanowire system. In the end, we find the predicted current-voltage curves in good agreement with previous experimental data.

Other than the mechanism of electron transport, fundamental questions about bacterial nanowires still remain unanswered. Specifically, the composition and structure of *Shewanella* nanowires is unknown. These filaments are generally assumed to be type IV pili [44], perhaps due to their similar proposed function as *Geobacter* pili, *i.e.* transporting electrons. However, it is important to note that the composition of *Shewanella* nanowires had never been directly studied. Researchers have attempted to evaluate the impact of deletion of type IV pili genes in electricity production of *Shewanella* cultures in microbial fuel cells and similar large scale systems [20]. These experiments however fail to isolate the

impact of type IV pili in cell attachment and biofilm formation from their role in electron transfer between cells and electrodes as possible structural components of bacterial nanowires.

There are also other important questions regarding bacterial nanowires: What is the physiological impact of nanowire production on cells? In particular, how does producing nanowires enhance a cells ability to survive under electron acceptor-limited conditions? What is its effect on cellular respiration?

One common weakness in all previous measurements on nanowire conductivity is that they were performed under non-physiological conditions, *i.e.* samples are typically fixed with aldehydes and dried while on a surface [30–32, 47]. Both the fixation and the dehydration steps could potentially alter the nanowire structure, the alignment and configuration of the OM cytochromes, and therefore change the conductive properties of the nanowire under study compared to its native, hydrated state. This lack of *in vivo* work has been due to the challenges that arise monitoring and sustaining growth of nanowires in solution. However, in this thesis, we find that *in vivo* imaging of bacterial nanowires is in fact the common basis in answering all of the questions posed above.

In this thesis, we introduce a new experimental approach to investigate *Shewanella* nanowires. In chapter 4 of this thesis, we report, for the first time, the development of a technique for imaging bacterial nanowires *in vivo*. We used fluorescence microscopy to image *Shewanella* cells that were maintained inside a microliter-volume perfusion chamber. Monitoring growth of bacterial nanowires using this method presented a significant challenge because all previous studies on *Shewanella* nanowires used bioreactors with controlled concentration of oxygen to produce the samples [31, 32]. However, in the new technique, nanowire producing conditions were obtained inside the perfusion chamber that enabled us to watch

the live growth of these filaments. The specifics of the developed experimental platform and methods used are explained in chapter 4.

The *in vivo* imaging platform also allowed us to examine the physiological impact of nanowire production on cells using a fluorescent indicator of cellular reductase activity [48, 49]. As nanowires were produced, the fluorescence intensity of this respiratory indicator increased, showing elevated respiration rates correlating with nanowire production.

To address the composition of *Shewanella* nanowires, protein-specific and lipid-specific fluorescent stains were used to label proteins and lipids on bacterial nanowires in solution. To our surprise, the lipid stain completely stained all bacterial nanowires, indicating the presence of lipid in these filaments. To further elucidate the structure, we localized fluorescent proteins inside the cellular periplasm which also localized inside *Shewanella* nanowires. This observation demonstrated that *Shewanella* nanowires are in fact extensions of the cellular outer membrane.

In vivo imaging of nanowires can also be used to investigate the possible mechanism of electron transport in nanowires. As proposed in the multistep hopping model and also based on previous conductivity measurements, the presence of outer membrane cytochromes facilitates the long range electron transport along a nanowire [32, 34]. In this thesis, using the *in vivo* imaging platform in combination with immunofluorescence microscopy we demonstrate the presence of MtrC and OmcA, the main OM cytochromes of *Shewanella*, along the filaments. In chapter 5, we describe how nanowires imaged *in vivo* during their growth can later be stained with antibodies raised against the specific OM cytochromes, allowing the visualization of these proteins along the same nanowires.

Given the presence of OM cytochromes along bacterial nanowires, it is beneficial to examine the electron transfer properties of individual OM cytochromes.

This information can serve as the stepping stone for building a large scale physical model that accurately describes the long-range electron transport characteristics of the entire nanowire system. MtrF, the cytochrome studied in this thesis, was chosen because it is the first outer membrane cytochrome with a published crystal structure [17]. In chapter 5, we report the development of an approach for investigation of the electron transfer properties of MtrF at the single-molecule level that is based on scanning tunneling microscopy (STM). Recombinant MtrF molecules are adsorbed on an atomically flat gold (Au(111)) substrate to form a uniform monolayer. Individual proteins are then approached by an STM tip, while a potential is applied between the tip and the gold substrate. The transferred current through MtrF can be measured as a function of the applied tip-substrate potential and compared with the results from recent simulations of MtrF conductance [40].

Moreover, additional details about the alignment and configuration of OM cytochromes on nanowires can be obtained by high resolution imaging using atomic force microscopy (AFM) and transmission electron microscopy (TEM). These observations can guide the assumptions regarding the configuration and spacing of the redox sites (hemes) and cytochromes, important factors in the multistep hopping model. In addition, the exact morphology and dimension of bacterial nanowires is more accurately measured in AFM and TEM imaging. In chapter 5 of this thesis, we describe AFM and TEM imaging of bacterial nanowires produced in the perfusion imaging platform. The preliminary TEM images reveal the membranous nature of nanowires while, along with the AFM images, indicating their various morphologies ranging from vesicle chains to smooth filaments.

In the context of MFCs, the biotic-abiotic interaction between the bacteria and the electrode in the MFC is extremely important in the efficiency and quality of

renewable energy conversion [50]. Bacterial nanowires constitute one of the mechanisms proposed for electron transfer between bacteria and extracellular solid phase electron acceptors such as electrodes in a MFC [50]. Using bacterial nanowires, not only the bacteria adjacent to the electrode can contact the surface to transfer electrons, but other cells remote from the surface can transfer electrons to the cells that are in contact with the electrode. Thus in a biofilm, which is normally formed on such electrodes in MFCs, bacteria can breathe through one another using bacterial nanowires and ultimately transfer the electrons extracted by the large community of cells in the biofilm to the electrode [50, 51]. Therefore understanding mechanisms of extracellular electron transfer in bacteria and the properties of bacterial nanowires can help us improve electron transfer at the interface of bacteria and electrodes and is crucial in developing more efficient microbial fuel cells as sources of cheap renewable energy.

In addition to the impact in microbial fuel cell research, bacterial nanowires might play an important role in biofilm formation and maintenance. First, they may establish contact between cells by connecting cells together to possibly build the structural backbone of the biofilm. Second, due to their conductive properties, bacterial nanowires might have the ability to facilitate respiration of bacteria in a biofilm by transferring electrons between cells which leads to sustained cellular respiration and energy conservation [52]. Examples of such biofilms occur in oral pathology, in disorders such as osteonecrosis of the jaw, where biofilms are difficult to treat and are resistant to antibiotics [52, 53]. In this case, the ability to destabilize the structural and metabolic integrity of the biofilm can be essential in treating the disorder. Notably, bacterial nanowires have been shown to exist and play a role in the stability of these biofilms [52, 53]. Therefore a better understanding of

bacterial nanowires and their properties can lead to development of treatments for biofilm-related disorders such as osteonecrosis of the jaw.

This thesis includes 6 chapters. Chapter 2 introduces the bioenergetic context, the mechanisms of extracellular electron transfer, the non-adiabatic electron transfer theory, and describes the specific fluorescence microscopy schemes used in this thesis. In this chapter, we also review some aspects of the solved crystal structure of the outer membrane cytochrome MtrF.

Chapter 3 features a quantitative evaluation of the proposed mechanisms of electron transport in bacterial nanowires based on the experimental evidence. Then we introduce the multistep hopping model of electron transport and compare its results with the conductivity measurements on bacterial nanowires. This chapter also motivates the *in vivo* cytochrome-localization experiments described in chapter 5.

Chapter 4 introduces the *in vivo* imaging of bacterial nanowires. We demonstrate that the production of nanowires correlates with increased cellular reductase activity. We also show, using fluorescent dyes and proteins, that *Shewanella* nanowires are outer membrane extensions. We describe our gene expression analysis of *Shewanella* nanowire samples in chemostats where we analyze the changes in expression of various genes including type IV pili genes as cells produce nanowires. This analysis serves as additional evidence supporting our findings on bacterial nanowire composition.

Chapter 5 addresses the localization of outer membrane cytochromes MtrC and OmcA on *Shewanella* nanowires as well as the electron transfer properties of the outer membrane cytochrome MtrF. Antibodies raised against OmcA and MtrC in combination with fluorescent secondary antibodies are used to demonstrate the presence of these proteins along nanowires. Samples described in this chapter are

prepared in the *in vivo* imaging platform described in chapter 4, where the target nanowires imaged during their growth are later checked for OM cytochrome presence. The findings reported in this chapter point to the OM cytochromes as possible facilitators of ET along nanowires, as was assumed in the multistep hopping model in chapter 3. Based on data from the gene expression analysis on chemostat samples introduced in chapter 4, we also report an increase in expression of OM cytochrome genes upon production of nanowires. These genes include *omcA*, *mtrC* and *mtrA*. In addition we describe the development of an approach for investigating the electron transfer characteristics of individual molecules of the outer membrane cytochrome MtrF. Purified MtrF is used to assemble a uniform monolayer of the cytochrome on atomically flat gold substrate. Single MtrF molecules can then be addressed with an STM tip in order to measure their conductivity, resulting in current-voltage curves. In addition, using live fluorescence microscopy in combination with TEM and AFM imaging, we demonstrate the different stages of nanowire growth and the occasional transformation of nanowires from vesicle chains to smoother filaments during early growth. The results reported here further clarify the morphologies of bacterial nanowires and indicate the membranous nature of these filaments. This chapter also points to TEM as a promising technique to investigate the configuration, alignment and spacing of outer membrane cytochromes along bacterial nanowires.

Finally, chapter 6 concludes this thesis. We review the work presented in this thesis and look at possible future work that can be built on the studies reported here to further advance our knowledge of extracellular electron transfer.

Chapter 2

Background

2.1 Energetics of life and oxidative phosphorylation

Living organisms are highly ordered systems in contrast to their environments. In order for life to maintain this imbalance of order, free energy has to be continuously transferred from the environment to the system [54]. A limited number of strategies are used by various forms of life to accomplish this vital task including respiration, fermentation and photosynthesis. An essential process in these strategies is electron transfer (ET) within or between biomolecules in biomembranes. The ET reactions lead to the formation of an electrochemical gradient across the cell or mitochondrial membrane that provides energy for formation of phosphate bonds in adenosine triphosphate (ATP). The dissociation of this bond, which leads to the conversion of ATP to adenosine diphosphate (ADP) is a universal source of free energy in biology [55].

In respiration, electrons derived from a high energy source, an electron donor (ED), flow through the electron transport chain (ETC) and are discarded to the environment, i.e. a low energy electron acceptor (EA) [3]. The energy disparity between high and low energy electrons is harnessed by the cell in the form of produced ATP molecules. A variety of electron donors and acceptors are used in

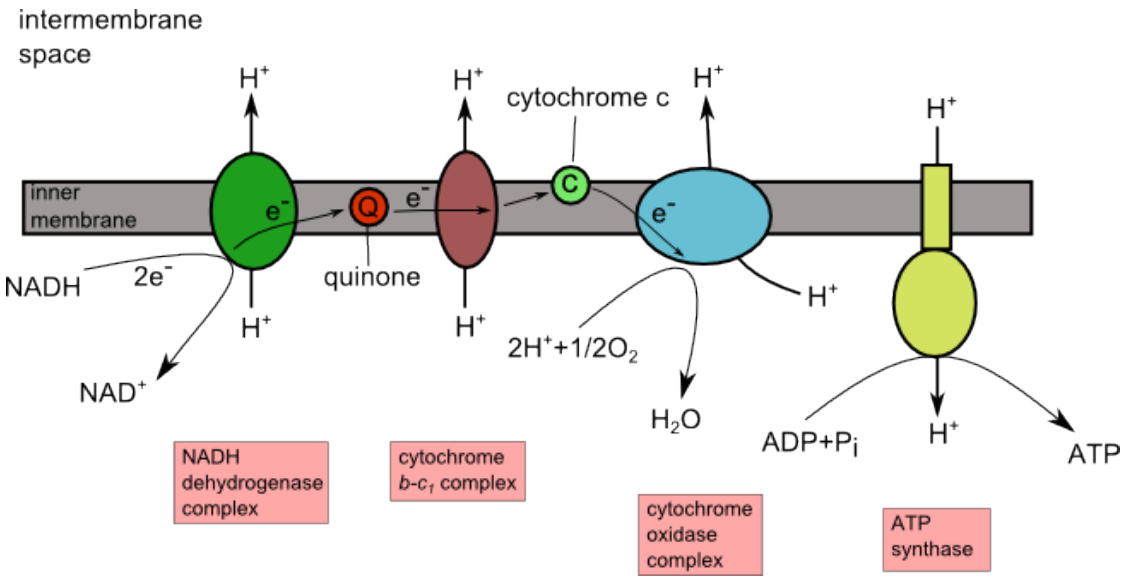

Figure 2.1: Schematic of the electron transport chain (ETC) in respiratory organisms. Electron transfer through the components of the ETC drives the pumping of protons across the inner (mitochondrial) membrane. The resulting proton motive force then powers the production of ATP, the universal currency of free energy in biology.

respiratory metabolisms, depending on their energy levels and availability. Examples of common electron donors and acceptors are carbohydrates and molecular oxygen (for aerobic organisms), respectively.

Electron transport through the electron transfer chain involves a number of carrier sites and proton pumps that are placed inside the inner membrane of the cell (or the mitochondrial inner membrane) as well as the ATP producing enzyme ATP synthase (Fig. 2.1) [56]. As electrons enter and move along the chain between the carrier sites, protons are pumped from the inside of the cell to the outside, building up a proton concentration gradient across the inner membrane [3]. Subsequently the ATP synthase acts as a channel through which these protons can move back to the cell interior. The energy from the proton gradient dissipation is harnessed by ATP synthase to high energy phosphate bonds in ATP molecules

through transforming ADP to ATP. Each ATP molecule stores about 500 meV of energy which can be released through ATP hydrolysis [56]. The synthesized ATPs are later used in various functions as source of energy, *e.g.* to synthesize proteins, RNA and DNA or in active transportation of molecules within the cell in eukaryotic cells.

Electron transfer from ED to EA is the driving force for cellular respiration and is continuously required for steady production of ATP [3]. The redox potential of the EA relative to the ED determines how favored the EA is to be used by the organism. A more negative potential for ED and a more positive redox potential for EA are favorable for the cell (Fig. 2.2) [57].

2.2 Anaerobic respiration and dissimilatory metal reduction

Oxygen is the most energetically favored electron acceptor (Fig. 2.2 2), and it is widely used by various species. When oxygen is used as electron acceptor, the respiration is called aerobic as opposed to anaerobic respiration in the case of other electron acceptors. Metals ions are one group of electron acceptors that are more available than oxygen in some environments on earth, for instance meters beneath the ground where oxygen is scarce [22]. Some of the organisms evolved under oxygen-limited conditions use metal ions to dispose of their respiratory electrons. The group of prokaryotes that couple metal reduction to cellular respiration is called dissimilatory metal reducing bacteria or DMRBs. As opposed to oxygen and other soluble electron acceptors, solid metal oxides can be used by DMRBs as EA outside the cell [22]. To accomplish this there is an entire apparatus in

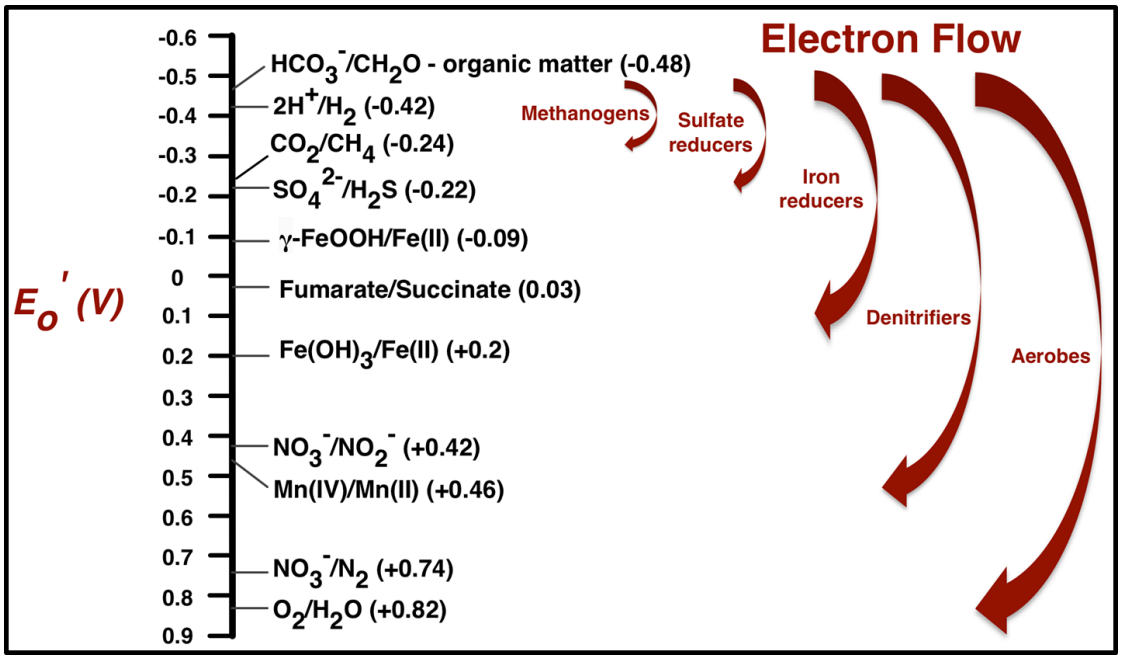

Figure 2.2: Redox tower containing a list of electron donors and acceptors and the redox potentials associated with their redox reactions. For electron donors a more negative potential (top of the tower) and for electron acceptors a more positive potential (bottom of the tower) is favorable for use by cells. Oxygen has one of the most positive redox potentials in the list; therefore it is commonly used as the EA by various organisms. Organisms are categorized (red arrows) according to the electron donor/acceptor combination they consume. Aerobes, for instance, use organic matter as electron donor and oxygen as the electron acceptor in respiration.

DMRBs to transfer electrons to the cell exterior and extracellularly reduce the EA [14].

Shewanella oneidensis MR-1, a facultative anaerobe, is one of the well-studied DMRBs that was isolated [8] from Lake Oneida in New York. This strain was initially reported to couple its anaerobic growth to reduction of manganese oxide, but was later confirmed to be much more versatile in terms of electron acceptor reduction and hence serves as a great model organism for investigating extracellular respiration [6, 8]. The connection between metabolic respiration and extracellular oxide reduction has been shown using electron transport inhibitors [9]. These

chemicals disrupt the function of carrier sites in the electron transport chain and thus stop the flow of respiratory electrons. When *S. oneidensis* MR-1 was exposed to these inhibitors, the oxide reduction stopped; indicating the coupling between electron transport and reduction of oxides [9].

2.3 Outer membrane cytochromes

All the proposed mechanisms for extracellular electron transfer (EET) in *S. oneidensis* MR-1 involve outer-membrane (OM) cytochromes [58]. Cytochromes, in general, are proteins that incorporate specific iron-containing prosthetic groups referred to as hemes. Presence of iron atoms in the cytochrome structure enables it to catalyze redox reactions by carrying the electrons involved in the reaction [19]. In the case of extracellular respiration, outer-membrane cytochromes are shown to be present on the outer surface of the outer-membrane of the cell [11, 13], enabling the transfer of electrons from the cell to the terminal electron acceptor. In addition to that, other cytochromes have been found to be responsible for carrying the electrons from the inner membrane (the electron transport chain) to the periplasm, through a porin in the outer membrane, and to the exterior of the cell [14, 59] (Fig. 2.3). As part of this chain, 'porin-cytochrome' modules are found to transport electrons across the outer membrane [18, 59] (Fig. 2.4). Overall, this array of cytochromes help conduct electrons necessary for ATP production to the outer leaflet of the outer-membrane (Fig. 2.3).

2.4 MtrF and its crystal structure

Recently the crystal structure of MtrF, one of 42 putative OM cytochromes in *Shewanella* has been published [17], raising the possibility of more careful and detailed

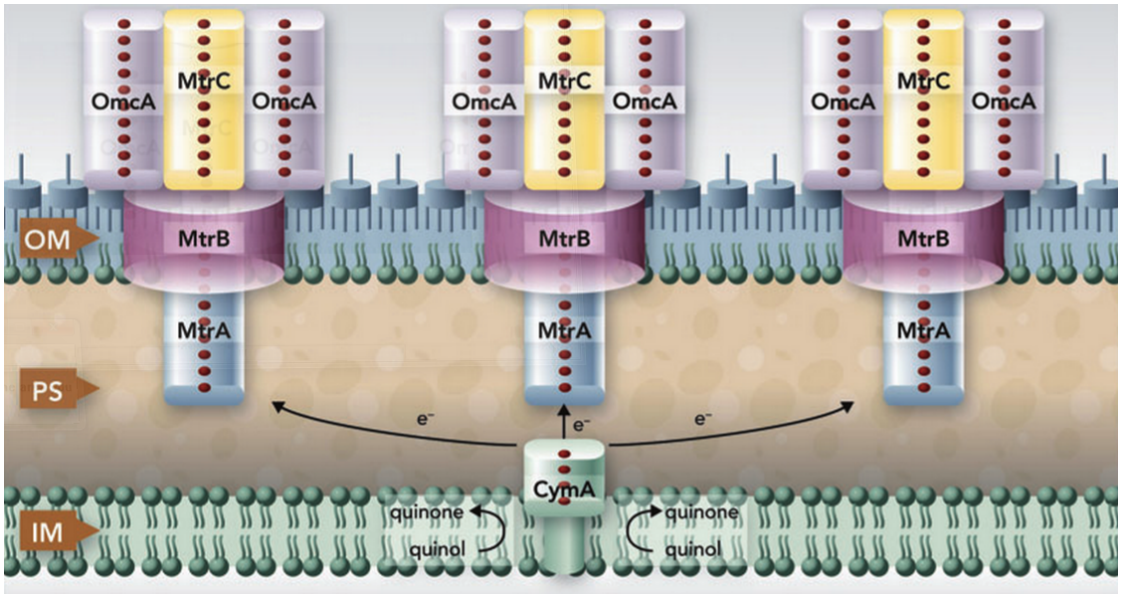

Figure 2.3: The extracellular electron transport pathway in *Shewanella*. Respiratory electrons are transferred to the cytochrome CymA at the inner membrane and subsequently to the porin-cytochrome module at the outer membrane. Reprinted with permission from [14], copyright John Wiley & Sons Inc.

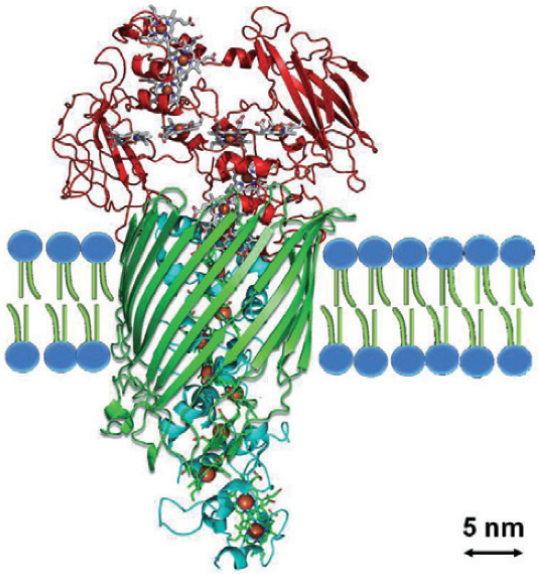

Figure 2.4: The porin-cytochrome module consists of a decaheme cytochrome embedded from the periplasmic side into a porin in the outer membrane, the porin, and an outer membrane cytochrome. From [59].

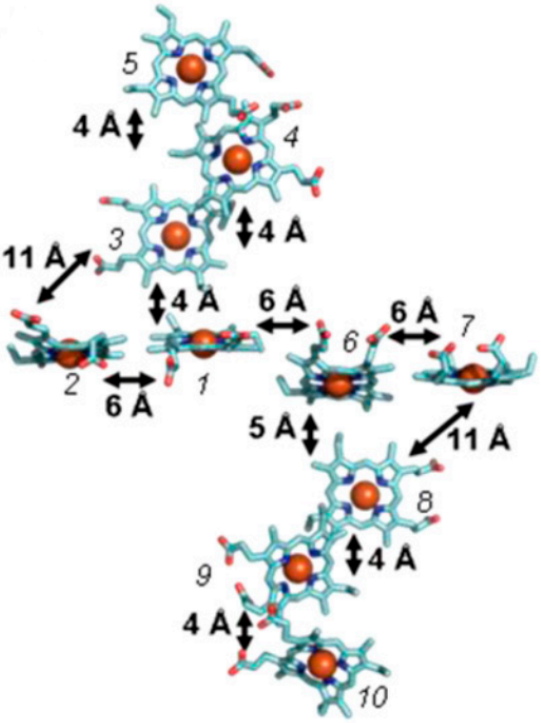

Figure 2.5: Position of heme groups in the staggered cross-like structure of the decaheme outer membrane cytochrome MtrF. The spacing between adjacent hemes is less than 1 nm. From [17], Copyright National Academy of Sciences USA.

calculations regarding electron transport in MtrF, its homologs and larger extracellular structures incorporating OM cytochromes. The molecule has an oblate ellipsoid shape with dimensions of $85 \times 70 \times 30$ Å. This 3.2-Å resolution crystal structure shows the relative position of all the 10 hemes within a decaheme OM cytochrome for the first time [17] (Fig. 2.5). The heme localization pattern in MtrF resembles a staggered cross with a 65-Å octaheme chain along the length that is crossed by a 45-Å tetraheme chain in the middle (Fig. 2.5).

Interestingly, the spacings between all adjacent hemes in MtrF are smaller than 1 nm (Fig. 2.5), suggesting the possibility of ET through the entire molecule by multistep electron hopping between neighboring hemes [34–36]. Heme 10 is proposed to be the input site of electrons from the cell, while heme 5, evidenced

by its high exposure to the solvent, would act as the exit point of electrons onto the insoluble mineral [17]. This would mean that electrons move along the longer chain (from heme 10 to heme 5) to reach the mineral.

In addition to the electron transfer path to the insoluble electron acceptor, there are two beta-barrel domains containing extended Greek key split-barrel structures which are common in flavin binding domains [17]. In addition, researchers have shown that OM cytochromes of *Shewanella* reduce flavins, molecules proposed to act as electron shuttles in EET [60]. Although it has not been directly demonstrated, these findings point at the possibility that flavins are reduced by binding to MtrF at these beta-barrel domains. The bound flavins would then exchange electrons with hemes 2 and 7, the closest hemes to the flavin-binding sites [17]. Therefore, the electron transport from heme 10 to either heme 2 or 7 would be another scenario of multistep ET that results in reduction of shuttles. This alternative pathway is especially beneficial if the heme 10-to-heme 5 ET pathway is blocked, possibly due to lack of direct contact between the cytochrome (at heme 5) and the insoluble mineral.

To investigate the conductive properties of individual MtrF molecules, the protein must be placed between two conductors that act as electrodes. For this reason, in the conductivity experiments described in this thesis, we use recombinant MtrF that has a surface exposed tetra-cysteine tag at its C-terminus (Fig. 2.6), enabling the cytochrome to covalently bind to Au(III) [40, 61]. Upon binding of MtrF to gold, the gold substrate can be used as an electrode that is in contact with the target molecule. The gold-adsorbed MtrF is then approached by the atomically sharp and conductive tip of the Scanning Tunneling Microscope (STM) from above to perform the desired conductivity measurements (Fig. 2.7) [40, 61]. This is

done by applying a bias voltage between the gold substrate (bottom) and the conductive tip (top) and measuring the current passing through the molecule, between the two electrodes.

2.5 Atomic force and scanning tunneling microscopy

Atomic force microscopy (AFM) [62] and scanning tunneling microscopy (STM) [63] both belong to the family of probe-based microscopy techniques and are used for nanoscale characterization of samples that are typically deposited on a surface. In both techniques, a sharp tip approaches the sample from above while the sample-tip spacing is measured through movements of the tip (in AFM) or the magnitude of the tunneling current between the tip and the substrate (in STM). Using a piezoelectric stage that accurately controls the height of the substrate, a feedback loop maintains the tip-sample distance constant while the tip laterally sweeps the sample. The obtained map of the stage height as a function of the lateral tip position gives the topography of the sample. Unlike AFM, STM can also be used to examine electron transfer properties of the sample by measuring the tunneling current as a function of the applied tip-substrate potential.

2.6 Pathways of extracellular electron transport (EET)

Extracellular electron transfer pathways can be categorized into two broad groups: direct and indirect mechanisms [58]. Indirect mechanisms involve small molecules such as flavins that either, as hypothesized, diffusively shuttle respiratory electrons

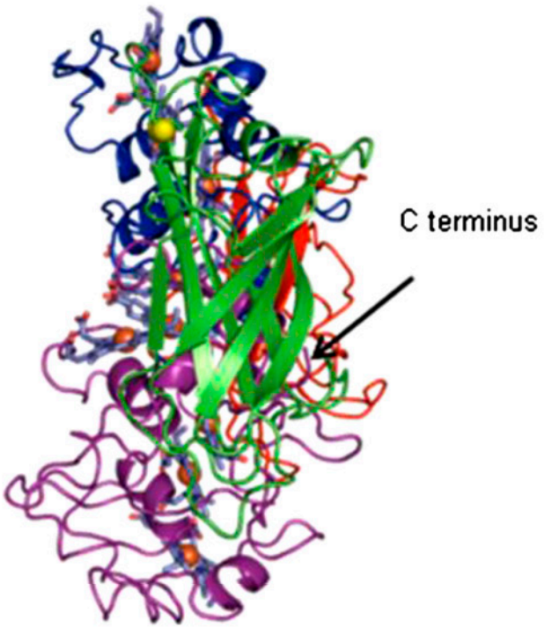

Figure 2.6: Crystal structure of the decaheme outer membrane cytochrome MtrF along with the position of the protein C-terminus. A tetra-cysteine tag added at the C-terminus allows covalent binding of the protein to a gold substrate. From [17], Copyright National Academy of Sciences USA.

from the cell surface to the solid-phase electron acceptor [41, 42] or chelate metal ions inside the cell to interact with the cellular oxidoreductases.

In direct mechanisms, electrons are transferred via a number of multiheme cytochromes directly to the mineral surface. This includes ET through direct contact between cell and solid surface or through micrometer-long conductive filaments known as bacterial nanowires [30, 31]. Another case of direct extracellular electron transfer occurs in interspecies electron transfer through natural conductive minerals [64], where a cell from one species capable of oxidizing a specific electron donor transfers its respiratory electrons through conductive minerals to another cell of a different species that reduces a specific electron acceptor.

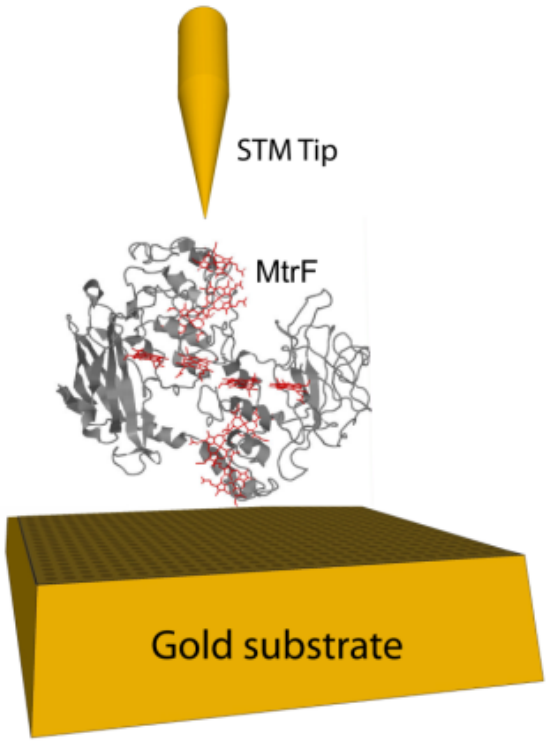

Figure 2.7: Schematic showing an MtrF molecule adsorbed on an atomically flat gold substrate with a scanning tunneling microscope (STM) tip approaching it from above. The STM tip and the gold substrate act as two electrodes in the MtrF conductance measurements.

2.7 Bacterial nanowires and their conductive properties

Bacterial nanowires produced by *S. oneidensis* MR-1 were first discovered in 2006 [31]. Cell cultures were grown continuously in a chemostat with excess oxygen as electron acceptor, under ED-limitation conditions. At some point, the oxygen input rate into the system is reduced so much that the conditions are changed from ED-limitation to EA-limitation in the reactor. Samples were taken from the oxygen-limited culture, were imaged with a scanning electron microscope (SEM) and were confirmed to contain microbial appendages. Further analysis of these

samples using scanning tunneling microscopy showed that these appendages are conductive and therefore can be referred to as nanowires. Also, as another indication of conductivity of these nanowires, they were shown to be essential in biological reduction of solid metallic electron acceptors by *S. oneidensis* MR-1. But further experiments were yet to be done to determine the exact transport mechanism and the conductive properties of bacterial nanowires.

The first quantitative measurement on the conductivity of bacterial nanowires was performed in 2008 [65]. Using conductive atomic force microscopy a voltage was applied across the width of a single nanowire and the resulting current was measured. The I-V curve from that experiment showed nA currents being carried by the nanowire across its width (Fig. 2.8A). Two years later another experiment demonstrated that bacterial nanowires are in fact able to transfer electrons longitudinally (μm length scales) [32]. Chemostat samples containing nanowires were deposited on a silicon oxide surface with pre-fabricated gold lines. Using SEM, each nanowire candidate was found on the non-conductive silicon oxide between two gold lines. Then by using platinum deposition, two micron-scale electrodes were deposited to connect each end of the nanowire to one of the gold lines. Later a voltage was applied between the two gold lines connected to the nanowire and the current was measured, producing the I-V curve in Fig. 2.8B.

One important feature of both of these results is the magnitude of the current at around 1 V. This number is orders of magnitude larger than the cellular respiration electron transfer rate of 10^6 electrons per second [32, 66], indicating that a single nanowire is capable of supporting an individual cell in terms of extracellular respiration. This is consistent with the proposed role of bacterial nanowires, namely to transfer a cell's respiratory electrons to the terminal electron acceptor.

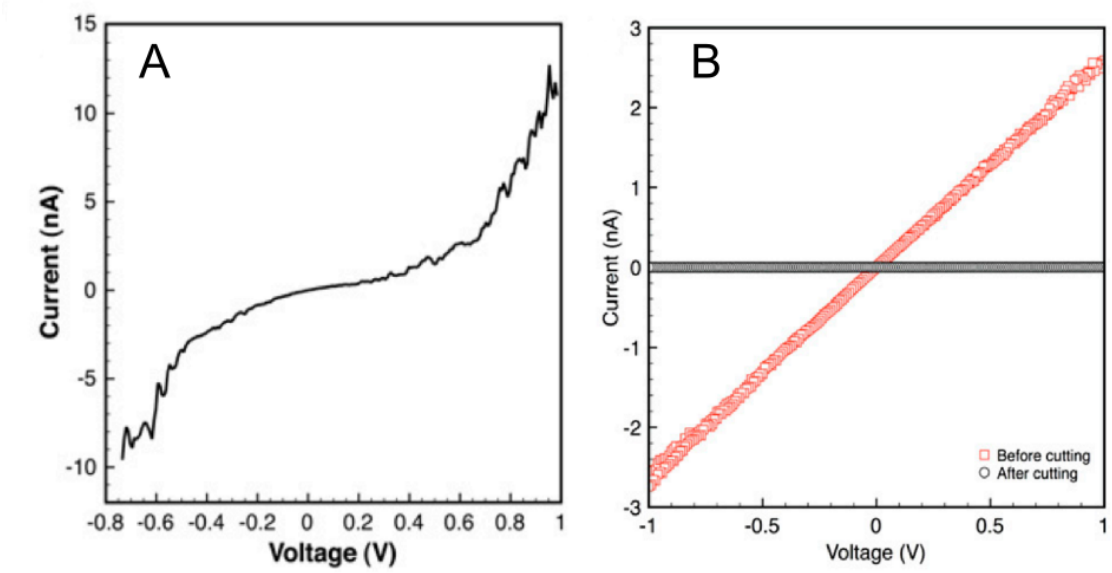

Figure 2.8: I-V curves from conductance measurements on bacterial nanowires of *Shewanella*. A) Transverse measurement across the 10-nm width of a nanowire. B) Longitudinal measurement along the 2000-nm length of a nanowire. The transverse and longitudinal curves appear to be different, raising questions about the physical electron transport mechanism behind nanowire conductance. A reprinted from [65], with permission from Elsevier. B reprinted from [32], Copyright National Academy of Sciences USA.

By looking at the I-V curves from the longitudinal and transverse conductance measurements, one may ask why the two curves appear to be so different. It is worth noting that despite the importance of theoretical modeling of these conductance data in answering such questions and revealing the mechanism of electron transport in bacterial nanowires, these measurements were not modeled in any way prior to the work reported in this thesis.

2.8 The theory of non-adiabatic electron transfer

An initial step to investigate transport in both individual cytochromes and bacterial nanowires is to specify the electron transfer (ET) rate between two neighboring

redox sites, which are in this case two hemes. The powerful theory of non-adiabatic ET which originated from the theoretical findings of Rudolph Marcus in 1956 [28] describes the electron transfer rate in ET reactions in terms of two factors [2]. The first factor which was the focus of Marcus' earlier work concerns the effect of nuclear configurations of the donor-solvent-acceptor system on the ET rate that are collectively reflected in a single nuclear reorganization parameter (λ, or the reorganization energy). Marcus introduced an exponential term involving λ to describe the effect of the nuclear configurations on the overall ET rate:

$$k_{et} \propto \exp\left[-\frac{(\Delta G+\lambda)^2}{4\lambda k_B T}\right] \tag{2.1}$$

where ΔG is the free energy change as a result of the ET, λ is the reorganization energy, k_B is the Boltzmann constant and T is the temperature. A counter-intuitive prediction resulting from Marcus' exponential expression was the Marcus inverted region, where increasing the driving force of the reaction reduces the overall reaction rate. This prediction was later verified by experiments [67, 68].

Later in 1974, Hopfield introduced the effect of the electronic coupling between the donor and the acceptor in the form of electron tunneling through a square barrier [29]. This effect was included in the overall ET rate as a pre-exponential term behind the Marcus exponential expression which is equal to the electron tunneling rate when the nuclei are in the transition state from reactant to product in the ET reaction. Combining the electron coupling and the nuclear configuration effects gives the non-adiabatic ET rate as [2]:

$$k_{et} = \frac{2\pi}{\hbar}\frac{|H_{DA}|^2}{\sqrt{4\pi\lambda k_B T}}\exp\left[-\frac{(\Delta G+\lambda)^2}{4\lambda k_B T}\right] \tag{2.2}$$

where λ is the reorganization energy of the system, k_B is the Boltzmann constant, T is the temperature, ΔG is the free energy change as a result of the electron transfer, and $|H_{DA}|$ is the coupling matrix element which contains the exponential tunneling factor. In the context of cytochrome ET, λ is the reorganization energy of the cytochrome and ΔG is the electric potential difference between the donor and the acceptor as a result of the applied voltage to the system.

In experiments regarding the conductive properties of OM cytochromes and nanowires, the potential is applied using two electrodes which make contact with the system. Therefore, other than the protein-protein ET kinetics, the interaction between the electrode and the cytochrome has to be taken into account [69]. For this reason, we also consider the density of states in the metallic electrode which is a function of the potential applied to the electrode. So similar to the protein-protein case, the protein-electrode ET rate is given by [69]:

$$k_{et} = C_{electrode} \int_{-\infty}^{\infty} \frac{\exp\left[-\left(x - \frac{\lambda + e(E-E^0)}{k_B T} \right)^2 \left(\frac{k_B T}{4\lambda} \right) \right]}{1 + \exp(x)} dx \tag{2.3}$$

where $C_{electrode} = \frac{2\pi}{\hbar} \sqrt{\frac{k_B T}{4\pi\lambda}}\, \overline{|H|^2 \rho}$, E^0 is the potential of the protein, E is the potential of the electrode, λ is the reorganization energy of the protein, $|H|$ is the coupling matrix element, and ρ is the density of states in the electrode [69]. Therefore this modified version of the non-adiabatic ET theory describes the protein-electrode ET kinetics. In the end, a complete model attempting to describe the experimental data on OM cytochrome/nanowire conductivity must address both the protein-protein and protein-electrode interaction properties using the above ET rate equations.

2.9 Fluorescence Microscopy

Here we describe the various fluorophores used in combination with fluorescence microscopy in this dissertation to characterize the composition, structure and components of bacterial nanowires and outer membrane vesicles.

To visualize proteins in bacterial extracellular structures, we use the fluorescent dye NanoOrange. This dye is nonfluorescent in aqueous solution, and undergoes a significant increase in fluorescence upon binding to hydrophobic regions of proteins [70]. NanoOrange was previously used to visualize nanometers-thick filamentous protein structures such as bacterial flagella [71]. In this work we use NanoOrange for staining the bacterial structures of interest, *i.e.* bacterial nanowires and outer membrane vesicles, due to its effectiveness in staining similar bacterial structures.

To test the extent of membrane involvement in nanowire formation, we labeled *S. oneidensis* MR-1 cells with the membrane stain FM 4-64FX. This styryl dye is membrane-selective as a result of a lipophilic tail that inserts into the lipid bilayer and a positively charged head that is anchored at the membrane surface [72, 73]. The amphiphilic nature of this molecule hinders it from freely crossing the membrane into the cellular interior except through the endocytic pathway, as extensively characterized in eukaryotic cells [73, 74]. FM 4-64 has also been widely used in bacterial cells and shown to specifically label membranes but not extracellular protein filaments such as flagella [75, 76], except in a few bacterial species where flagella are coated in membrane sheaths [77].

In addition, we used a fluorescent redox-sensing dye, RedoxSensor Green (RSG), to demonstrate the impact of nanowire production on live cells of *S. oneidensis* MR-1. RSG is an indicator of bacterial reductase activity and it serves as a reporter for changes in electron transport chain function [49]. This dye permeates through both cellular membranes and interacts with components of the

cellular electron transport chain, producing a stable green fluorescence emission upon reduction. Furthermore, bacterial cells undergo a significant decrease in RSG fluorescence upon addition of inhibitors of different electron transport chain components [49]. RSG was previously used as a reporter of bacterial metabolic activity in environmental samples [48] and as an indicator of the respiratory activity of *Geobacter sulfurreducens* cells [78]. In this work, we demonstrate, for the first time, the capacity of RSG as a marker for respiratory activity in *Shewanella* (chapter 4) and subsequently use RSG to show the increase in cellular respiration rate upon production of bacterial nanowires.

In this work, we use indirect immunofluorescence, a popular technique for visualizing specific biomolecules, to observe localization of the OM cytochromes MtrC and OmcA along bacterial nanowires [79]. In this technique, the structures are stained with rabbit-raised polyclonal primary antibodies that are specific to MtrC and OmcA (the antigens) and bind to the corresponding epitopes on these proteins via their fragment antigen-binding (Fab) domains [79] (Fig. 2.9). A goat anti-rabbit secondary antibody is subsequently added that binds the cytochrome-bound primary antibodies at their fragment crystallizable region (Fc) [79] (Fig. 2.9). Since the Fc domain is constant between antibodies from the same species (in this case rabbit), a single anti-rabbit secondary antibody is used to bind the Fc domains of both MtrC and OmcA-specific rabbit-raised primary antibodies. The secondary antibody used also carries multiple conjugated FITC (Fluorescein isothiocyanate) fluorophores (Fig. 2.9), in turn allowing visualization of MtrC and OmcA along bacterial nanowires.

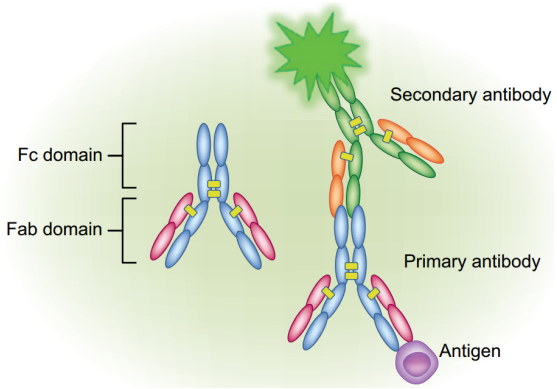

Figure 2.9: Schematic of the indirect immunofluorescence technique. After binding of the primary antibody to the antigen, the Fab region of the secondary antibody binds to the Fc region of the primary antibody. The fluorophore conjugated to the secondary antibody enables visualization of the antigen through fluorescence microscopy. Reprinted by permission from Macmillan Publishers Ltd: Journal of Investigative Dermatology [79], copyright 2013.

Chapter 3

Multistep Hopping Model of Electron Transport in Bacterial Redox Chains

3.1 Introduction

Reduction-oxidation (redox) reactions and electron transport are essential to the energy conversion pathways of living cells [80]. Respiratory organisms generate ATP molecules - life's universal energy currency - by harnessing the free energy of electron transport from electron donors (fuels) to electron acceptors (oxidants) through biological redox chains. In contrast to most eukaryotes, which are limited to relatively few carbon compounds as electron donors and oxygen as the predominant electron acceptor, prokaryotes have evolved into versatile energy scavengers. Microbes can wield an astounding number of metabolic pathways to extract energy from diverse organic and inorganic electron donors and acceptors, which has significant consequences for global biogeochemical cycles [8, 22, 81].

For short distances, such as between respiratory chain redox sites in mitochondrial or microbial membranes separated by < 2 nm, electron tunneling is known to play a critical role in facilitating electron transfer [80]. Recently, microbial electron transport across dramatically longer distances has been reported, ranging

from nanometers to micrometers (cell lengths) and even centimeters [58]. A few strategies have been proposed to mediate this long-distance electron transport in various microbial systems: soluble redox mediators (*e.g.*, flavins) that diffusively shuttle electrons, conductive extracellular filaments known as bacterial nanowires, bacterial biofilms incorporating nanowires or outer membrane cytochromes, and multicellular bacterial cables that couple distant redox processes in marine sediments [30–33, 42, 47, 82, 83]. Functionally, bacterial nanowires are thought to offer an extracellular electron transport (EET) pathway linking metal-reducing bacteria, including *Shewanella* and *Geobacter* species, to the external solid-phase iron and manganese minerals that can serve as terminal electron acceptors for respiration.

Furthermore, bacterial nanowires of *Shewanella* were shown to have electron transport rates up to 10^9 s^{-1} at 100 mV of applied bias and a measured resistivity on the order of 1 Ω cm; sufficient to keep up with the typical specific respiration rates of these microbes [32]. At the same time, mutants lacking specific multiheme cytochromes (MtrC and OmcA) produce non-conductive filaments under identical conditions, suggesting that extracellular redox sites are necessary for long-range EET *via* microbial nanowires [32].

In addition to the fundamental implications for respiration, EET is an especially attractive model system because it has naturally evolved to couple to inorganic systems, giving us a unique opportunity to harness biological energy conversion strategies at electrodes for electricity generation (microbial fuel cells) and production of high-value electrofuels (microbial electrosynthesis) [26].

This chapter focuses on the theoretical basis of how biotic components such as microbial nanowires and associated multiheme *c* cytochromes form conductive

biofilms facilitating direct microbe-to-electrode EET. We build on two recent theoretical studies proposing multistep hopping in redox chains as the physical mechanism of this long-range charge transfer in *Geobacter* biofilms and *Shewanella* nanowires [35, 36]. The proposed model is based on an incoherent multistep hopping mechanism between redox sites, and an interfacial treatment of non-adiabatic (Marcus theory) electron transfer rate equations to account for the electrochemical interactions with measurement electrodes [69]. Using this model, we compute current-voltage ($I - V$) curves consistent with both transverse and longitudinal experimental measurements of *Shewanella* nanowires (published data [32, 65] and new higher-bias data reported here) as well as inter-site spacings from the recently determined crystal structure of *Shewanella* cytochromes [17].

3.2 Modeling

3.2.1 Background

Previous charge transport measurements in microbial nanowires and biofilms were performed over length scales far exceeding the size of individual cells (>1 μm) [32, 35, 47], and are therefore beyond the scope of direct single-step tunneling mechanisms relevant over much shorter distances (<2 nm) [80]. For this reason, the direct EET systems have been interpreted in light of two mechanisms: (i) fully coherent band conduction much like metals and semiconductors [47], and (ii) incoherent multistep hopping between charge localizing sites, such as redox cofactors [35, 36]. We start by considering the length and time scales involved in these physically distinct ideas, and consequently their applicability to microbial EET.

As discussed by Polizzi *et al.* [36], band conduction requires that the scattering time of the carriers, T_s, and the width of the energy band, W, satisfy the condition $T_s W \gg \hbar$ with $\hbar$ being the Planck constant. The width of the energy band can be defined as $W = 4|H_{DA}|$, where $|H_{DA}|$ is the charge transfer integral between the localizing sites in the system. At the same time, the charge mobility in band theory is $\mu_{BT} = 2er^2|H_{DA}|T_s/\hbar^2$, where e is the charge and r is the distance between localizing sites [84]. Combining these expressions results in a fundamental requirement that $\mu_{BT} \gg er^2/2\hbar$. In other words, there is a minimum mobility for the band theory picture. Even using a small separation between neighboring sites, 0.35 nm (consistent with π-stacking in conducting polymers), this requires that the mobility be far greater than ~ 1 cm^2.V.s^{-1} [36]. However, from our previous measurements of *Shewanella* nanowires [32], the conductivity is measured to be 1 S.cm^{-1} and the mobility can be estimated to be lower than 10^{-3} cm^2.V.s^{-1} [36]. While enough to sustain microbial respiration [32], this is clearly well below the band theory limit. For this reason, we contend that fully coherent band conduction is not a viable model for microbial nanowire conductivity and therefore exclude the band picture in the model and experimental measurements described below. Other aspects of the applicability of band theory to describe previously reported experimental measurements in *Geobacter* nanowires [47] (also with mobilities far below the band limit described above) have been debated elsewhere [45].

In the hopping picture, for an electron hopping process between two wells, the vibrational relaxation rate should be larger than the hopping rate for the hopping step to be independent of the preceding and succeeding hopping, *i.e.* $k_{rel} \gg k_{hop}$. This has recently been interpreted by Troisi [85] as a 'speed limit', imposing a maximum charge mobility for sequential hopping. Furthermore, this limit can be

conveniently estimated from spectroscopic measurements in organic solids since the vibrational relaxation rate is given by $k_{rel} = 2\pi c\overline{\delta}$, where c is the speed of light and $\overline{\delta}$ is the Raman line broadening [85, 86]. Using standard values for molecular materials, k_{rel} typically exceeds 10^{11} s^{-1} [85]. On the other hand k_{hop} can be estimated from the non-adiabatic rate equation for electron transfer between two sites [2]:

$$k_{hop} = \frac{2\pi}{\hbar} \frac{|H_{DA}|^2}{\sqrt{4\pi\lambda k_B T}} \exp\left[- \frac{(\Delta G + \lambda)^2}{4\lambda k_B T} \right] \tag{3.1}$$

where λ is the reorganization energy of the system, k_B is the Boltzmann constant, T is the temperature, and ΔG is the free energy change as a result of the electron transfer. This expression is frequently encountered in the simplified phenomenological form [36]:

$$k_{hop}(s^{-1}) = 10^{13} \exp\left[- \beta R - \frac{(\Delta G + \lambda)^2}{4\lambda k_B T} \right] \tag{3.2}$$

where β is the tunneling decay factor (~ 1 Å^{-1}), and R is the effective tunneling distance between two neighboring sites (the difference between the nearest neighbor hopping distance and the distance at van der Waals contact, the latter taken to be 0.35 nm). At the maximum hopping rate for efficient biological electron transfer, $\lambda = -\Delta G$, and taking $R = 0.65$ nm, a value consistent with typical inter-cofactor distances in a *Shewanella* multiheme cytochrome [17], this results in $k_{hop} = 1.5 \times 10^{10}$ s^{-1}. In summary, this rate can fall below the relaxation rate, allowing for independent hopping steps from electrode to electrode through a chain of redox sites.

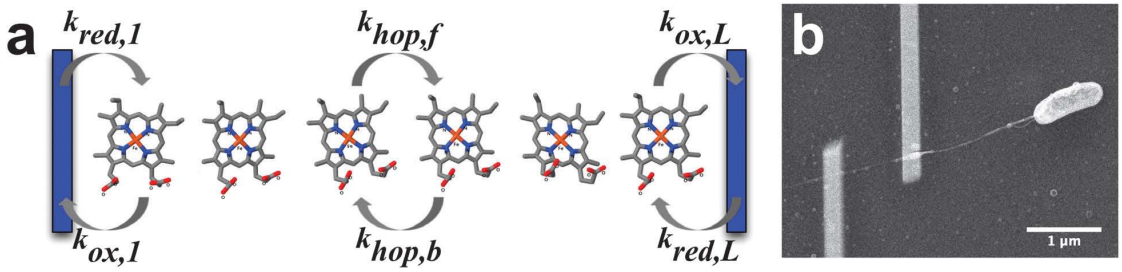

Figure 3.1: (a) A redox chain bridging two measurement electrodes. Forward and backward charge transfer rates within the redox chain are determined by $k_{hop,f}$ and $k_{hop,b}$ respectively, while the interactions with electrodes are determined by the electrochemical transfer rates k_{red} and k_{ox} at the left and right contacts. The redox sites pictured in the schematic represent hemes such as those found in the multiheme cytochromes of the dissimilatory metal-reducing bacterium *Shewanella oneidensis* MR-1. (b) Scanning electron microscopy image of an experimental platform, where two Pt electrodes address an individual microbial nanowire from a single *S. oneidensis* MR-1 cell (rod shaped cell to the right). [34] - Reproduced by permission of the PCCP Owner Societies.

3.2.2 Multistep Hopping

The multistep hopping chain model is schematically illustrated in Fig. 3.1(a), where L redox sites bridge two measurement electrodes. This picture is motivated by the experimental approaches recently used to measure the current response of one dimensional structures such as microbial nanowires when a voltage V is applied between the electrodes (Fig. 3.1(b)). The forward and backward electron transfer rates between redox sites within the chain are given by $k_{hop,f}$ and $k_{hop,b}$, both of which follow the expression for k_{hop} above but with the corresponding ΔG values of $-eV/L$ and eV/L, respectively. This electron hopping step between sites i and $i+1$ $(1 \leq i \leq L-1)$ is represented by the following reaction [35, 85]:

$$(\mathrm{i})_{\mathrm{reduced}} + (\mathrm{i}+1)_{\mathrm{oxidized}} \underset{k_{hop,b}}{\overset{k_{hop,f}}{\rightleftharpoons}} (\mathrm{i})_{\mathrm{oxidized}} + (\mathrm{i}+1)_{\mathrm{reduced}} \tag{3.3}$$

which in turns gives the electron flux between two neighboring redox sites as [35]:

$$J = k_{hop,f}P(i)[1 - P(i+1)] - k_{hop,b}P(i+1)[1 - P(i)] \tag{3.4}$$

where $P(i)$ denotes the occupation probability of site i (reduced probability) and $1 - P(i)$ denotes the vacation probability of site i (oxidized probability). The heterogeneous transfer from/to the electrodes (electrochemical oxidation and reduction of the first or L'th site) is determined using the electrochemical form of the non-adiabatic electron transfer rate equation [69], by considering the overlap between the electronic density of states in the metallic electrode, ρ (Fermi-Dirac distribution), and the Gaussian oxidation or reduction peaks of the neighboring redox site, situated $+\lambda$ and $-\lambda$ with respect to the redox potential, as illustrated in Fig. 3.2. The rates $k_{red,\eta}$ and $k_{ox,\eta}$, representing electron transfer from and to an electrode (to and from site η where $\eta = 1$ or L), are given by [36, 69]:

$$k_{red,\eta} = C_{electrode}\int_{-\infty}^{\infty}\frac{\exp\left[-\left(x - \frac{\lambda + e(E-E^0)_\eta}{k_BT}\right)^2\left(\frac{k_BT}{4\lambda}\right)\right]}{1+\exp(x)}dx \tag{3.5}$$

$$k_{ox,\eta} = C_{electrode}\int_{-\infty}^{\infty}\frac{\exp\left[-\left(x - \frac{\lambda - e(E-E^0)_\eta}{k_BT}\right)^2\left(\frac{k_BT}{4\lambda}\right)\right]}{1+\exp(x)}dx \tag{3.6}$$

where $C_{electrode} = \frac{2\pi}{\hbar}\sqrt{\frac{k_BT}{4\pi\lambda}}\,\overline{|H|^2}\rho$ and $(E - E^0)_\eta$ is the difference between the applied electrode potential (E) and the potential of its neighboring redox site (E^0) at either the left or right contact. The latter can also be represented as a local voltage drop. For example, at the left electrode, $(E - E^0)_1 = \alpha V$ where α is a fraction of the overall applied voltage V between the two electrodes. These

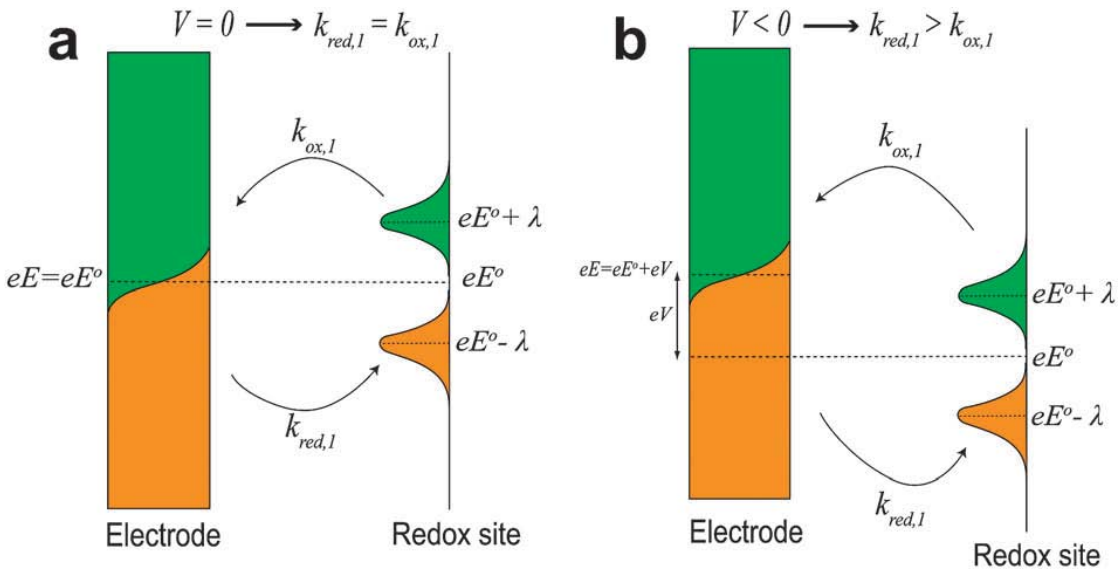

Figure 3.2: A schematic of the electrochemical interaction between the redox species and a neighboring electrode. Applying a voltage V changes the relation of the metallic states with respect to the oxidation- reduction probability peaks of the redox site. (a) When $V = 0$, the Fermi energy of the metal electrode (eE) is equivalent to the redox energy (eE^0), leading the oxidation and reduction rates to balance, and therefore the net charge transfer is zero. (b) Applying a voltage shifts the energy level of the electrode with respect to the redox level, favoring reduction or oxidation ($V < 0$ pictured, leading to increased reduction rate). [34] - Reproduced by permission of the PCCP Owner Societies.

heterogeneous transfer rates allow the calculation of the charge flux at the left and right electrodes [87]:

$$J_1 = k_{red,1}\,[1 - P(1)] - k_{ox,1}\,P(1) \tag{3.7}$$

$$J_L = k_{ox,L}\,P(L) - k_{red,L}\,[1 - P(L)] \tag{3.8}$$

Two symmetric contact electrodes will lead to the same magnitude of local voltage drop at opposite electrodes, *i.e.* $(E - E^0)_1 = -(E - E^0)_L$, which in turn

translates to $k_{red,1} = k_{ox,L}$ and $k_{ox,1} = k_{red,L}$. In addition, realizing that the charge flux from one electrode to the other is equal:

$$J_1 = k_{red,1}\,[1-P(1)] - k_{ox,1}\,P(1) = J_L = k_{red,1}\,P(L) - k_{ox,1}\,[1-P(L)] \Rightarrow P(L) = 1-P(1) \tag{3.9}$$

Finally, realizing that the flux within the chain is equivalent to the flux at the electrodes, $J = J_1 = J_L$, combining equations 3.4 and 3.9 gives the occupation probability throughout the chain as:

$$P(i+1) = \frac{k_{hop,f}\,P(i) + k_{ox,1}\,P(1) - k_{red,1}\,[1-P(1)]}{k_{hop,b} + (k_{hop,f} - k_{hop,b})\,P(i)};\ 1 \le i \le L-1 \tag{3.10}$$

Next, we apply this analysis to calculate the probability profiles and corresponding current-voltage ($I-V$) curves to compare with transverse and longitudinal transport measurements of microbial nanowires from the bacterium *S. oneidensis* MR-1.

3.3 Results and comparison to experiments

For a specific V (applied bias), L (number of sites), R (effective tunneling distance), λ (reorganization energy), α (fraction defining the contact voltage drop), $C_{electrode}$ (pre-exponential of the heterogeneous transfer rates k_{red} and k_{ox}), and k_BT (thermal energy), the model outlined above allows the calculation of the occupation probability profile throughout the redox chain, and consequently the overall current response to applied voltage. At each voltage step, the last sites occupation probability $P(L)$ can be calculated as a function of the first sites occupation probability $P(1)$, by solving equation 3.10 recursively. Combining this relation with the

symmetric constraint from equation 3.9 results in a unique value for $P(1)$, which is dependent on the transfer rates $k_{hop,f}$, $k_{hop,b}$, k_{ox}, and k_{red} (note all these rates are functions of voltage). Next, the entire probability profile $P(i)$ can be calculated from equation 3.10. We performed this calculation in MATLAB, using parameters consistent with existing transverse (small L) and longitudinal (large L) $I-V$ measurements of *Shewanella* nanowires. The results described here assume the value of k_BT at room temperature, and take 1 nm as the typical distance between the redox sites (*i.e.* $R = 0.65$ nm), consistent with the recently measured inter-heme spacings in MtrF, a multiheme cytochrome from *Shewanella* [17]. We obtained excellent fits to the experimental data by assuming an effective heterogeneous transfer rate $C_{electrode}$ smaller than the hopping rate between sites k_{hop}. For each experiment, we calculate the probability profile and the conventional (positive) current ($I = -J$) as a function of applied bias V. Finally, we fit our calculations to $I-V$ measurements, and comment on the parameters λ, α, and $C_{electrode}$ that give rise to good agreement with these experiments.

Fig. 3.3 shows the calculated probability profile for a redox chain consisting of 2000 sites as the voltage is swept from 0 to 1 V. As the voltage increases the occupation probability rapidly changes from a linear and relatively flat profile to a sharp sigmoid with high occupation probability near one electrode and a high vacation probability near the opposing electrode. With the probability profile in hand, the corresponding $I-V$ behavior is simply calculated from $I = -J_1 = k_{ox,1}\,P(1) - k_{red,1}\,[1-P(1)]$, and the result is plotted in Fig. 3.4. When $C_{electrode} \ll k_{hop}$, $P(1) \approx 1$ under positive bias, except near zero applied voltage (and similarly $P(1) \approx 0$ for negative non-small bias). Under these conditions, the current essentially follows the form of the heterogeneous electron transfer terms

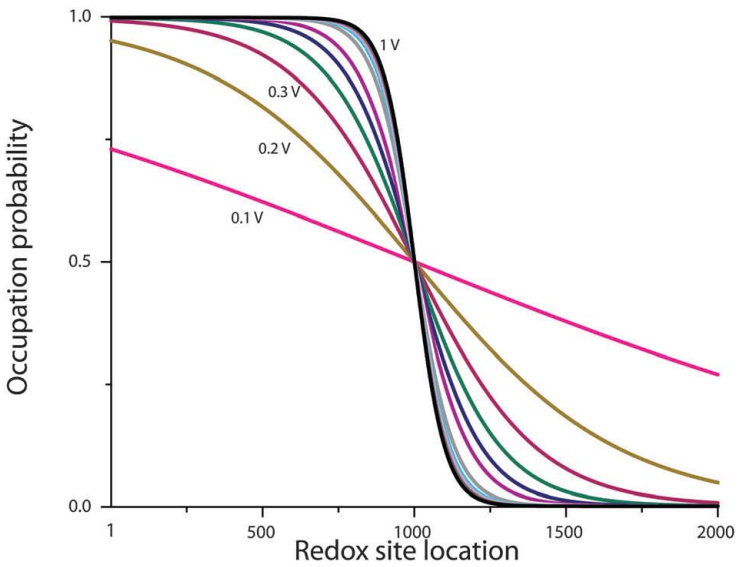

Figure 3.3: The occupation probability profile for a chain composed of $L = 2000$ redox sites as the applied voltage between the surrounding electrodes is stepped up in 0.1 V increments (corresponding to the experiment in El-Naggar *et al.* [32] and the calculated $I - V$ profiles of Fig. 3.4 and 3.5(b)). Calculation parameters: $L = 2000$, $\lambda = 0.4$ eV, $\alpha = 0.015$, $R = 0.65$ nm, $\beta = 1$ Å^{-1}, $k_BT = 0.025$ eV. [34] - Reproduced by permission of the PCCP Owner Societies.

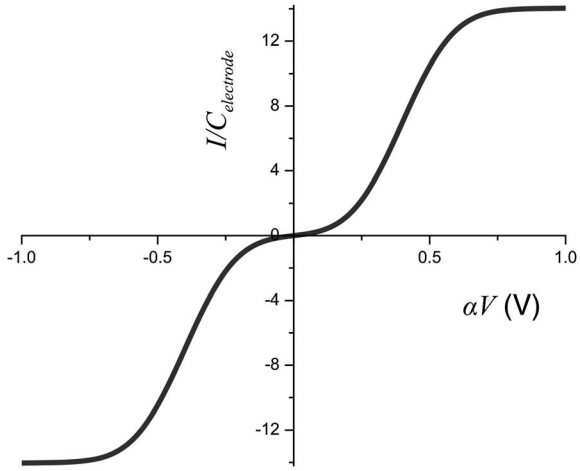

Figure 3.4: Calculated current as a function of the local electrode voltage drop for the $L = 2000$ redox chain (using equation 3.7 and the occupation probability profile of Fig. 3.3). The current reaches a constant value when the overlap between the electrode's Fermi function and the redox peaks saturates at high applied voltage. Calculation parameters: $L = 2000$, $\lambda = 0.4$ eV, $\alpha = 0.015$, $R = 0.65$ nm, $\beta = 1$ Å^{-1}, $k_BT = 0.025$ eV. [34] - Reproduced by permission of the PCCP Owner Societies.

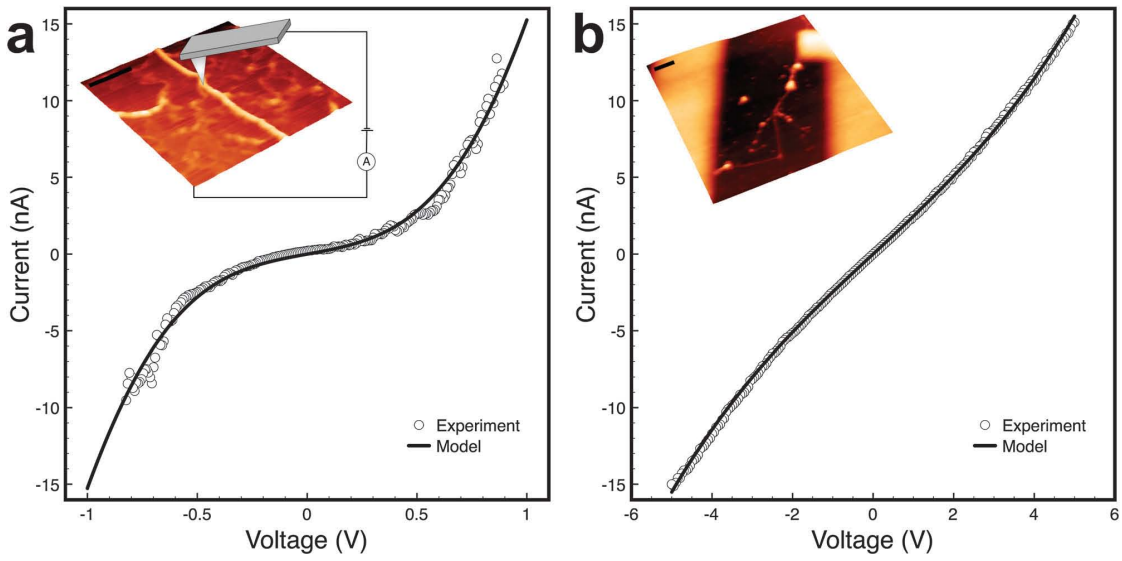

Figure 3.5: A comparison of the measured $I - V$ characteristics and modeling results for two different experiments [32, 65]. (a) Transverse transport across the thickness of a microbial nanowire ($\sim$ 10 nm), using a conductive tip as the top electrode and a supporting surface as the bottom electrode (calculation parameters: $L = 10$, $\lambda = 0.4$ eV, $\alpha = 0.3$, $C_{electrode} = 1.8 \times 10^{10}$ s^{-1}, $k_BT = 0.025$ eV). (b) Longitudinal transport along a microbial nanowire (2 μm) bridging two Pt electrodes (calculation parameters: $L = 2000$, $\lambda = 0.4$ eV, $\alpha = 0.015$, $C_{electrode} = 5 \times 10^{11}$ s^{-1}, $k_BT = 0.025$ eV). Insets show the AFM images corresponding to the measurements with 250 nm scale bars. [34] - Reproduced by permission of the PCCP Owner Societies.

equation 3.5 and 3.6, *i.e.* increasing the voltage increases the current response, until the overlap between the electrode's Fermi function and the Gaussian redox peaks saturates for very high voltages, as schematically illustrated in Fig. 3.2 and discussed elsewhere [36].

We now compare the predictions of this model to measurements of transport in conductive microbial appendages, performed using two different experimental techniques. In the first experiment [65] (Fig. 3.5(a)) transverse transport is measured across the width (10 nm, corresponding to $L = 10$ in the model) of a microbial

nanowire using a conductive atomic force microscope (c-AFM) tip as a top electrode and the underlying substrate as a bottom electrode. In the second experiment [32], longitudinal transport is measured along a nanowire using two electron/ion beam deposited electrodes separated by $2\,\mu$m ($L = 2000$). The previously reported longitudinal measurements revealed linear $I - V$ curves for low voltages (< 1 V), but the non-linearity predicted by the model appears at higher bias, as can be seen by the experimental data reported here for the same sample (up to 5 V in Fig. 3.5(b)).

For a similar voltage range, the $I - V$ measurements of the transverse and longitudinal experiments appear distinct [32, 65]. However, the model is in good agreement with both measurements, as shown on Fig. 3.5. Both experiments were fit with a reorganization energy λ close to 0.4 eV. While there are no experimental measurements of λ in *Shewanella*'s cytochromes, 0.4 eV is consistent with electrochemically determined values of λ for cytochrome c at electrode surfaces [88]. It should be noted that λ measured electrochemically, with a system probing electron transfer to electrodes, is expected to be smaller than theoretical calculations in solution without electrodes, since the electrode approach decreases the outer-sphere reorganization's (λ_{out}) solvent contribution [88, 89]. In addition, the experiments considered here were performed in air under ambient conditions.

Different $C_{electrode}$ and α parameters are expected for the two different experiments, since these parameters reflect the electronic interaction and fraction of voltage drop at the measurement contacts. In the transverse experiment, the nanowire is supported on a flat conductive surface and a metallized AFM tip is held just above the nanowire (applying a force in the nN range) [65]. The resulting transport behavior was fit using $C_{electrode} = 1.8 \times 10^{10}$ s^{-1}. In the longitudinal

experiment, Pt electrodes are directly vacuum deposited onto the nanowire surface, and this intimate electronic contact was reflected with $C_{electrode} = 5 \times 10^{11}$ s^{-1}. It is worth noting that both values are orders of magnitude higher than previously measured heterogeneous transfer rate constants of *Shewanella* cytochromes [16]. The reason for this wide discrepancy is not clear, but it may be attributed to the very different experimental conditions, namely the dry fixed environment of the microbial nanowire measurements, and the likelihood that the system does not adopt its native conformation under these conditions. By examining α, we estimate that 30% of the overall voltage drop happened at the electrode-wire contact ($\alpha = 0.3$) in the transverse measurement across 10 nm, compared to 1.5% ($\alpha = 0.015$) in the measurement along a 2 μm nanowire. Indeed, it is reasonable to expect that for a longer redox chain the local voltage drop at the electrode should be smaller, relative to the total voltage, than in a shorter chain.

Furthermore, we previously measured the contact resistance for a 600-nm long wire [32], and found that the corresponding local voltage drop at the electrode is 7% of the total applied voltage, *i.e.* giving an experimentally determined $\alpha = 0.07$ for a 600-nm chain; an intermediate value between the 10 nm and 2 μm predictions, further confirming the expected trend. With the fit parameters described here (Fig. 3.5 and Table 3.1), it is possible to calculate the voltage threshold corresponding to the saturation of transport due to the maximum overlap between the metallic Fermi function and the Gaussian redox peaks (Fig. 3.2 and 3.4). The saturation would

Measurement	R (nm)	L	λ (eV)	α	$C_{electrode}$ (s^{-1})	β ($Å^{-1}$)	k_BT (eV)
Fig. 3.5(a) - 10 nm transverse	0.65	10	0.4	0.3	1.8×10^{10}	1	0.025
Fig. 3.5(b) - 2 μm longitudinal	0.65	2000	0.4	0.015	5×10^{11}	1	0.025

Table 3.1: Simulation parameters used to model the transverse and longitudinal measurements (Fig. 3.5).

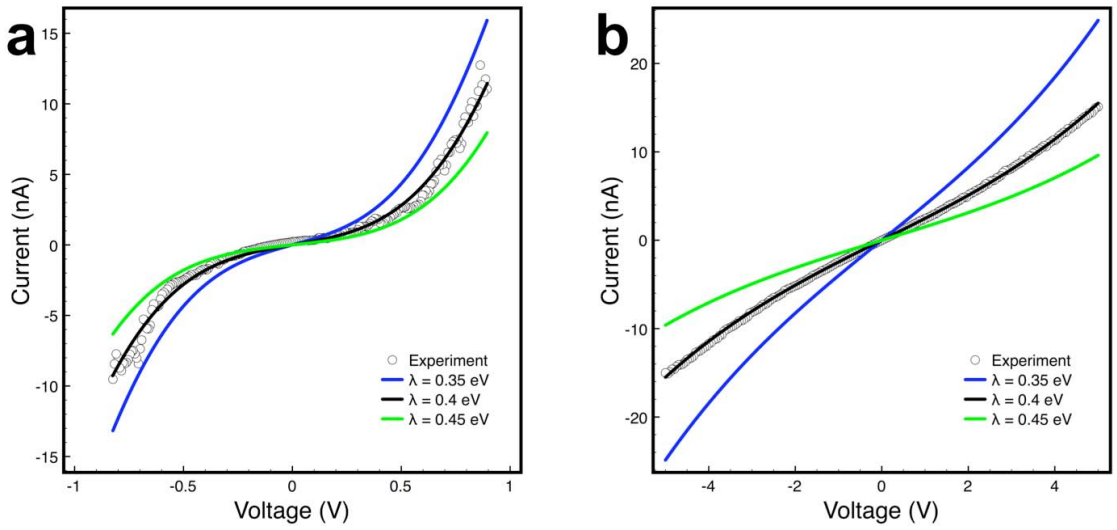

Figure 3.6: Sensitivity of the calculation to variations in the reorganization energy λ while keeping the rest of the parameters the same as Fig. 3.5/Table 3.1. (a) Transverse transport across the thickness of a microbial nanowire, using a conductive tip as the top electrode and a supporting surface as the bottom electrode (Calculation parameters: $L = 10$, $\beta R = 6.5$, $\lambda = 0.35 - 0.45$ eV, $\alpha = 0.3$, $C_{electrode} = 1.8 \times 10^{10}$ s^{-1}, $k_B T = 0.025$ eV). (b) Longitudinal transport along a microbial nanowire bridging two Pt electrodes (Calculation parameters: $L = 2000$, $\beta R = 6.5$, $\lambda = 0.350.45$ eV, $\alpha = 0.015$, $C_{electrode} = 5 \times 10^{11}$ s^{-1}, $k_B T = 0.025$ eV). [34] - Reproduced by permission of the PCCP Owner Societies.

be expected at 2.5 V and 50 V for the transverse and longitudinal measurements, respectively. These predictions are useful for designing future experiments to test and improve the model, provided that the high voltages required do not induce physical damage in the biological structures under study.

Next, we examine the sensitivity of the calculation to the model parameters. The assumption made that $C_{electrode}$ is smaller than k_{hop} places an upper limit on the effective tunneling distance R. While this assumption should be easily met for most reasonable distances that sustain tunneling because of the normally very small heterogeneous transfer rates [16] (discussed above), using our higher fit values for $C_{electrode}$ ($\sim 10^{10}$ s^{-1}), and comparing with k_{hop}, suggests an upper limit $\beta R \approx 6.9$.

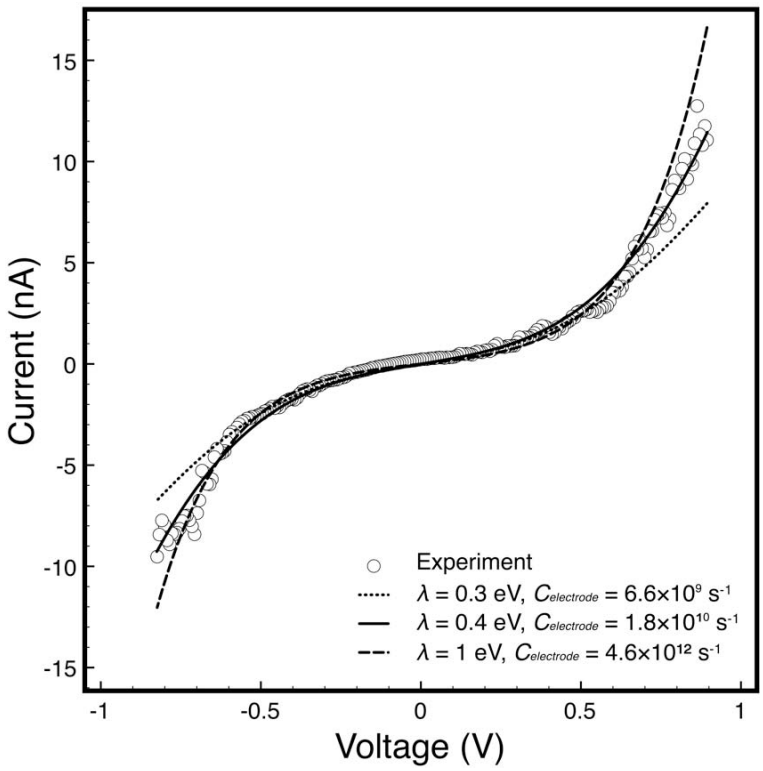

Figure 3.7: Best fits to the transverse transport measurement (c-AFM) by simultaneously adjusting the reorganization energy λ and the effective heterogeneous transfer rate $C_{electrode}$. The model fit diverges from the experimental data at high bias for $\lambda < 0.3$ eV and $\lambda > 1$ eV, regardless of the assumed heterogeneous transfer rate. [34] - Reproduced by permission of the PCCP Owner Societies.

With a typical protein decay coefficient of 1 Å^{-1}, this translates to an effective tunneling distance $R < 0.69$ nm (*i.e.* taking the van der Waals contact distance to be 0.35 nm, the nearest neighbor hopping distance is less than 1.04 nm). This result is consistent with the previous finding by Polizzi *et al.* [36], and is also met by the experimentally determined heme separation distances in *Shewanella*'s multiheme cytochromes [17]. As noted above, in this regime the predicted current response follows the form of the heterogeneous electron transfer terms equation 3.5 and 3.6, which makes the calculated $I - V$ behavior very sensitive to λ and $C_{electrode}$. Fig. 3.6 illustrates this sensitivity by showing the disagreement between model

and experiment for slightly lower and higher reorganization energies, $\lambda = 0.35$ and 0.45 eV respectively, while keeping $C_{electrode}$ fixed. However, it is possible to compensate for the variation of the reorganization energy and obtain a good fit to the experimental data by tuning $C_{electrode}$ simultaneously, but only within the range 0.3 eV$< \lambda <$ 1 eV, outside which we observe disagreement between calculations and experiments in the high bias region as shown in Fig. 3.7.

Understanding the theoretical basis of extracellular charge transfer in microbial redox chains has significant implications for elucidating the natural respiratory strategies employed by important environmental bacteria. In addition, this understanding can be harnessed towards defining the limitations and realizing the untapped potential of emerging technologies (such as biofuel cells) where these bacteria are employed as electrode-bound catalysts for driving redox reactions. In light of the multistep hopping model described here (Fig. 3.1(a)), we note that efficient EET requires a favorable interaction with electrodes (described by the heterogeneous transfer rates), which may be a limiting factor in real devices, motivating us to investigate new anode materials that maximize the electronic coupling with redox molecules. Efficient EET also requires small separations between redox sites within the chain ($\sim$ 1 nm) [17]; a requirement that seems to be satisfied by the heme-to-heme distances of individual outer membrane cytochromes. However, this hopping picture appears to be sensitive to possible structural defects in one dimension, and microbes may address this limitation through redundancy and multiple redox chains spread over cell surfaces and extracellular appendages within three-dimensional biofilms attached to electrodes.

3.4 Conclusion

In summary, we presented a model to describe charge transfer in microbial redox chains between electrodes. After reviewing the applicability of coherent band conduction and incoherent hopping to the transport measurements of microbial nanowires, we excluded band conduction as a viable model of charge transport in these structures because the measured mobilities are far below the minimum mobility set forth by the coherent mechanism. In contrast, the incoherent hopping mechanism can account for the observed transport rates as well as the form of the current-voltage curves from transverse and longitudinal measurements of microbial nanowires. The proposed model is based on an incoherent multistep hopping mechanism between redox sites, and an interfacial treatment of the electrochemical interactions with the measurement electrodes. Using this model, we computed the occupation probability profile throughout the redox chain, which allowed the calculation of the current response to applied voltage between the electrodes. We found the results to be in good agreement with two previously reported experiments measuring transport in microbial nanowires produced by the bacterium *Shewanella oneidensis* MR-1. Furthermore, the fit parameters were consistent with the length scales and electrode contact conditions of each experiment, as well as the typical reorganization energies expected from *c* cytochromes known to be critical for this organism's extracellular charge transfer ability. Our analysis motivates further experimental and theoretical investigations into the identity and structural organization of redox components in microbial systems with significant environmental and biotechnological implications.

Chapter 4

In vivo Imaging of Bacterial Nanowires of *Shewanella oneidensis* MR-1 and Their Composition and Structure

4.1 Background

A number of fundamental issues surrounding bacterial nanowires remain unresolved. Bacterial nanowires have never been directly observed or studied in vivo. Our direct knowledge of bacterial nanowire conductance is limited to measurements made under ex situ dry conditions using solid-state techniques optimized for inorganic nanomaterials [30–32, 47], without demonstrating the link between these conductive structures and the respiratory electron transport chains of the living cells that display them. Intense debate still surrounds the molecular makeup, identity of the charge carriers, and interfacial electron transport mechanisms responsible for the high electron mobility of bacterial nanowires. *Geobacter* nanowires are thought to be type IV pili, and their conductance is proposed to stem from a metallic-like band transport mechanism resulting from the stacking of aromatic amino acids along the subunit PilA [90]. The latter mechanism, however, remains

controversial [45, 83]. In contrast, the molecular composition of bacterial nanowires from *Shewanella*, the best-characterized facultatively anaerobic metal reducer, has never been reported. *Shewanella* nanowire conductance correlates with the ability to produce outer membrane redox proteins [32], suggesting a multistep redox hopping mechanism for EET [34, 36].

In this chapter, we address these outstanding fundamental questions by analyzing the composition and respiratory impact of bacterial nanowires in vivo. We report an experimental system allowing real-time monitoring of individual bacterial nanowires from living *Shewanella oneidensis* MR-1 cells and, using fluorescent redox sensors, we demonstrate that the production of these structures correlates with cellular reductase activity. Using a combination of gene expression analysis and live fluorescence measurements, we also find that the *Shewanella* nanowires are membrane- rather than pilin- based, and are associated with outer membrane vesicles. Our data point to a general strategy wherein bacteria extend their outer membrane and periplasmic electron transport components, including multiheme cytochromes, micrometers away from the inner membrane.

4.2 Experimental

4.2.1 Cell growth conditions

All *Shewanella* strains were grown aerobically in 50 mL of sterile LB broth (Sigma L3022, 20 g in 1 L of deionized water) in 125-mL flasks from a frozen ($-80\,^{\circ}$C) stock, at $30\,^{\circ}$C, shaking at 150 rpm up to an OD600 of $2.4 - 2.8$. 15 mL of the preculture was centrifuged at $4226\times$g for 5 min, the pelleted cells were washed twice, and finally resuspended in 45 mL of a defined medium consisting of 30 mM

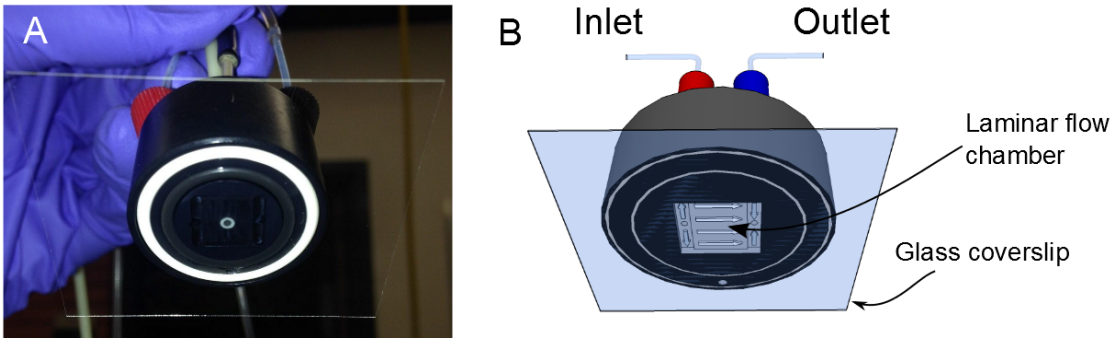

Figure 4.1: Perfusion chamber used in the *in vivo* imaging of nanowires. Chamber is closed with a glass coverslip and placed on an inverted fluorescence microscope. Laminar flow is maintained within the rectangular area at the center of the chamber.

PIPES, 60 mM sodium DL-lactate as an electron donor, 28 mM NH_4Cl, 1.34 mM KCl, 4.35 mM NaH_2PO_4, 7.5 mM NaOH, 30 mM NaCl, 1 mM $MgCl_2$, 1 mM $CaCl_2$, and 0.05 mM ferric nitrilotriacetic acid. In addition, vitamins, amino acids, and trace mineral stock solutions were used to supplement the medium as described previously [31]. The medium was adjusted to an initial *pH* of 7.2.

4.2.2 Perfusion chamber platform

Perfusion chamber

A laminar flow Vacu-Cell incubation chamber (C&L Instruments, model VC-LFR-25) was used in all perfusion and live microscopy experiments (Fig. 4.1). The chamber was constructed from black polyether ether ketone (PEEK, custom order) and modified with an additional port (0.0805 in), besides the inlet and outlet ports, that housed an Ag/AgCl reference electrode (not used in the experiments described in this thesis). An inverted 135-mL serum bottle was used to supply medium to the perfusion chamber, and a bubble trap (Omnifit, model 006BT or 006BT-HF)

placed upstream of the chamber (Fig. 4.2 and Fig. 4.3). After every time the bubble trap and tubings were exposed to the NanoOrange or the RedoxSensor Green stains, the bubble trap membrane as well as all tubings were changed and the opened bubble trap was sonicated for 10 min while immersed in ethanol to remove residual stain. Tygon S3 tubing, ID=1/32 in and OD=3/32 in, from Cole Parmer Instrument Co was used throughout. The flow of media from the serum bottle was established either by peristaltic pumping or by pressurizing the supply bottle's headspace with air or N_2 using a 6-inch septum needle, depending on whether aerobic or anaerobic conditions were desired, while the serum bottle was held slightly higher than the end of the outlet tube of the chamber. The flow rate of media through the perfusion chamber was obtained by measuring the time interval between two consecutive drops at the end of the chamber outlet tube. Using a vacuum line, the perfusion chamber was sealed against a 43×50 mm No.1 coverslip (Gold Seal catalog #: 3329) while flow of media had started and the main chamber area was covered with liquid, forming a small (250 μm deep, 17.4 μ L volume) laminar flow rectangular chamber (Fig. 4.1).

The entire perfusion set-up was taped on a Nikon Eclipse Ti-E inverted microscope stage (Fig. 4.2 and Fig. 4.3), equipped with a drift correction unit (Nikon Perfect Focus System) for maintaining focus at the coverslip-medium interface during time-lapse imaging. Washed cells were slowly injected into the perfusion chamber ($d = 250\,\mu$m, $w = 9,580\,\mu$m, $L = 7,110\,\mu$m) using a 10-mL syringe connected to the chamber inlet tube by a 4-way stopcock (Value Plastics, catalog #: VPB1000110N) and the flow was stopped to allow the cells to settle on the coverslip with a surface density of $\sim$ 100 cells in an $83 \times 66 - \mu$m field of view while being imaged by the inverted microscope. After inoculation, sterile defined

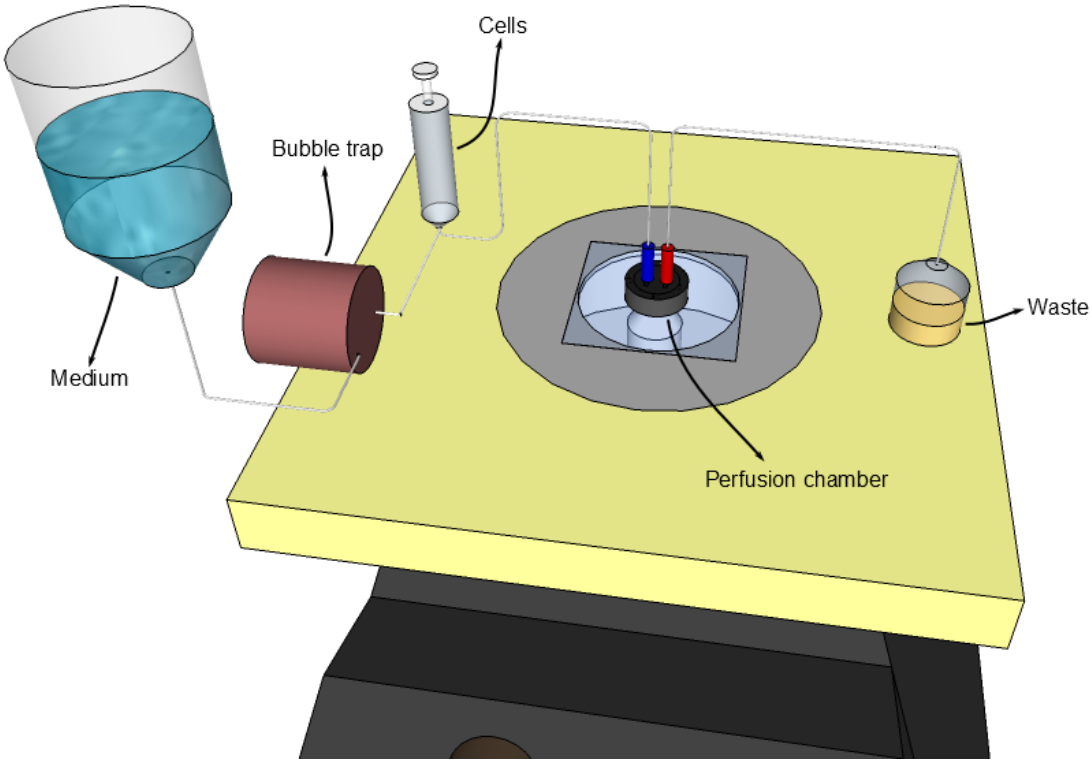

Figure 4.2: Schematic of the perfusion imaging platform. Perfusion chamber is placed on an inverted microscope stage above the objective while medium flows through the chamber from a serum bottle (left) and passes through a bubble trap. Cells are injected using a syringe connected to the inlet tube with a stopcock. Waste from the chamber flows into the waste container (right).

medium (100 mL in an inverted 135−mL sealed glass serum bottle) was connected to the perfusion chamber inlet and passed through at a flow rate of $5 \pm 1\,\mu$L/s that remained constant for 3 h.

Oxygen limitation

As previously detailed [31, 91], transition to electron-acceptor limitation was required to promote the production of bacterial nanowires and membrane vesicles; this was accomplished using one of two methods. In the first method, the

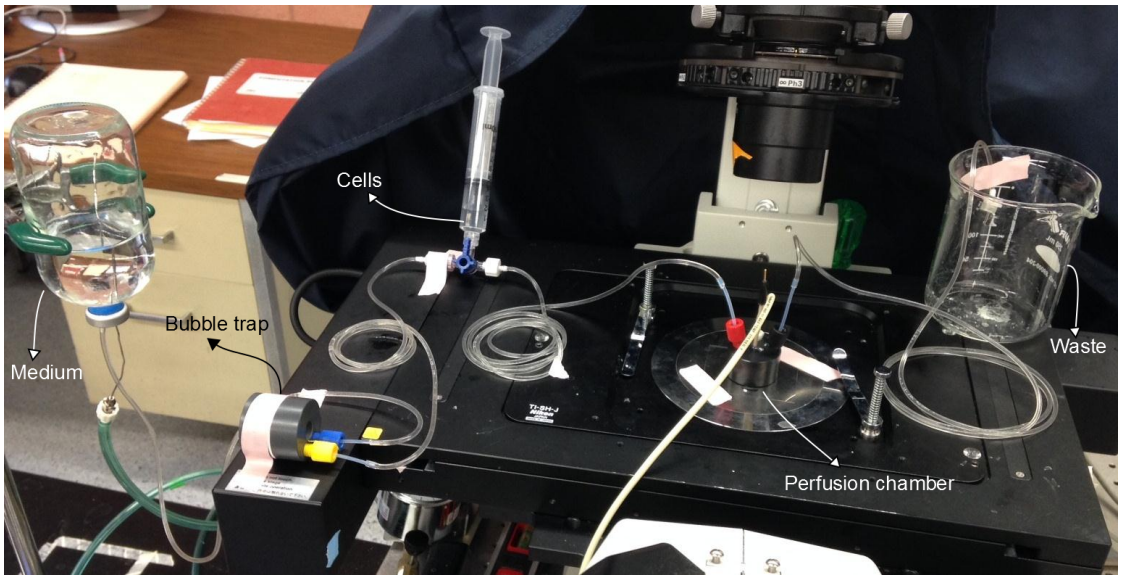

Figure 4.3: Perfusion imaging platform. Perfusion chamber is placed on an inverted microscope stage above the objective while medium flows through the chamber from a serum bottle (left) and passes through a bubble trap. Cells are injected using a syringe connected to the inlet tube with a stopcock. Waste from the chamber flows into the waste container (right).

experiment is started with fully aerobic medium flow before switching to supply bottles containing medium made anaerobic by boiling and purging with 100% N_2 (1 L of media boiled in a 2-L flask and transferred using a pump into serum bottles that were previously flushed with N_2 for 15 min, the media in serum bottles were then bubbled with N_2 for one hour). This method has the advantage of providing a precise time point for entering acceptor (O_2) limitation (Fig. 4.10A and Movies S1 and S4 in [92]). In the second method, O_2 becomes limited close to the coverslip surface at high cell density, even with aerobic medium, as a result of the laminar flow (no mixing between adjacent layers) and no-slip condition (zero velocity at the surface); this is confirmed with the simple calculation outlined below.

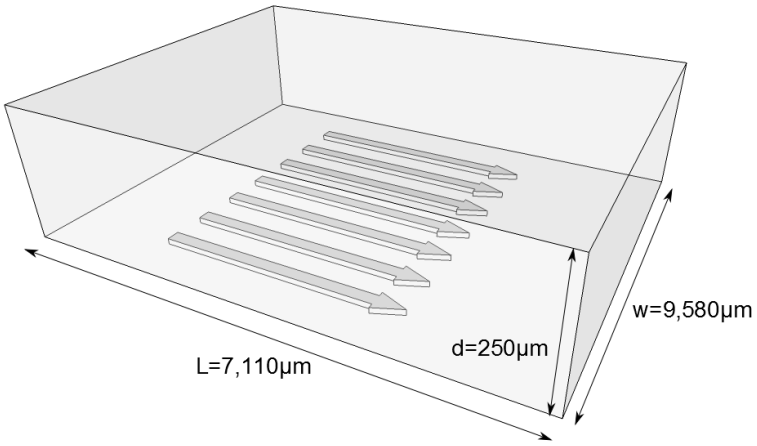

Figure 4.4: Schematic of laminar flow of medium inside the perfusion chamber along. Oxygen becomes limiting close to the coverslip due to the celluar consumption, in turn causing the production of nanowires.

For plane Poiseuille flow between two parallel plates ($w = 9,580\,\mu$m) separated by distance d ($250\,\mu$m) (Fig. 4.4), the volumetric flow rate ($5\,\mu$L/s in our experiment) is given by $Gwd^3/12\mu$, where μ is the viscosity, allowing us to estimate G, the pressure gradient in the flow direction x. In addition, the fluid velocity profile between the plates is given by $Gy(d-y)/(2\mu)$, where $0 \leq y \leq d$. Since the cells are located at the coverslip ($y = 0$), we assume that the cells interact with the $1\,\mu$m-thick layer of media adjacent to the coverslip (no mixing from upper layers) where the average flow velocity v is $25\,\mu$m/s. The O_2 concentration will consequently diminish in the x direction according to $C(x) = C_0 - \alpha \times x/v$, where C_0 is the inlet concentration (~ 8 mg/L at 100% of air saturation) and α is the cellular consumption rate which we estimate from previous studies of per cell respiration rates [32] and our surface cell density to be 0.63 mg/L/s. From this calculation, we find

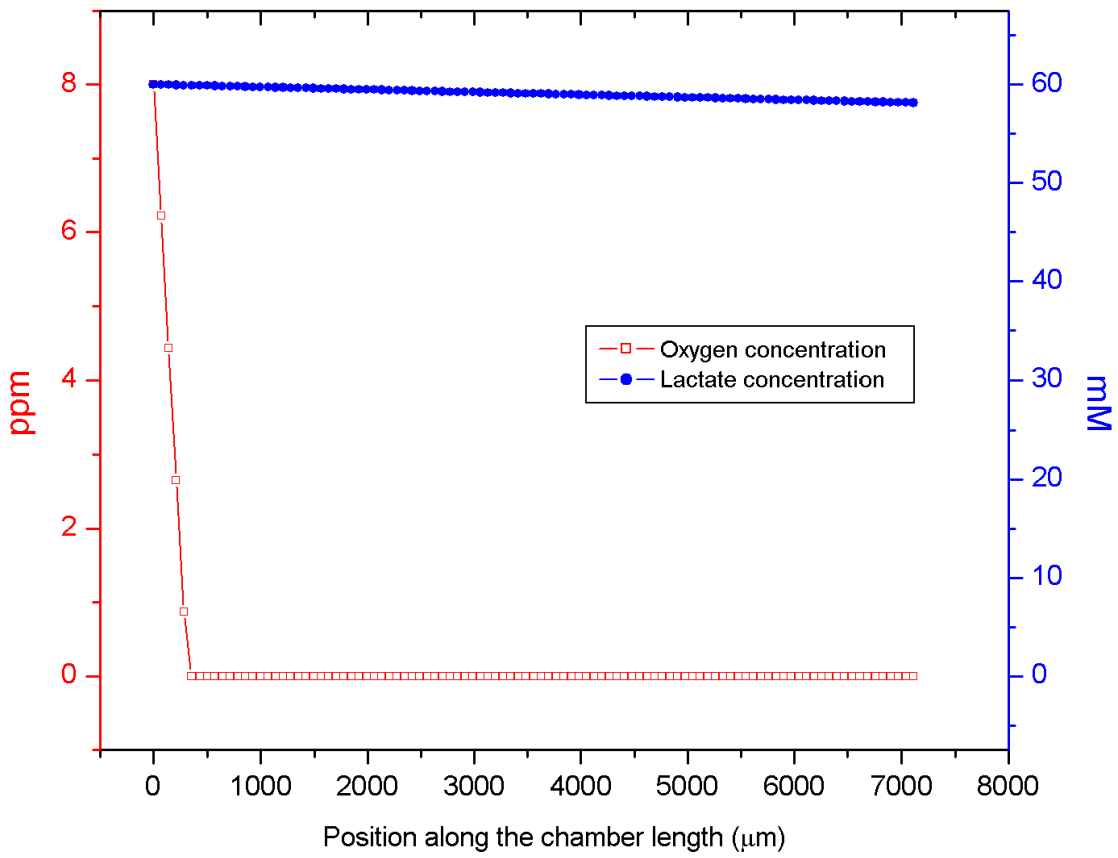

Figure 4.5: Concentration of molecular oxygen and lactate along the length (L in Fig. 4.4) of the perfusion chamber close to the coverslip. Oxygen quickly becomes limiting as medium flows from left to right inside the chamber.

that the O_2 concentration drops below 10% of air saturation at $x = 290\,\mu$m and reaches 0% at $x = 320\,\mu$m (Fig. 4.5). A similar analysis for lactate reveals that the donor concentration only drops to 96.9% of its inlet value (60 mM) at the outlet ($x = 7,110\,\mu$m) (Fig. 4.5). In other words, the majority of the surface-bound cells are acceptor, rather than donor, limited.

Using method 2 described above, nanowires and membrane vesicles were consistently observed after a lag period of 90-120 min from the start of perfusion flow

(Movies S2 and S3 in [92]). We observed higher nanowire production rates and better consistency using this method, possibly because the slower transition exposed the surface-bound cells to a wide range of acceptor concentrations, compared with the abrupt transition in the first method. Both methods resulted in identical membrane extensions as observed using membrane fluorescence (FM 4-64FX), protein fluorescence (NanoOrange), and the accompanying increase in reductase activity (RedoxSensor Green).

Fluorescence microscopy

To visualize the nanowires/vesicles by fluorescence microscopy, either the protein stain NanoOrange (Life Technologies) (Fig. 4.12A) or the membrane stain FM 4-64FX (Life Technologies) (Fig. 4.12A) was used. For each experimental run, we added 100 μL of the NanoOrange reagent or 25 μg of FM 4-64FX (dissolved in 200 μL of deionized water) to the autoclaved serum bottle containing the 100 mL of perfusion medium. Both of these fluorescent dyes allowed staining of cells, membrane vesicles, and bacterial nanowires.

Fluorescence imaging of NanoOrange and FM 4-64FX was done in the FITC (Nikon filter set B-2E/C) and TRITC (Nikon filter set G-2E/C) excitation/emission channels, respectively. The exposure time in both cases was 500 ms. Both channels were used at intensity level 2. The excitation and emission windows for both channels are described in Table 4.1. NanoOrange fluorescence was visible in both FITC and TRITC, whereas FM 4-64FX was only bright in TRITC.

Since NanoOrange has significant emission in the TRITC channel, we were not able to simultaneously stain structures with FM 4-64FX and NanoOrange. We began with FM 4-64FX in the medium, and imaged the nanowires produced by

either wild-type MR-1 or the pilus-deletion mutant strains (Table 4.2) in TRITC. We then stopped the medium flow, manually injected 10 mL of NanoOrange solution (20 μL NanoOrange reagent diluted in cell medium) using a syringe connected to the stopcock, and imaged the same structures again in the FITC channel.

4.2.3 RedoxSensor Green assay

RedoxSensor Green (from BacLight^{TM} RedoxSensor^{TM} Green Vitality Kit, Life Technologies, catalog # B34954) was used to assess cellular respiration activity. Because NanoOrange and RedoxSensor Green (RSG) reagents both fluoresced in the same channel (FITC), we could not use NanoOrange and RSG simultaneously in the same experiment. Instead, to test the impact of nanowire production on cellular reductase activity, we used FM 4-64FX and RSG to simultaneously visualize the nanowires and track the reductase activity, respectively. In these experiments, 0.3 μM RSG (30 μL of 1 mM RSG reagent in 100% DMSO) was added to the 100 mL of flow medium in the supply bottle, along with FM 4-64FX.

To measure the intensity of RSG in cells, brightness and contrast of images were linearly adjusted, equally for all cells, to capture the entire range of RSG intensity

Filter set name	**Excitation Filter Wavelengths**	**Dichromatic Mirror Cut-on Wavelength**	**Barrier Filter Wavelengths**
B-2E/C - 'FITC'	465 – 495 nm (bandpass, 480 CWL)	505 nm (longpass, LP)	515 – 555 nm (bandpass, 535 CWL)
G-2E/C - 'TRITC'	528 – 553 nm (bandpass, 540 CWL)	565 nm (longpass, LP)	590 – 650 nm (bandpass, 620 CWL)

Table 4.1: Wavelength windows of the fluorescence channels used in the perfusion chamber experiments.

in all cells. The images were then exported to MATLAB where the average pixel intensity (API, arbitrary units) of every cell was extracted by manual selection of the cell periphery and calculating the API of the pixels inside the selected periphery.

4.2.4 Verification of RedoxSensor Green as a probe for active respiration in *Shewanella*

The redox sensing functionality of RedoxSensor Green (RSG) was verified in *Shewanella* by observing fluorescence change in response to substrate activation (Fig. 4.6), as previously demonstrated for environmental samples [48]. *S. oneidensis*

Strain	**Description**	**Source**
MR-1	*Shewanella oneidensis*, wild-type	[8]
$\Delta mtrC/omcA$	MR-1 $\Delta mtrc$, $\Delta omcA$	[31]
$\Delta pilA$	MR-1 $\Delta pilA$	This work
$\Delta pilM-Q/mshH-Q$	MR-1 $\Delta pilMNOPQ$, $\Delta mshHIJKLMNEGBACDOPQ$	[93]
Plasmid	**Description**	**Source**
pHGE-P*tac*TorAGFP	Km^R, P*tac*, $TorA_{sp}$-GFP (periplasmic GFP)	[94]
p519ngfp	Km^R, P*lac*/P*npt*-2, mob^+, GFP (cytoplasmic GFP)	[95, 96]
pPROBE-NT	Km^R, broad host-range expression of GFP	[97]
pHydA-YFP	Km^R, gfp replaced with $hydA-yfp$ in pPROBE-NT	This work

Table 4.2: Strains and plasmids used in this study.

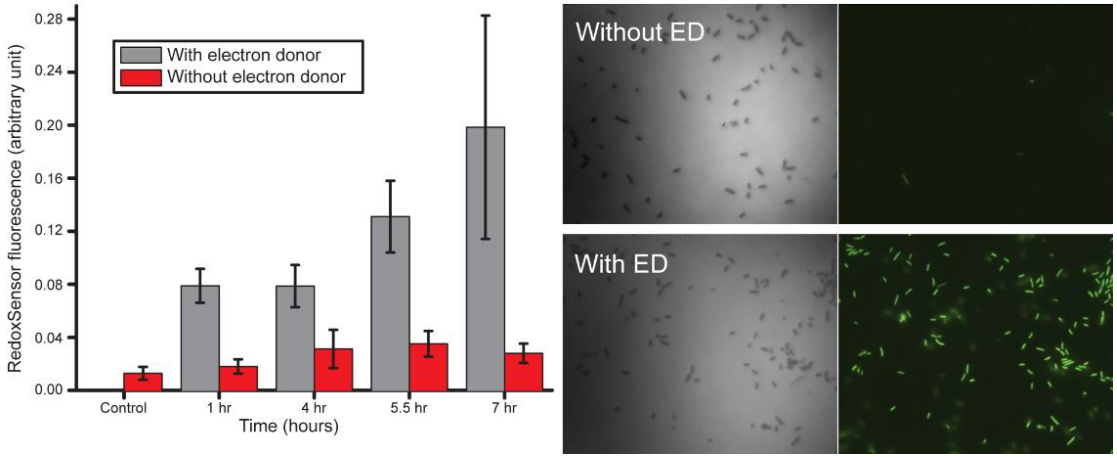

Figure 4.6: Verification of RedoxSensor Green functionality by comparing starved and electron-donor-activated *Shewanella oneidensis* MR-1 cells. A starved culture was divided into two subcultures, one of which remained starved while the other was activated with lactate as an electron donor. (A) Quantitative bar plot of fluorescence intensity of RSG in cells from subculture with electron donor (gray) and without electron donor (red) at various time points. Control refers to the initial sample that was starved for 19 hours. For each time point, images were collected from six random fields of view. The bar plot shows the average fluorescence ±SEM. (B) Representative reflection (left) and RSG fluorescence (right) images of cells from the control sample that was starved for 19 hours (top panel) and the subculture with added lactate after 7 hours of activation with lactate (bottom panel). The lactate-activated cells are all visible with fluorescence, in contrast to the starved cells not visible with fluorescence.

MR-1 cells were taken from LB culture in mid-log phase (OD600 = 1.5), washed twice and starved by incubation in defined medium without lactate or any other electron donor, for 19 hours at 30 °C and shaking at 150 rpm in 125-mL flasks. Following starvation, the cells were split into two subcultures. The first subculture was activated with 20 mM lactate, while the second culture remained starved. Both subcultures were sampled at multiple time points (1, 4, 5.5, and 7 hours after starvation) and imaged with the same microscope settings (fluorescence channel, exposure time and intensity) following incubation with 1 μM RSG reagent at 30 °C

for 40 min. Six randomly selected fields of view were imaged and analyzed at each time point.

Fluorescence intensity of cells was analyzed by image processing functions in MATLAB. The positions and exact periphery of cells were located using reflection mode (without fluorescence) and used to create a mask. The mask from the reflection image was then fit on top of the RSG fluorescence image to remove pixels lying outside the cells. The average pixel intensity (API) of the masked fluorescence image was calculated and averaged over the six fields of view, for both starved and activated samples at each time point.

The effect of three electron transport chain (ETC) inhibitors on RSG fluorescence was monitored to further confirm and localize the redox sensing functionality of RSG in *Shewanella*, as previously reported for other bacteria [49]. Rotenone, antimycin A, and sodium azide were selected because they affect respiration by inhibiting different ETC components [98]. Mid-log *S. oneidensis* MR-1 cells (OD600 = 1.5) from LB cultures were washed twice and incubated in the defined medium with 1 mM rotenone, 20 μM antimycin A, 10 mM sodium azide, or no inhibitor (control) for 15 min at 30 °C. The RSG reagent (1 μM) was added to each sample and incubated for 30 min at 30 °C. Cells from all samples were placed on a coverslip and imaged by fluorescence microscopy (Fig. 4.7) using the same settings (fluorescence channel, exposure time and intensity).

4.2.5 Cytoplasmic and periplasmic green fluorescent protein (GFP) imaging

To express GFP in the cytoplasm, *S. oneidensis* MR-1 was transformed with plasmid p519ngfp [95, 96]. The resulting strain was grown in LB augmented with

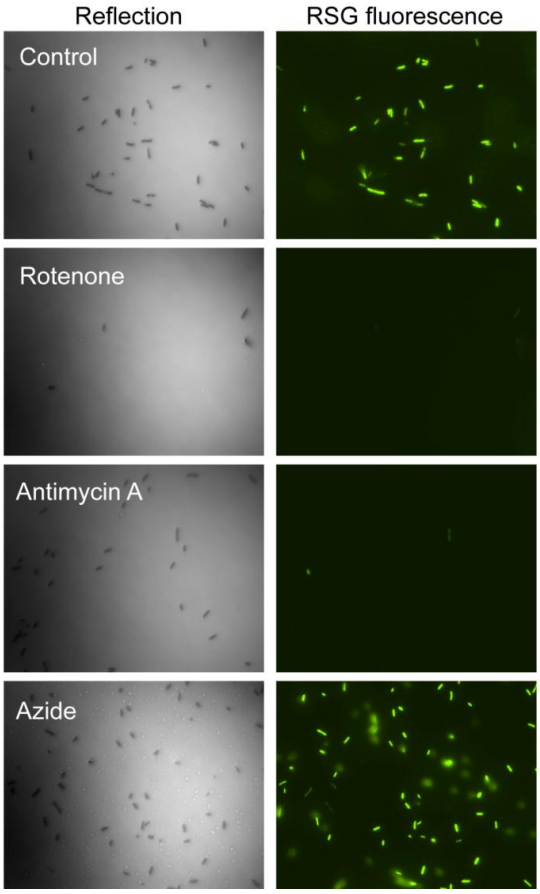

Figure 4.7: The effect of electron transport chain inhibitors on RedoxSensor Green fluorescence. *Shewanella oneidensis* MR-1 cells were incubated with no ETC inhibitor (control), 1 mM rotenone, 20 μM antimycin A, or 10 mM sodium azide. Following staining with RedoxSensor Green (RSG), both reflection and RSG fluorescence images were collected. The top panel shows the control sample without any ETC inhibitor. The second panel from the top shows cells inhibited by rotenone, with cells significantly darker than the control sample. The third panel, from the sample inhibited by antimycin A, also shows cells darker than the control. These images indicate that RedoxSesnor Green is capable of detecting the drop in respiration activity caused by rotenone and antimycin A inhibiting the ETC. However, cells inhibited by sodium azide are as bright as the control cells, indicating that RSG interacts with the ETC at a point downstream of antimycin A's site of inhibition (cyt bc1 complex), but upstream of azide's site of inhibition (cyt c oxidase).

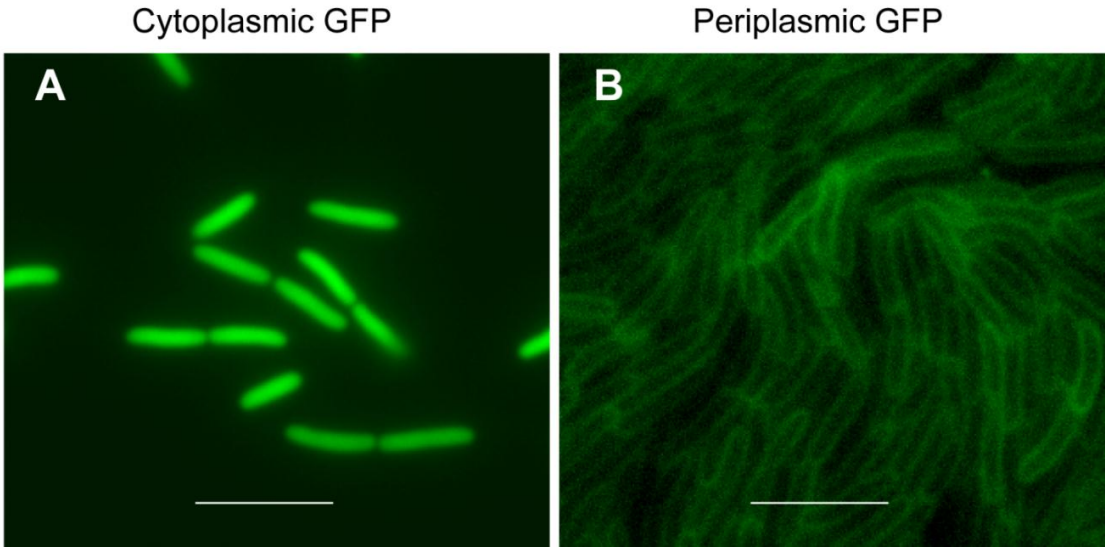

Figure 4.8: Cells containing periplasmic and cytoplasmic Green Fluorescent Protein (GFP). (A) Fluorescence image of *Shewanella oneidensis* MR-1 constitutively expressing GFP with no signal sequence for export, resulting in a uniform cellular fluorescence pattern throughout the cytoplasm. (B) *Shewanella oneidensis* MR-1 expressing GFP fused with the twin-arginine translocation (Tat) signal peptide from the *E. coli* TorA. Cells were imaged on an agar pad following LB growth and IPTG induction. Due to the presence of the signal peptide, the fusion protein is exported to the periplasm, resulting in fluorescence limited primarily to the periphery of the cell. Scale bars are 5 μm.

50 μg/mL kanamycin ahead of use in the perfusion flow imaging experiment as described above for the *S. oneidensis* MR-1. No kanamycin was added to the washing or perfusion medium.

To localize GFP to the periplasm, *S. oneidensis* MR-1 was transformed with plasmid pHGE-P*tac*TorAGFP (Table 4.2) as described previously [94]. pHGE-P*tac*TorAGFP is an IPTG-inducible plasmid expressing GFP fused to the twin-arginine translocation (Tat) signal peptide from *E. coli* TorA. Fusion to the Tat signal peptide enables GFP to be exported to the periplasm [94]. This *S. oneidensis* periGFP strain was grown in LB with 50 μg/mL kanamycin, and 0.1 mM IPTG

was added to induce the expression of TorA$_{sp}$-GFP at OD600 = 0.4 ahead of use in the perfusion imaging experiment as described above. Since the Tat system exports fully folded proteins from the cytoplasm, the cellular fluorescence pattern of this *S. oneidensis* periGFP strain is not necessarily limited to the periplasm only, and can change over time depending on the induction, export rate, or post-export cleavage of the signal peptide [94]. Therefore, to assess the successful periplasmic localization of GFP prior to use in the perfusion experiments (Fig. 4.12B), we imaged this strain on 3% agar on a slide (no nutrients or further IPTG induction) which resulted in the characteristic peripheral fluorescence pattern consistent with periplasmic localization (Fig. 4.8).

4.2.6 Chemostat growth and qPCR analysis of the transition from electron-donor to electron-acceptor limitation

S. oneidensis MR-1 was grown in chemostat medium (Table 4.3) at 30 °C, pH 7.0, and 20% dissolved oxygen tension (which was adjusted using controlled air and N_2 input) using continuous flow bioreactors (BioFlo 110; New Brunswick Scientific) (Fig. 4.9) with a dilution rate of 0.05 h^{-1} and an operating liquid volume of 1 L, as previously described [31]. After 48 h of this aerobic growth, a reference sample was taken (each sample was $\sim$ 10 mL). The dissolved oxygen tension was then manually dropped to 0% by adjusting the N_2/air mixture entering the reactor, and the first sample after electron acceptor limitation ($t = 0$) was taken at this time. O_2 served as the sole terminal electron acceptor throughout the experiment.

Samples were subsequently taken at 15-min intervals for 1 h. At each time point, 10 mL of cells were harvested in ice-cold 5% citrate-saturated phenol in

Figure 4.9: Picture of a chemostat used for analyzing the expression levels of various genes before and after production of bacterial nanowires by *S. oneidensis* MR-1 cells.

ethanol to prevent further transcription and protect the RNA. Samples were taken from three independent biological replicates (different chemostats).

The gene expression profiling was done as part of a larger collaboration with Sarah Barchinger and John Golbeck (at Pennsylvania State University, University Park) [92]. Total RNA was prepared using a hot phenol extraction, as previously described [99]. Five micrograms of total RNA from each of the time points described above was used as input for reverse-transcriptase reactions with the SuperScript III First-Strand Synthesis System, as per the manufacturers protocol (Life Technologies). Subsequent cDNA was then diluted and used as template in qPCR experiments with SYBR Select Master Mix (Life Technologies).

Fold change in gene expression relative to the reference sample was calculated by $2^{-\Delta\Delta CT}$ from at least four reactions of three independent biological replicate

Ingredient	**FW**	**g/L**	**Final concentration in media (mM)**
PIPES buffer	302.4	0.91	3
Sodium hydroxide	40	0.3	7.5
Ammonium chloride	53.49	0.53	9.9
Potassium chloride	74.55	0.1	1.34
Potassium phosphate monobasic	136.09	0.6	4.4
Sodium sulfate	142.04	0.19	1.34
Sodium lactate (60%)	112.06	3.7	19.8
Minerals solution [31]		10 mL	
Amino acids solution [31]		10 mL	
Vitamins solution [31] (after autoclaving)		10 mL	
$MgCl_2$ (after autoclaving)	95.211	0.095	1
$CaCl_2$ (after autoclaving)	110.98	0.11	1
Ferric nitrilotriacetic acid (after autoclaving)			0.05

Table 4.3: Chemostat medium.

samples, using *recA* for normalization. Similar results were obtained using *rpoB* for normalization. The sequences of the primers used for each gene are shown in Table 4.4.

4.2.7 Strains and plasmids generated for this study

Δ*pilA*: This strain was provided by our collaborators Rachida Bouhenni and Daad Saffarini (at University of Wisconsin, Milwaukee) [92]. To generate a chromosomal deletion of *pilA*, 1 kb DNA fragments that flank this gene were amplified using the primers pilAF (5'- GCATTGGCATGTCGATGAT), pilAR (5'- ATGTAAGCCTGTGGTGGGCATTTTCTCGCTCCAATACAG), pilBF (5'- CCCACCACAGGCTTACAT), and pilBR (5'- TTCGCCCACCATTACCAC). The 1 kb

Primer Name	Primer Sequence (5'-3')
RecAQF	AGCTATAGCCGCTGAAATCG
RecAQR	CCTCGACATTGTCATCATCG
RpoBQF	AGGCGTATTCTTCGATCACG
RpoBQR	AACCATGAACCACGGTAAGG
MtrCQF	CTCAAGAGTTTGCGGATGGT
MtrCQR	CATGTCGGATTCAACGTGAC
MtrAQF	CGGCACTTACCATCACAATG
MtrAQR	ATCCCACTTCGACGCATAAG
OmcAQF	AACTGTGCATCTTGCCACAC
OmcAQR	TCGCCACCTTTATGGATAGC
PilAQF	GAAAGGCCTTGCAGGATATG
PilAQR	TGCTTCAGCAACATCAGGAG
MshAQF	TGCGTCTGCATTACAAGGTC
MshAQR	TCTCCCAATGAAAAGGTTGG
PilEQF	TGGCCAATCTACAAGAGCAG
PilEQR	TCACTGAGTAATTACCGTTTTCG
FimTQF	CACGTAACACCGCAATCAAC
FimTQR	CTTCAGTGCATTGACCATCG

Table 4.4: qPCR Primers.

fragments were used as template to amplify a 2 kb fragment using cross-over PCR. The resulting 2 kb DNA that lacks *pilA* was cloned into pER21 and used to generate chromosomal deletion mutant as described previously [93].

pHydA-YFP: Also as part of our collaboration, this fusion protein was provided by Samantha Reed and Margaret Romine (at Pacific Northwest National Lab) [92]. pProbeNT-YFP was constructed by replacing the *EcoRI-NsiI* fragment encoding GFP in pProbeNT [97], with the *EcoRI-NsiI* fragment encoding YFP from pEYFP-C1 (Clonotech laboratories). A PCR product encoding *hydA* gene (SO 3920) and its upstream promoter was generated by amplification of *Shewanella oneidensis* MR-1 genomic DNA with primers 5'-gcgcTCTAGAGTCGACCATGCCGATAATCT-3' and 5'-gcgcGAGCTCGTTACCCAGCCATGAAGAGC-3'. The PCR product was digested with *SstI* and *XbaI* (sites underlined in primer sequence) and then cloned into same sites of pProbeNT-YFP, yielding pHydA-YFP. *S. oneidensis* MR-1 was transformed with this plasmid and the resulting strain, designated *S. oneidensis* HydA-YFP, was grown in LB augmented with 50 μg/mL kanamycin ahead of use in the perfusion flow imaging experiment as described above for the wild-type. No kanamycin was added to the washing or perfusion medium.

4.3 Results and discussion

4.3.1 *In vivo* imaging of nanowire formation

Previous reports demonstrated increased production of bacterial nanowires and associated redox-active membrane vesicles in electron acceptor (O_2)-limited *Shewanella* cultures [31, 32, 91]. To directly observe this response in vivo, we subjected

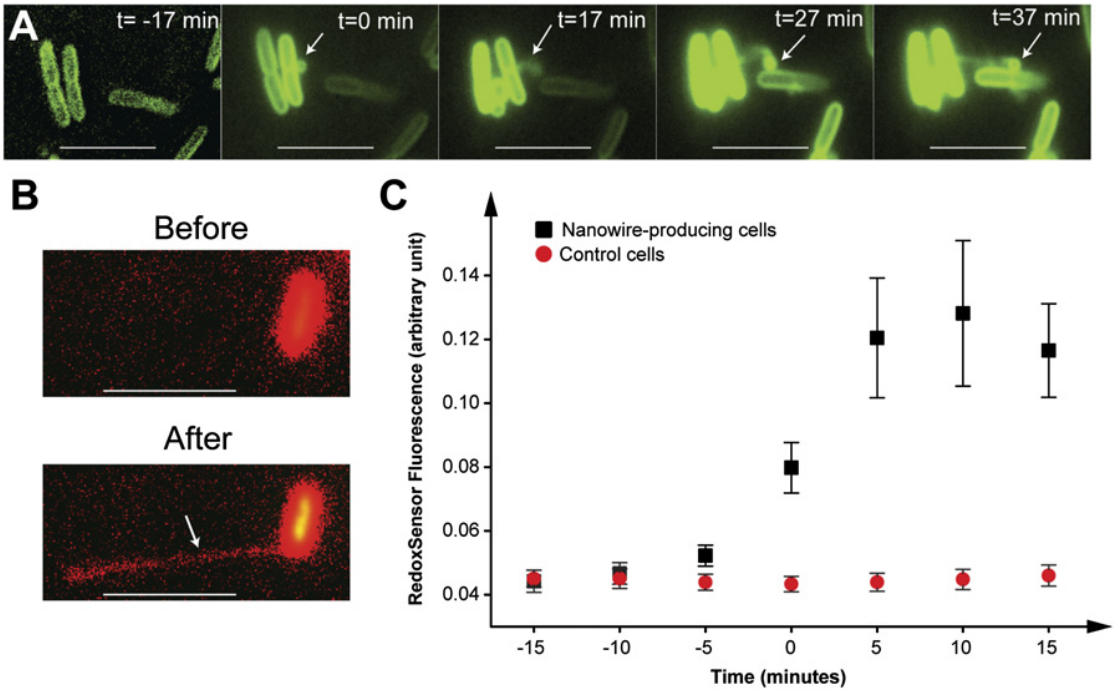

Figure 4.10: In vivo observations of the formation and respiratory impact of bacterial nanowires in *S. oneidensis* MR-1. (A) A leading membrane vesicle and the subsequent growth of a bacterial nanowire observed with fluorescence from the protein stain NanoOrange. Extracellular structure formation was first observed in the $t = 0$ frame, captured 20 min after switching from aerobic to anaerobic perfusion. (Scale bars: 5 μm.) (B) Combined green (RedoxSensor Green) and red (FM 4-64FX) fluorescence images of a single cell before and after (35 min later) the production of a bacterial nanowire. Movie S6 in [92] shows the time-lapse movie of B. (Scale bars: 5 μm.) (C) The time-dependent RedoxSensor Green fluorescence for nanowire-producing cells, compared with neighboring cells that did not produce nanowires ($n = 13$, mean cellular pixel intensity $\pm$SE). The nanowires were first observed at the $t = 0$ time point.

Shewanella oneidensis MR-1 to O_2-limited conditions in a microliter-volume laminar perfusion flow imaging platform (Fig. 4.2, Fig. 4.3 and Experimental section above) and monitored the production and growth of extracellular filaments from individual cells with fluorescent microscopy. The cells and attached filamentous appendages were clearly resolved (Fig. 4.10 and Movies S1-S4 in [92]) at the

surface-solution interface using NanoOrange, a merocyanine dye that undergoes large fluorescence enhancement upon binding to proteins [70, 71]. This dye was previously used to label bacterial nanowires recovered from chemostat cultures [31, 100]. In all our experiments, the production of filaments coincided with the formation of separate or attached spherical membrane vesicles, another observation consistent with previous electron and atomic force microscopy measurements of *Shewanella* nanowires [91]. In Fig. 4.10A, a leading membrane vesicle can be clearly seen emerging from one cell 20 min after switching to anaerobic flow conditions, followed by a trailing filament. These proteinaceous vesicle-associated filaments were widespread in all of the *S. oneidensis* MR-1 cultures tested; the response was displayed by $65 \pm 8\%$ of all cells (statistics obtained by monitoring $6,466$ cells from multiple random fields of view in six separate biological replicates). As a representative example, Movie S5 in [92] shows an $83 \times 66 - \mu$m area where the majority of cells produced the filaments. The length distribution of the filaments is plotted in Fig. 4.11, showing an average length of $2.5\,\mu$m and reaching up to $9\,\mu$m (100 randomly selected filaments from six biological replicates).

The filaments described here were the only extracellular structures observed in our experiments, and possess several features of the conductive bacterial nanowires previously reported in O_2-limited chemostat cultures. Specifically, the dimensions of these filaments [32, 65, 101], their association with membrane vesicles [91], and their production during O_2 limitation [31] led us to conclude that these structures are the bacterial nanowires whose conductance was previously measured ex situ under dry conditions [32]. Additionally, when we labeled cells grown in O_2-limited chemostat cultures with the same fluorescent dyes, we observed identical structures with the same composition as the perfusion cultures reported here (see below).

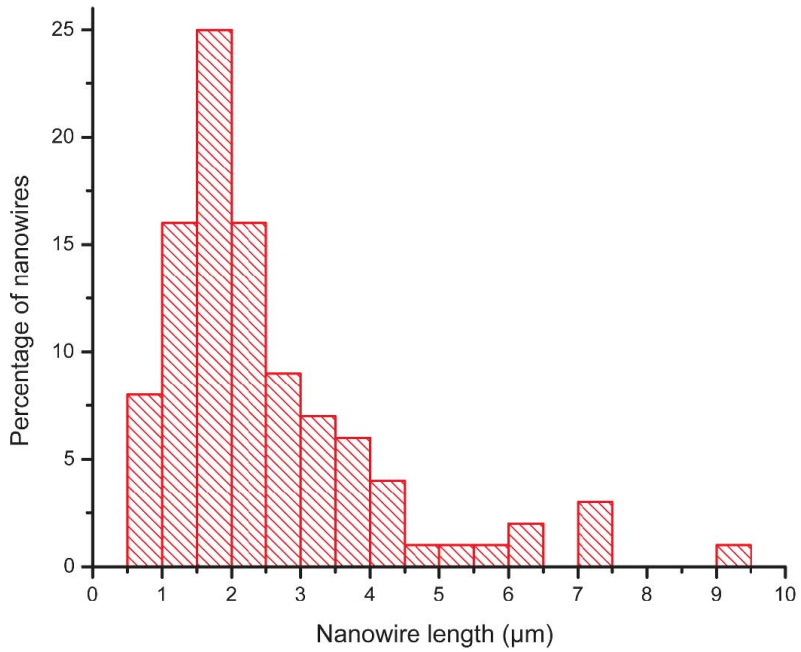

Figure 4.11: Distribution of *Shewanella oneidensis* MR-1 nanowire length. Histogram of nanowire length (100 randomly selected nanowires from 6 separate biological replicates). The average is 2.5 μm.

4.3.2 The production of *S. oneidensis* MR-1 bacterial nanowires is correlated with an increase in cellular reductase activity

To directly measure the physiological impact bacterial nanowire production has on *S. oneidensis*, we labeled cells with RedoxSensor Green (RSG) in the perfusion imaging platform described above. RSG is a fluorogenic dye that yields green fluorescence upon interaction with bacterial reductases in the cellular electron transport chain, and has been previously demonstrated to be an indicator of active respiration in pure cultures and environmental samples [48, 49, 78]. Because the redox-sensing ability of RSG was not previously characterized in *Shewanella*, we first confirmed that electron donor (lactate)-activated respiration increases RSG

fluorescence in aerobic cultures relative to starved controls (Fig. 4.6), and that the addition of specific electron transport inhibitors abolishes RSG fluorescence (Fig. 4.7). *S. oneidensis* MR-1 cells displayed a significant increase in RSG fluorescence concomitant with nanowire production (Fig. 4.10B and C and Movie S6 in [92]), indicating increased respiratory activity compared with nearby control cells that did not produce nanowires in the same field of view under identical perfusion conditions. DMSO, which is respired extracellularly by *Shewanella* [102], was available as a terminal electron acceptor in all RSG-labeled experiments.

4.3.3 *S. oneidensis* MR-1 nanowires are outer membrane and periplasmic extensions

Membrane vesicles have previously been observed to be associated with *Shewanella* nanowires [91] (Fig. 4.10A). To test the extent of membrane involvement in nanowire formation, we labeled *S. oneidensis* MR-1 cells with the membrane stain FM 4-64FX. To our surprise, the entire length of the *Shewanella* nanowires was clearly stained with this reliable lipid bilayer dye (Fig. 4.10B, red channel, and Fig. 4.12), indicating that membranes are a substantial component of *Shewanella* nanowires, contrary to previous suggestions that these structures are pilin based. We stained cells producing both nanowires and membrane vesicles with NanoOrange and FM 4-64FX, demonstrating that proteins and lipid colocalized on these extracellular structures, consistent with being derived from the cell envelope (Fig. 4.12A).

Most known bacterial vesicles are composed primarily of outer membrane and periplasm. To determine whether *Shewanella* nanowires contain periplasm, we expressed either GFP fused to a signal sequence that enables GFP export to the

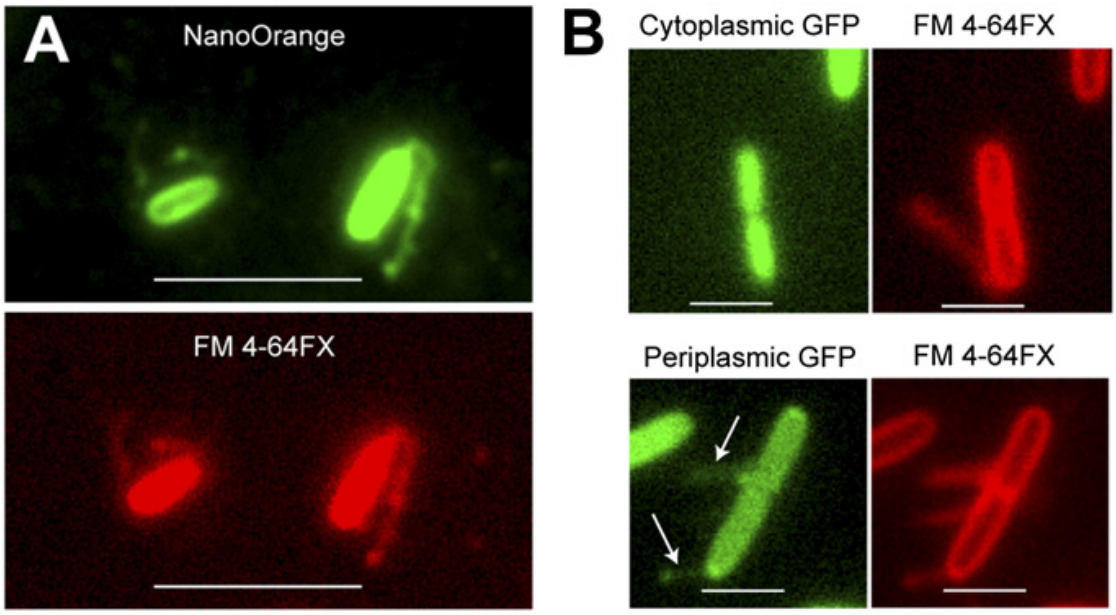

Figure 4.12: Bacterial nanowires contain lipids, proteins, and periplasm. (A) *Shewanella oneidensis* MR-1 cells and attached bacterial nanowires, stained with both NanoOrange (Upper) and FM 4-64FX (Lower), indicating the presence of proteins and membranes, respectively. (Scale bars: 5 μm.) (B) Bacterial nanowires from *S. oneidensis* MR-1 strains containing GFP only in the cytoplasm (Upper) or in the periplasm as well (Lower). The green and red channels monitor GFP and FM 4-64FX fluorescence, respectively. The nanowires display green fluorescence only when GFP is present in the periplasm (Lower Left). (Scale bars: 2 μm.)

periplasm (Fig. 4.8) after folding in the cytoplasm [94] or YFP fused to the *S. oneidensis* periplasmic [Fe-Fe] hydrogenase large subunit HydA (Experimental section above). We observed fluorescence along the bacterial nanowires in both constructs (Fig. 4.12B and Fig. 4.13). However, no fluorescence was detected along nanowires from a strain expressing cytoplasmic-only GFP (Fig. 4.12B). Taken together, these results indicate that *Shewanella* nanowires are outer membrane extensions containing soluble periplasmic components.

It has previously been proposed, but never demonstrated, that pili are important components of *Shewanella* nanowires. To test whether pili play a role in *S.*

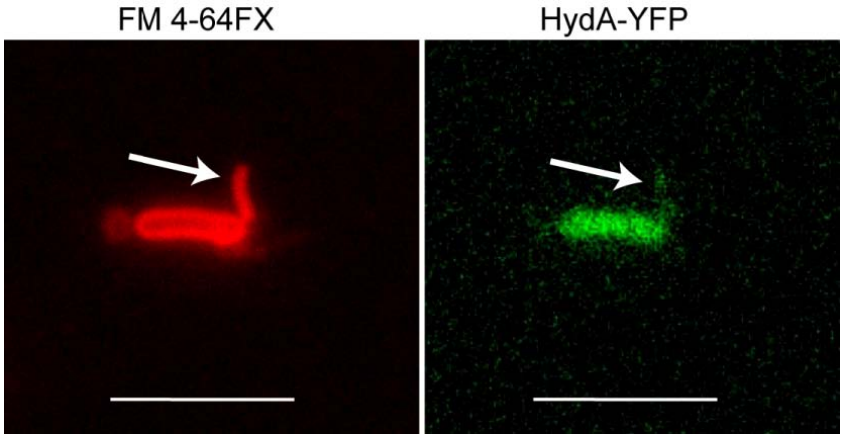

Figure 4.13: Localization of the periplasmic [Fe-Fe] hydrogenase large subunit HydA along bacterial nanowires. Images are of *Shewanella oneidensis* MR-1 cells expressing HydA fused to yellow fluorescent protein (HydA-YFP) under the control of the native *hydA* promoter. The perfusion flow imaging platform was used to monitor bacterial nanowire production (arrows). The red (left) and green (right) channels show fluorescence from the membrane stain FM 4-64FX and YFP, respectively. Brightness/contrast adjustment and bilinear interpolation was applied equally to the entire image on the right to highlight the HydA-YFP fluorescence. Scale bars are 5 μm.

oneidensis nanowire production, we harvested RNA [99] from chemostat cultures where O_2 served as the only electron acceptor, before and at time intervals after transition from electron donor (lactate) limitation to O_2 limitation. Electron acceptor limitation is known to result in increased production of bacterial nanowires, as previously demonstrated in chemostat cultures [31, 32] (and confirmed by electron microscopy). We then used qPCR to measure changes in the expression of key genes necessary for type IV pilus assembly: $pilA$, encoding the type IV major pilin subunit; $mshA$, encoding the mannose sensitive hemagglutinin (msh) pilin major subunit; and $pilE$ and $fimT$, encoding type IV minor pilin proteins. Expression of all these pilin genes either remained constant or decreased after electron acceptor limitation, when nanowire production was observed (Fig. 4.14A). Furthermore, mutants lacking the type IV pilin major subunit ($\Delta pilA$) or both the type IV and

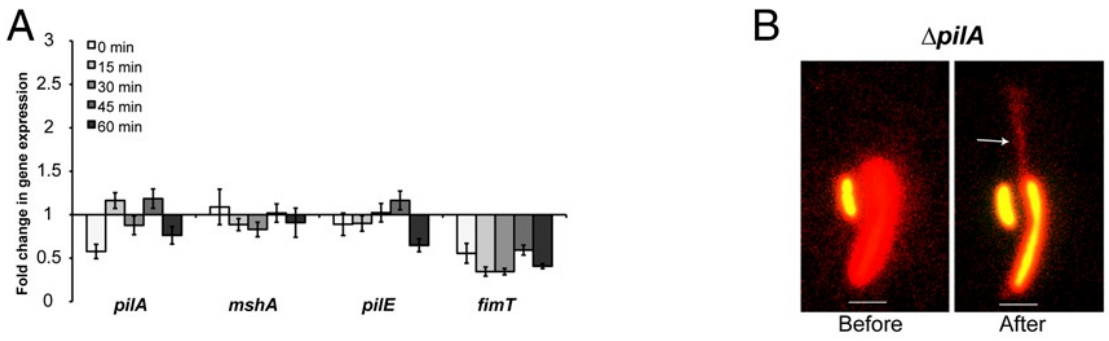

Figure 4.14: The genetic and molecular basis of bacterial nanowires. (A) Expression of pilin genes in *S. oneidensis* MR-1 measured by qPCR. Chemostat cultures were grown under aerobic conditions (dissolved oxygen tension of 20%) at 30 °C for 48 h before the dissolved oxygen tension (DOT) was reduced to 0%. Samples were harvested from cultures right before reducing the DOT ($t < 0$, reference sample), at $t = 0$, and in 15-min intervals for 1 h. The fold change in gene expression relative to the reference sample was calculated by $2^{-\Delta\Delta CT}$ from at least four reactions of three independent chemostat cultures, using *recA* for normalization. (B) Combined green (RedoxSensor Green) and red (FM 4-64FX) fluorescence images of the Δ*pilA* strain, lacking the type IV pilin major subunit PilA, before and after (95 min later) the production of a bacterial nanowire. Δ*pilA* is capable of producing bacterial nanowires with a similar respiratory impact as wild-type *S. oneidensis* MR-1, evidenced by the increase in reductase activity (green fluorescence) after nanowire production. (Scale bars: 2 μm.)

msh pilus biogenesis systems (Δ*pilM* − *Q*/Δ*mshH* − *Q*) [93] produced bacterial nanowires and displayed an increase in reductase activity in the perfusion imaging platform (Fig. 4.14B and Fig. 4.15) - a response identical to wild-type *S. oneidensis* MR-1. The chemostat qPCR and perfusion pilus-deletion observations both support the conclusion that *Shewanella* nanowires are distinct from pili.

Why were the membrane and periplasmic components of these structures overlooked in previous studies? One important factor is the difficulty of isolating the appendages and separating them from cells before downstream compositional analysis (*e.g.*, liquid chromatography-tandem mass spectrometry). In fact, membrane

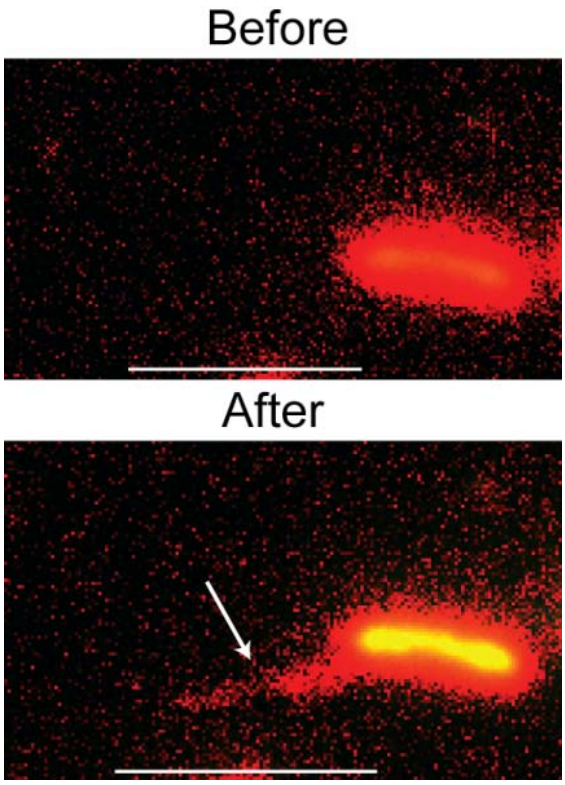

Figure 4.15: Nanowire production by $\Delta pilM - Q/mshH - Q$ and its impact on cell respiration indicated by RedoxSensor Green fluorescence. Images show combined fluorescence from membrane stain FM 4-64FX (red) and RedoxSensor Green (green) before (top) and after (bottom) nanowire production. The production of extracellular structures was correlated with a sudden increase in redox sensing fluorescence, similar to the wild-type strain. Scale bars are 5 μm.

and periplasmic proteins were previously identified in a study focused on developing optimal methods for removing the *Shewanella* filaments, although it was not possible to rule these proteins out as an artifact of the shearing procedure [103]. The present in vivo microscopy work circumvents some of the previous artifact problems by fluorescently labeling specific cellular components (protein, lipid, and periplasm) on intact nanowires attached to whole cells. In light of these new results, we revisited the chemostat samples from our previous conductance study, and noted that in those samples, SEM images also revealed vesicular morphologies,

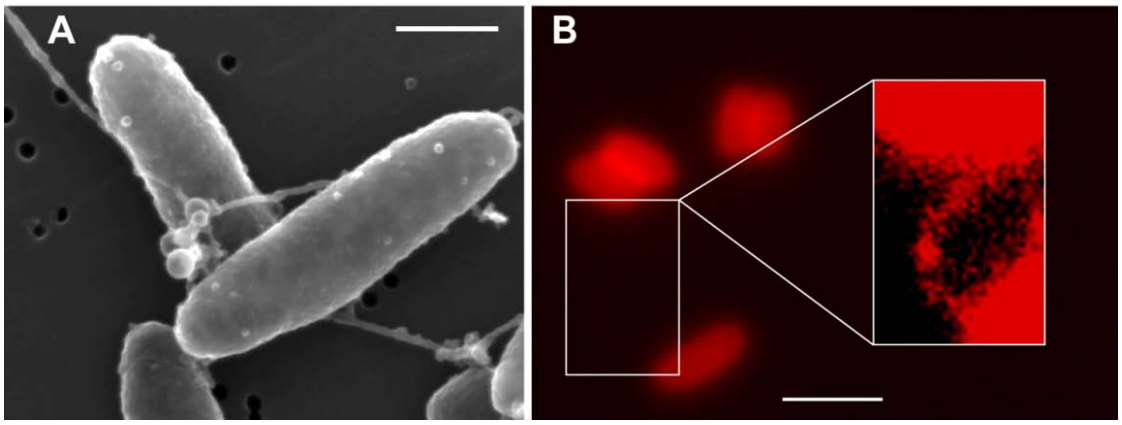

Figure 4.16: O_2-limited chemostat cultures contain membranous and vesicle-associated filaments. (A) Scanning electron microscopy of *Shewanella oneidensis* MR-1 from an O_2-limited chemostat which was previously used for nanowire conductance measurements [32]. Scale bar is 500 nm. (B) Fluorescence image of an O_2-limited chemostat sample stained by the membrane stain FM 4-64FX. A representative membranous filament is observed connecting two MR-1 cells. Brightness/contrast adjustment and bilinear interpolation was applied equally to the entire inset image to highlight the filament. Scale bar is 2 μm.

non-uniform cross-sections, and diameters $>$ 5 nm (larger than pili; Fig. 4.16A and the source-drain devices in [32]). These suggestive links did not become clear until the present in vivo results. We fixed samples from O_2-limited chemostat cultures and labeled them with FM 4-64FX. The nanowires from chemostat cultures contained both protein and membrane (Fig. 4.16B), further demonstrating that these structures are the same as those observed in the perfusion cultures in vivo. Though the net patterns of gene expression measured in the planktonic chemostat cultures may differ from the surface-attached perfusion cultures, it is important to stress that identical membrane extension phenotypes were observed in both these experiments where O_2 served as the sole electron acceptor in limiting concentrations.

4.4 Conclusion

Bacterial nanowires from *Shewanella oneidensis* MR-1 were previously shown to be conductive under nonphysiological conditions. Intense debate still surrounds the molecular makeup, identity of the charge carriers, and cellular respiratory impact of bacterial nanowires. In this chapter, using in vivo fluorescence measurements and quantitative gene expression analysis, we demonstrated that *S. oneidensis* MR-1 nanowires are extensions of the outer membrane and periplasm, rather than pilin-based structures, as previously thought. To study the physiological impact of nanowire production on *Shewanella* cells, we also demonstrated that production of bacterial nanowires correlates with an increase in cellular reductase activity. In the next chapter, in order to examine the mechanism of electron transport in *Shewanella* nanowires, we investigate the involvement of outer membrane cytochromes along these filaments.

Chapter 5

Cytochrome Localization and Nanoscale Characterization of Bacterial Nanowires

5.1 Introduction

As a metal reducer, *Shewanella* has evolved an intricate EET pathway to traffic electrons from the inner membrane, through the periplasm, and across the outer membrane to external electron acceptors, including minerals and electrodes. This pathway includes the periplasmic decaheme cytochrome MtrA, as well as the outer membrane decaheme cytochromes MtrC and OmcA, which may interface to soluble redox shuttles or, via solvent-exposed hemes, directly to the insoluble terminal acceptors [17].

However, the presence of outer membrane cytochromes along bacterial nanowires had never been directly shown before this work. Therefore, in light of the structural finding that *Shewanella* nanowires are outer membrane and periplasmic extensions (chapter 4), in this chapter we will examine whether expression of these periplasmic and outer membrane cytochromes increases during nanowire production in *S. oneidensis* bioreactors that transition from electron donor-limitation to electron acceptor-limitation.

In addition, we will use immunofluorescence to visualize and indicate the presence of specific outer membrane cytochromes along bacterial nanowires produced in the *in vivo* imaging platform described in chapter 4. After this demonstration we will examine the electron transport characteristics of single molecules of outer membrane cytochromes. This basic knowledge can serve as the buiding block for future large scale models describing the long range transport physics in bacterial nanowires. To this end, we demonstrate the development of an experimental approach to examine the basic physics of electron transfer in individual molecules of the MtrC homolog, MtrF, which is the first outer membrane cytochrome with a solved crystal structure. Monolayers of MtrF are produced and the monolayer properties are investigated using scanning tunneling microscopy (STM). The approach developed here can be used in future in combination with tunneling spectroscopy (TS) I-V measurements to examine electron transfer characteristics of individual MtrF molecules.

During *in vivo* imaging of bacterial nanowire formation, ocassionally we observed the initial growth of a vesicle chain that later transitioned into a smoother filament. In addition, it had been previously shown that bacterial nanowires are typically associated and attached to outer membrane vesicles in *Shewanella* [91]. To investigate the involvement of outer membrane vesicles in nanowire formation, and to gain a more accurate estimate of the morphologies and dimensions of bacterial nanowires, we performed atomic force microscopy (AFM) as well as transmission electron microscopy (TEM) on nanowires previously produced in the *in vivo* imaging platform described in chapter 4. This technique revealed the intermediate steps in the formation of nanowires and demonstrated the true dimensions of these filaments.

5.2 Experimental

5.2.1 Immunofluorescence with MtrC or OmcA antibody

S. oneidensis MR-1 and Δ*omcA*/*mtrC* (Table 4.2 in chapter 4) were used in the perfusion chamber experiment as described in chapter 4. As soon as the nanowires were produced and observed through staining by FM 4-64FX, the media flow was stopped and the chamber was opened in a petri dish containing 20 mL of sterile medium such that the coverslip remained hydrated. The sample (coverslip with attached cells) was cut to retain only the area corresponding to the laminar flow region of the chamber and was fixed with 4% (vol/vol) formaldehyde solution in PBS (at pH 7.4) for 1 h at room temperature (RT). After rinsing in PBS (each rinse corresponds to incubation in fresh PBS for 30 seconds), the sample was incubated in 0.15% glycine in PBS at RT for 5 min to quench free aldehyde groups and reduce background fluorescence. The sample was then transferred to a blocking solution of 1% BSA in PBS for 5 min, and reacted with the diluted polyclonal rabbit-raised MtrC or OmcA-specific primary antibody [104] at RT for 30 min (MtrC Ab: 2.6 μg/mL, OmcA Ab: 1.9 μg/mL, both in 1% BSA/PBS). The MtrC and OmcA-specific primary antibodies were provided by our collaborator Liang Shi (at Pacific Northwest National Lab). After rinsing four times in PBS, the sample was incubated with anti-rabbit FITC-conjugated secondary antibody (Thermo Scientific Pierce antibodies, catalog no. 31635; 7.5 μg/mL in 1% BSA/PBS) at RT for 30 min. Finally, the coverslip was rinsed twice in PBS before immunofluorescence imaging in the green channel while the side of the coverslip with cells remained hydrated on the microscope. To perform immunofluorescence on the same cells and

nanowires observed during live imaging (Movies S7 and S8 in [92] and Fig. 5.4), we modified the coverslips with surface scratches that acted as fiducial markers.

5.2.2 Preparation of MtrF monolayers on Au(111)

A 4×Cys/V5/6×His tag (DDDDKAACCPGCCKGKPIPQPLLGLDSTRTGHH-HHHH) was added at the C-terminus of MtrF to make the recombinant MtrF used in this study. This tag allowed purification of the protein, while its cysteine residues established covalent bonds between the recombinant protein and gold surfaces. As was described previously for recombinant MtrC [105], we prepared a construct with a gene encoding this recombinant MtrF, resulting in the construct (pLS289) which was then introduced into *S. oneidensis* MR- 1 to give LS622 [106]. Using the protocol described in [17], we overexpressed LS622 and then purified the tetra-cysteine tagged MtrF. The purified MtrF (1.7 mg/mL) was divided into 100 μL aliquots, stored at -20 °C in 20 mM HEPES-buffered solution with protease inhibitor, 10% glycerol, 250 mM NaCl, 1% OGP, and 5 mM β-mercaptoethanol at pH 7.6. Using a fresh buffer solution of 20 mM OGP and 50 mM HEPES at pH 7.6, we exchanged the solution twice by centrifuging at 14,000 rcf at 10 °C in Amicon Ultra-0.5 mL centrifugal filters (10 kDa molecular weight cut-off), as described previously [61]. We then fourfold diluted the extracted solution containing MtrF with deionized water.

The diluted solution was carefully deposited on atomically flat Au(111) substrates (Agilent annealed N9805B) (Fig. 5.1). These gold surfaces are made by Au(111) evaporation onto a 50 to 75 μm thick mica substrate that is 1.4×1.1 cm in size. The gold surface itself is 1.0×1.1 cm and is then flame-annealed to give atomically flat terraces that are several hundred nanometers across. The Au(111)

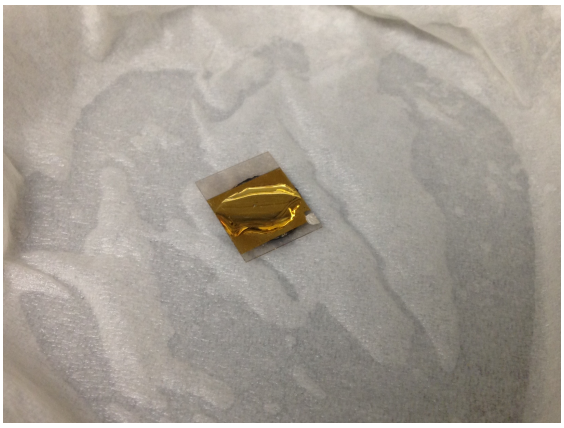

Figure 5.1: Deposited MtrF solution on atomically flat Au(111) substrate. The substrate along with the deposited solution is placed on top of wet Kimwipes and inside a closed petri dish for 15 hours at 4°C.

substrate along with the solution were incubated for 15 hours at 4 °C while sitting on wet Kimwipes inside a closed petri dish. Before STM measurements, the majority of the solution was removed from the surface using a pipette applied to the corner, followed by wicking to minimize the remaining solution on the surface. The substrate and surface-adsorbed MtrF layer were then left at room temperature and ambient humidity for about 2 hours to dry. The sample was then attached to an 18-mm diameter mounting disk (Bruker Product #:APSH-0010) by applying silver paint between the mounting disk and the bottom of the mica substrate. The electrical connection between the gold and the mounting disk was achieved by extending the silver paint over the mica surface and to the corner of the gold surface. The sample was then left to dry for 15 mins at room temperature.

5.2.3 Scanning tunneling microscopy of MtrF monolayers

A Bruker Innova AFM/STM was used in combination with 80/20 Pt/Ir STM tips (Bruker CLST-PTBO) to perform STM measurements. Initially 500×500 nm areas

of the dried MtrF sample were scanned while the STM tip was held at a more positive potential (+1 V) than the substrate with a tunneling current setpoint of 2 nA. These scans showed 'pits' in the MtrF monolayer (Fig. 5.6B), similar to the features previously observed in MtrC and OmcA monolayers [61]. Subsequently the STM tip-substrate potential difference was reversed and the same area was scanned while the STM tip was held at -3V with respect to the substrate, with a 2 nA tunneling current setpoint. As suggested with MtrC and OmcA monolayers [61, 107], this second scan 'activated' the MtrF monolayer by removing the OGP overlayer that was covering the MtrF proteins. The tip potential and current setpoint were then changed back to the initial values (+1 V and 2 nA) and the activated area was scanned for a third time, revealing individual MtrF molecules forming a uniform monolayer on the atomically flat terraces of the Au(111) substrate.

5.2.4 Atomic force microscopy following live perfusion flow imaging

Following in vivo imaging of vesiculation and nanowire growth under perfusion flow conditions, samples were imaged by atomic force microscopy (AFM) to correlate fluorescence and nanoscale topography data (Fig. 5.7). Each sample (coverslip and attached cells) was fixed in 2.5% glutaraldehye overnight at 4 °C. The sample was rinsed four times in deionized water (each rinse was a 30-sec incubation in DI-water) and left to air dry. The coverslip was then cut and prepared for AFM imaging. The AFM imaging was performed using a tapping mode tip (Asylum Research, silicon probe model AC240TS with 2 N/m nominal spring constant) on a Veeco Innova instrument. Scratch marks previously placed on the coverslips

acted as fiducial markers, allowing us to perform AFM on the same cells and nanowires observed during live cell growth.

5.2.5 Transmission electron microscopy following nanowire formation in the *in vivo* imaging platform

After production of nanowires by the cells attached to the coverlips in the *in vivo* imaging platform was confirmed, the perfusion chamber was opened in a Petri dish containing 20 mL of 1× Phosphate Buffer Saline (PBS) at pH=7.4. The coverslip was then cut to only retain the area corresponding to the laminar flow region of the perfusion chamber (rectangular area in Fig. 4.1). The sample was then left in a 4% (vol/vol) formaldehyde solution in PBS for 1 hour. The sample was then washed in 100 mM (pH 7.2) sodium cacodylate buffer by soaking 5 times in the solution. Afterwards, the coverslip was soaked in 1% aqueous osmium tetroxide for 30 min, washed with deionized water and then soaked again for 30 min in reduced osmium (the same osmium solution used before but containing 0.3% potassium ferrocyanide, from a 3% aqueous solution).

The coverslip was washed with deionized water and then quickly passed through increasing concentrations of ethanol (30%, 50%, 70%, 80%, 90% and 100%) and given two extra changes in 100% ethanol. The sample was then soaked in a 50:50 mix of dry ethanol and epoxy resin (Eponate 12 kit from Ted Pella, with a formulation that made a harder rock). No catalyst was added to the resin mixture for soaking. After the coverslip was left for an hour in the mixture, the resin amount was increased to a 1:3 ratio of ethanol to resin (no catalyst used).

After soaking the sample overnight, the old resin:ethanol mix was washed away and was replaced by fresh resin that contained N,N-Dimethylbenzylamine (BDMA)

as a catalyst. Next, the back side of the coverslip was wiped, small gelatin capsules (Electron Microscopy Sciences, gelatin capsules, catalog #: 70104) were filled and the excess resin was blotted off from the specimen side. The filled capsules were then inverted onto the coverslip to embed the specimen in resin. The resin was polymerized by heating overnight in a 60 °C oven. Polymerized resin blocks were removed from the oven and the glass substrate was removed from the resin. This was done by breaking the glass and separating the resin blocks. The resin with glass attached was repeatedly immersed in liquid nitrogen and warmed up, until the glass fell away from the resin. Anything that was initially on the glass surface was embedded in the resin, but only at the top face of the block.

To section the bacteria that were initially on the glass coverslip surface, the block was put into an ultramicrotome (Leica UC 6) and the front of the block was cut with a diamond knife (Diatome: EMS). The knife was positioned so that it was not perfectly aligned with the block face, but was offset to only cut a band from the block on one side. All sections were collected and mounted on Formvar-coated single slot grids (Electron Microscopy Sciences, catalog#:G205-Cu), contrasted with 3% aqueous uranyl acetate, washed in a jet of water, and contrasted again with an aqueous solution of lead citrate (Reynolds recipe [108], but modified by Venable and Coggeshall [109]). The lead citrate was EM grade which was prepared fresh as follows: 0.1 g lead citrate was dissolved in 1 mL of 1 N sodium hydroxide and made up to 10 mL. The grids were contrasted by floating them, section-side down on drops of the heavy metal solution and then dipping them in degassed water 10× sequentially in 4 different beakers. The first beaker (10 mL) contained 1 drop of 1 N sodium hydroxide.

The grids were dried and imaged with a Tecnai BioTwin Spirit operating at 120 kV (FEI Company, Hillboro, OR).

5.3 Results and discussion

5.3.1 Localization of the decaheme cytochromes MtrC and OmcA along nanowires

We measured the expression levels of *mtrA*, *mtrC*, *omcA*, and *dmsE*, a periplasmic decaheme cytochrome required for maximal extracellular respiration of DMSO [102], during and after the transition to O_2 limitation in chemostat cultures. These EET components had significantly increased expression in response to electron acceptor limitation (Fig. 5.2 and Fig. 5.3).

Using MtrC- and OmcA-specific antibodies [104] following in vivo observation of the target nanowires in the perfusion imaging platform (Movies S7 and S8 in [92]), we observed MtrC and OmcA localization at the periphery of the cell, as expected. We also observed clear localization of these cytochromes along the membrane-stained bacterial nanowires (25 of 35 nanowires labeled with anti-MtrC and 19 of 22 nanowires labeled with anti-OmcA), whereas no fluorescence was detected from $\Delta mtrC/omcA$ negative control cells or their membrane extensions (none of 22 nanowires labeled with anti-MtrC and none of 20 nanowires labeled with anti-OmcA; Fig. 5.4).

Though the conductance of *Shewanella* nanowires was previously only demonstrated under nonphysiological conditions [32], the data reported here are consistent with membrane extensions that could function as nanowires to mediate EET from live cells. Localization of MtrC and OmcA to these membrane extensions

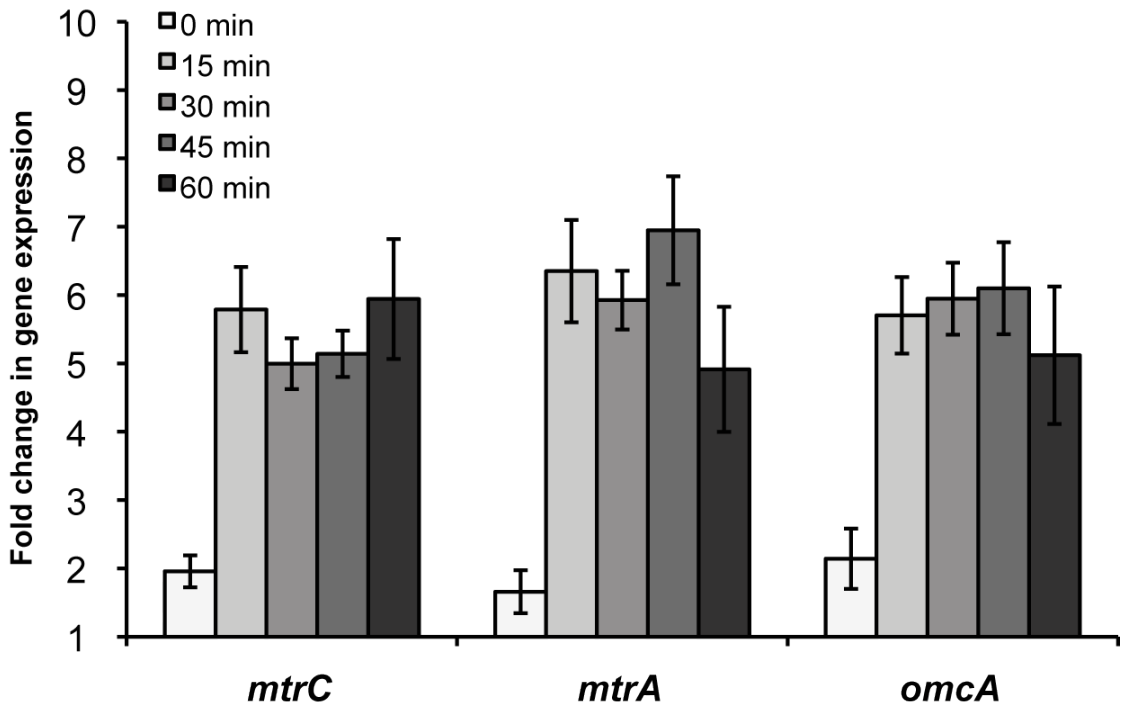

Figure 5.2: Profiling of *mtrC*, *mtrA*, and *omcA* expression during transition from electron donor to electron acceptor limitation. *Shewanella oneidensis* MR-1 cells were grown under aerobic conditions (dissolved oxygen tension of 20%) at 30 °C in a chemostat for 48 hours before the dissolved oxygen tension was reduced to 0% ($t = 0$). Samples were taken from the chemostat right before reducing the DO tension ($t < 0$, reference sample), at $t = 0$ and in 15-minute intervals for an hour. Following RNA purification and qPCR, the fold change in gene expression relative to the reference sample was calculated by $2^{-\Delta\Delta CT}$ from at least four reactions of three independent cultures, using *recA* for normalization.

provides the most compelling evidence to date, and directly supports the proposed multistep redox hopping mechanism [34, 36, 83], allowing long-range electron transport along a membrane network of heme cofactors that line *Shewanella* nanowires (Fig. 5.5). We have shown that *S. oneidensis* nanowires contain periplasm (Fig. 4.12B in chapter 4); therefore, it is also possible that periplasmic proteins and soluble redox cofactors may contribute to electron transport through these extensions.

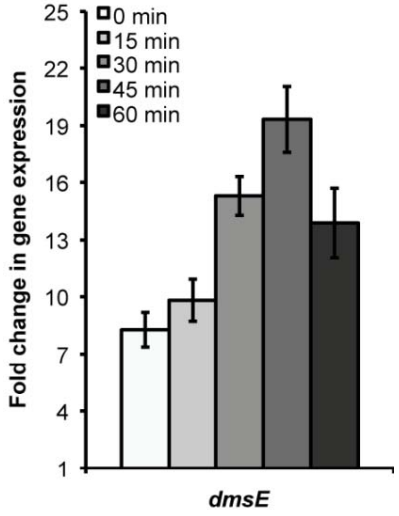

Figure 5.3: Profiling of *dmsE* expression during transition from electron donor to electron acceptor limitation. *Shewanella oneidensis* MR-1 cells were grown under aerobic conditions (dissolved oxygen tension of 20%) at 30 °C in a chemostat for 48 hours before the dissolved oxygen tension was reduced to 0% ($t = 0$). Samples were taken from the chemostat right before reducing the DO tension ($t < 0$, reference sample), at $t = 0$ and in 15-minute intervals for an hour. Following RNA purification and qPCR, the fold change in gene expression relative to the reference sample was calculated by $2^{-\Delta\Delta CT}$ from at least four reactions of three independent cultures, using *recA* for normalization.

5.3.2 Proof of concept for single-molecule electron transfer measurements in MtrF

Considering previous findings pointing at a long range electron transport in bacterial nanowires facilitated by cytochromes [31, 32], we aimed at developing a method to examine, at the single-molecule level, the electron transfer properties of outer membrane cytochromes. This basic understanding is a fundamental step toward building models that describe the entire system of cytochromes mediating the long range electron transfer in bacterial nanowires.

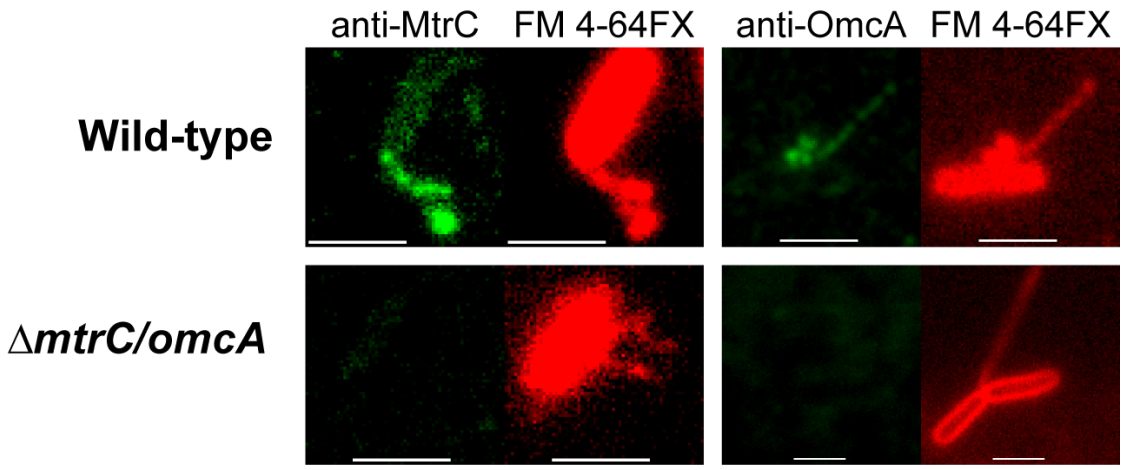

Figure 5.4: Involvement of outer membrane cytochromes in bacterial nanowires. Labeling with antibodies against MtrC (Left) or OmcA (Right) and membrane fluorescence (FM 4-64FX) images of wild-type *S. oneidensis* MR-1 (Upper) compared with the Δ*mtrC*/*omcA* control strain (Lower). Nanowire-localized MtrC and OmcA are observed in the wild-type strain. (Scale bars: 2 μm.)

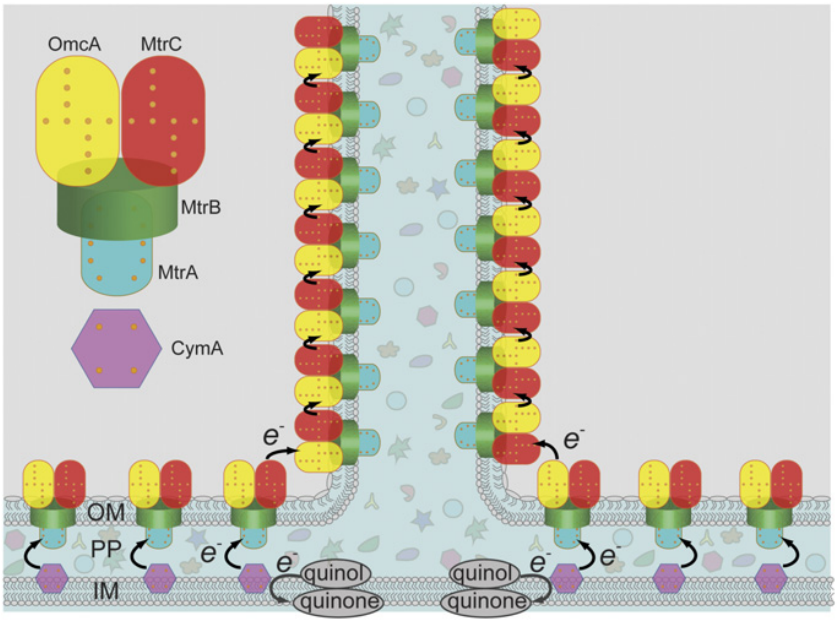

Figure 5.5: Proposed structural model for *Shewanella* nanowires. *S. oneidensis* MR-1 nanowires are outer membrane (OM) and periplasmic (PP) extensions including the multiheme cytochromes responsible for extracellular electron transport.

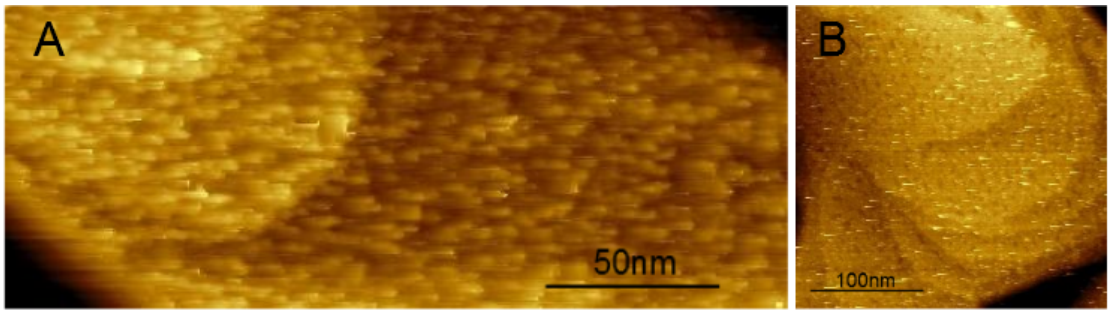

Figure 5.6: A) Scanning tunneling microscopy image of an activated MtrF monolayer on atomically flat Au(111) terraces. Individual MtrF molecules forming a uniform protein monolayer can be resolved. B) Scanning tunneling microscopy image of an MtrF monolayer before activation. The pits seen here are observed as a result of the detergent overlayer blanketing the protein monolayer.

Here we follow the previously reported procedures used in preparation and investigation of single molecules of MtrC and OmcA [61]. However, the availability of the crystal strcuture of MtrF [17], unlike MtrC and OmcA, presents a unique opportunity for comparison between future experimental results that will be obtained using this method and the existing theoretical models that are built upon the knowledge of the MtrF crystal structure.

We report, for the first time, scanning tunneling microscopy measurements on monolayers of *Shewanella*'s outer membrane cytochrome MtrF. Purified MtrF molecules adsorbed on the Au(111) substrate via covalent thiol bonds between the cysteine residues in the tetra-cysteine tag of the protein and the gold surface. This strong bond allows electrons to tunnel from the protein to the gold substrate during STM and TS measurements. Initial scanning of the MtrF monolayer revealed features that were previously observed in MtrC and OmcA monolayers and were referred to as 'pits' [61] (Fig. 5.6B). A second scan of the same area with the tip-substrate bias reversed 'activated' the monolayer. During the activation scan, as

suggested previously with MtrC and OmcA samples [61, 107], the detergent (Octyl β-D-glucopyranoside or OGP) overlayer blanketing the protein monolayer is disrupted enough to open a window for interaction of the STM tip with cytochromes adsorbed on the surface. The detergent overlayer forms in solution when the OGP detergent used to solubilize the cytochromes covers the hydrophobic region of the proteins adsorbed on the surface. After the activation scan, imaging with the initial tip-substrate bias revealed the uniform monolayer of cytochromes and allowed the estimation of single protein dimensions (Fig. 5.6A). Individual cytochromes within the monolayer can be visualized continuously after a one-time activation.

Based on the obtained STM images, we found the lateral dimensions of MtrF molecules to be in the 6 to 9 nm range. Although, the expected distance between heme 5 and 10 in the MtrF crystal strcuture ($\sim$7 nm, [17]) lies in the measured range of MtrF size in our experiment, it is possible that the adsorbed MtrF molecules on the surface were tilted at an agle realtive to the ideal upright position where the heme 5 to heme 10 axis is normal to the substrate surface. This tilt can be explained by the fact that the C-terminus of the protein, where the tetracysteine tag is located, lies closer to the MtrF center and relatively distant from heme 10 [17]. In addition, flexibility of the C-terminal region or the tag as well as partial denaturation of the protein can explain the possible tilting of the protein. The platform developed here has enabled recent STM and tunneling spectroscopy (TS) I-V measurements of individual MtrF molecules [40] that together with the recently reported kinetic Monte Carlo simulations of MtrF conductivity [40] led to a deeper understanding of the basic physics behind electron transport in MtrF.

5.3.3 Nanoscale characterization of the intermediate steps in nanowire formation

The extension of outer membrane filaments, and their functionalization with electron transport proteins, may represent a widespread strategy for EET. Virtually all Gram-negative bacteria produce outer membrane vesicles, and can alter the rate of production and composition of those vesicles in response to various stress conditions [91, 110]. More recent electron microscopy reports describe membrane vesicle chains and related membrane tubes (also referred to as periplasmic tubules) that form cell-cell connections in the social soil bacterium *Myxococcus xanthus* [111] as well as the phototrophic consortium *Chlorochromatium aggregatum* [112]. Consistent with these reports, we observed both a transition from vesicle chains to smoother filaments (Movie S9 in [92]), as well as nanowires connecting separate *Shewanella* cells (Movie S4 in [92]).

To gain a clearer picture of the role of membrane vesicles in *Shewanella* nanowire formation, we performed atomic force microscopy (AFM) on the same bacterial nanowires after observing their growth with fluorescent imaging under perfusion flow conditions. In addition, we imaged bacterial nanowires produced in the *in vivo* imaging platform using transmission electron microscopy (TEM). Such observations were not possible in steady-state chemostat cultures where the nanowire growth is not confined to the surface-solution interface. Perfusion was stopped and the samples were fixed quickly after observing the early signs of nanowire production, allowing us to examine the initial stages of nanowire formation with nanoscale resolution using AFM (Fig. 5.7) and TEM (Fig. 5.8). Using AFM, we measured the nanowires to be 10 nm in diameter under dry conditions, consistent with previous observations [32, 65, 101] and roughly corresponding

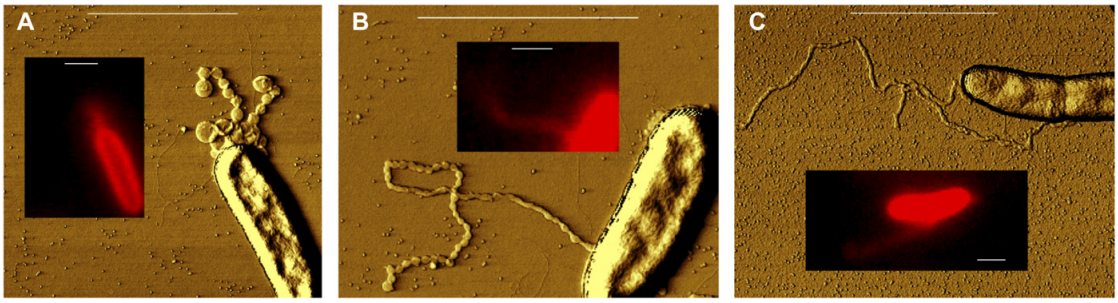

Figure 5.7: Correlated atomic force microscopy (AFM) and live-cell membrane fluorescence of bacterial nanowires. (A-C) Tapping AFM phase images of *S. oneidensis* MR-1 cells after producing bacterial nanowires in the perfusion flow system. The sample is fixed and air-dried before AFM imaging. (Scale bars: 2 μm.) (Insets) In vivo fluorescence images of the same cells/nanowires at the surface/solution interface in the perfusion platform. The cells and the nanowires are stained by the membrane stain FM 4-64FX. (Scale bars: 1 μm.) The morphologies observed range from vesicle chains (A) to partially smooth filaments incorporating vesicles (B), which is consistent with SEM imaging of chemostat samples (Fig. 4.16A), and, finally, continuous filaments (C). See also Movie S9 in [92], which captures the transition from a vesicle chain to a continuous bacterial nanowire.

to two lipid bilayers. In addition, we were able to resolve different morphologies corresponding to different stages of nanowire formation (Fig. 5.7 and Fig. 5.8), consistent with the chain-to-filament transition in Movie S9 in [92]. The morphologies observed ranged from vesicle chains (Fig. 5.7A and Fig. 5.8A and B) to partially smooth filaments incorporating vesicles (Fig. 5.7B, also consistent with SEM imaging in Fig. 4.16A in Chapter 4), and finally continuous filaments (Fig. 5.7C and Fig. 5.8C and D). In addition to possibly mediating EET up to micrometers away from the inner membrane, the vesiculation and extension of outer membranes into the quasi one-dimensional morphologies observed here increase the surface area-to-volume ratio of cells. This shape change can present a significant advantage, increasing the likelihood cells will encounter the solid-phase minerals that serve as electron acceptors for respiration.

5.4 Energy cost calculations of nanowire production

To better understand the energetics involved in the process of nanowire production by a cell, we calculated the free energy necessary to produce a 1-μm long nanowire which includes the free energy of bending the lipid bilayer (cellular outer membrane) into a 1-μm smooth cylinder as well as the energy required to produce the outer membrane cytochromes on the nanowire. The contribution of the former part can be calculated using the expression for the bending energy of lipid bilayer [56]:

$$E_{bend} = \frac{K_b}{2} \int (C_1 + C_2)^2 dA \tag{5.1}$$

where K_b is the bending rigidity of the lipid bilayer and is typically estimated to be around $20\, K_B T$ (K_B being the Boltzmann constant and T temperature in Kelvin) [56], C_1 and C_2 are the two principle curvatures at each point on the surface, and $\int dA$ is taken over the entire surface. Assuming a radius of 10 nm for the filament, calculation of this integral over the surface of a 1-μm cylinder-shaped nanowire gives $\sim 6000\, K_B T$ (or energy of hydrolysis of 300 ATP molecules [56]) as the total requirement for the bending energy. Previous measurements in mid-log cultures of *E. coli* have shown an ATP concentration of $\sim 10^6$ ATPs per cell [113]. Assuming a similar value for ATP concentration in *Shewanella* means that the the above membrane bending energy represents less than $\frac{1}{1000}$th of the cellular ATP budget.

Next, we calculate the cost of production and assembly of the OM cytochromes on nanowires. The average length of MtrC and OmcA is ~ 700 amino acids, and the average energy cost of production and adding an amino acid to the peptide

chain is 5.2 ATPs per amino acid [56]. Therefore, each OM cytochrome costs about 3600 ATP molecules to make. Assuming a single linear chain of OM cytochromes along a 1-μm nanowire (the minimum number of cytochromes to sustain multistep hopping), where each cytochrome is approximately 10 nm long, we can conclude that the nanowire contains a minimum of about 100 OM cytochromes. Multiplying that number by the cost per cytochrome gives an overall cytochrome cost of 3.6×10^5 ATPs, which is 3 orders of magnitude larger than the membrane bending cost to produce the nanowire, and comparable to the cellular ATP content ($\sim 10^6$ ATPs per cell [113]).

5.5 Conclusion

We demonstrated the presence of outer membrane cytochromes MtrC and OmcA along bacterial nanowires, which points to the involvement of cytochromes in nanowire conductivity and to multistep hopping as its underlying mechanism. In addition, we developed an approach to investigate the electronic properties of individual molecules of MtrF, an MtrC homolog, which can be used in the future to build a more comprehensive model of nanowire conductance based on cytochrome-mediated electron transport.

Given the ubiquity of membrane vesicles and related extensions in Gram-negative bacteria, the localization of electron transport proteins along membrane extensions in a manner consistent with bacterial nanowires that could mediate extracellular electron transport, and the finding of nanowire-based cell-cell connectivity, our results raise the intriguing possibility of redox-functionalized membrane extensions as a general microbial strategy for EET and cell-cell signaling. Our study motivates further experimental and theoretical work to build a detailed

understanding of the full biomolecular makeup, electron transport physics, and physiological impact of bacterial nanowires.

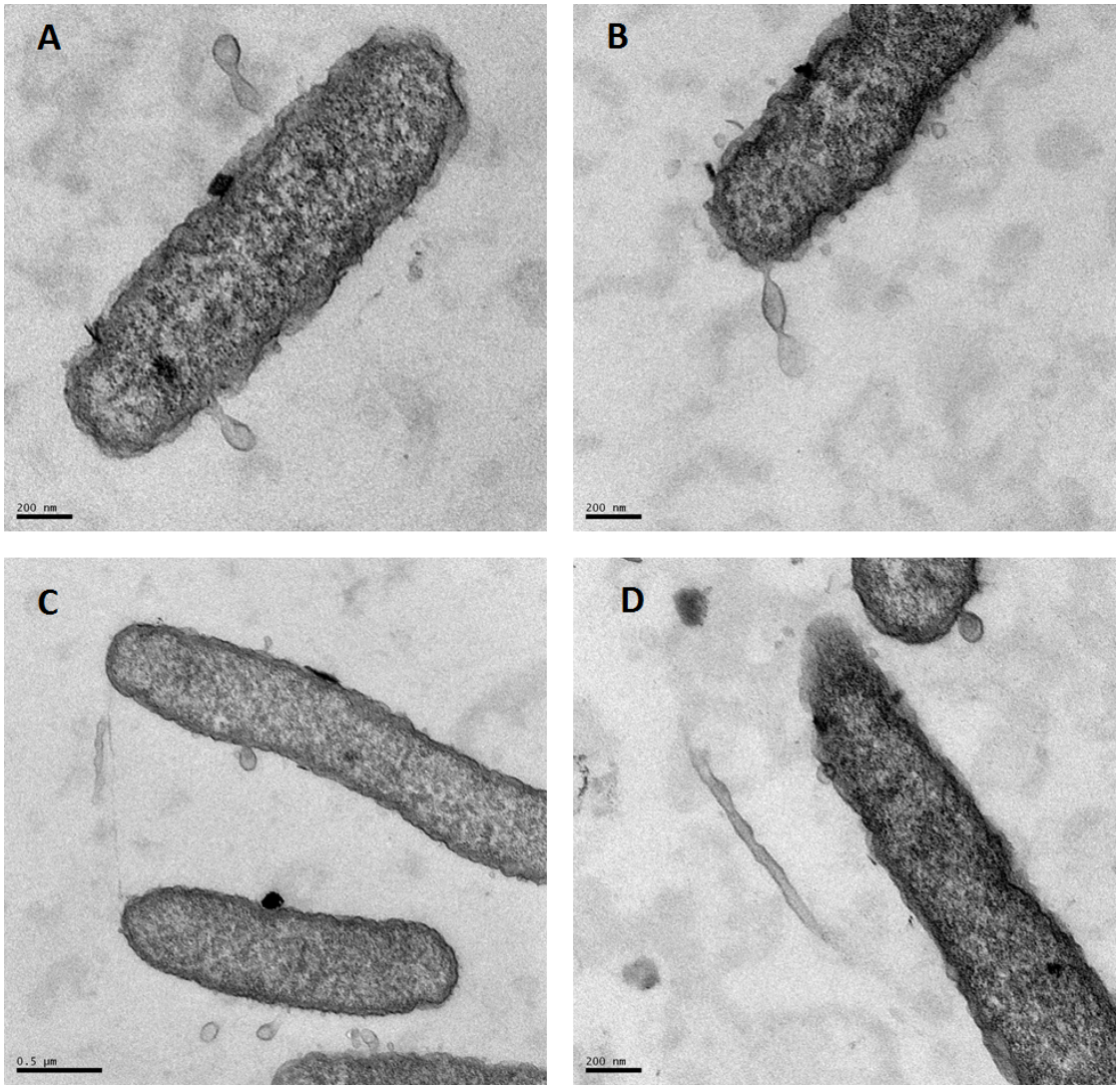

Figure 5.8: Transmission electron microscopy (TEM) images of *S. oneidensis* MR-1 bacterial nanowires produced in the perfusion imaging platform. A and B show nanowires in the form of vesicle chains and C and D demonstrate smoother filaments. The transition from vesicle chains to smooth filaments is also observed both in live fluorescence microscopy and in atomic force microscopy of nanowires.

Chapter 6

Conclusion

Dissimilatory metal reduction in bacteria has been the topic of many studies in the past two decades. The interest in this topic is mainly rooted in the desire for renewable energy recovery using bacteria as well as to gain a better understanding of the global elemental cycles affected by microbes [6, 51]. One of the strategies used by the dissimilatory metal reducing bacteria such as *Shewanella oneidensis* MR-1 to couple their respiration to the reduction of extracellular electron acceptors involves bacterial nanowires [31]. The conductance of bacterial nanowires has been characterized before, although under non-physiological conditions [32, 65]. However, the physical mechanism behind this long-range transport, the compositional and structural properties, and the physiological relevance of nanowires remained elusive until this work. Motivated by these questions, in this thesis we addressed three topics regarding bacterial nanowires.

The first topic concerns the physical mechanism of electron transport along bacterial nanowires which has been the subject of intense debate in the past few years [45]. Some studies have suggested that cytochromes, with their heme groups acting as redox sites, are responsible for mediating long range electron transport in nanowires and biofilms [35, 36], whereas others have described *Geobacter* nanowire electron transport to stem from 'metallic-like' conductivity mediated by stacking of aromatic amino acids along nanowires [47].

In chapter 3, to elucidate the physical nature of electron transport in *Shewanella* nanowires, we developed a theoretical model that aims at describing the results from two separate conductance studies on bacterial nanowires of *S. oneidensis* MR-1 [32, 65]. In addition, it was previously shown that deletion of two outer membrane cytochromes, MtrC and OmcA, from *S. oneidensis* MR-1 results in non-conductive nanowires. Informed by this observation, our proposed model features a chain of redox sites along nanowires, *i.e.* heme groups within outer membrane cytochromes, that mediate the long-range electron transfer along nanowires via a multistep hopping mechanism. As opposed to 'metallic-like' conductivity, the proposed ET mechanism in nanowires of *Geobacter*, multistep hopping involves electrons localizing on each site after every hopping event between two adjacent redox sites along the chain. We found the outcome of this model to match well with the measured conductance (current-voltage $I-V$) curves of *Shewanella* nanowires. Future models informed by the exact structure of outer membrane cytochromes as well as the redox potential of their hemes can motivate further experimental investigations into the electron transfer properties of bacterial nanowires. While the overall data is most consistent with a multistep hopping mechanism, questions still remain about the high electronic couplings measured in experiments compared to the theoretical predictions. This discrepancy motivates the use of new experimental approaches such as spectroscopic measurements in the future to shed more light on the experimental electronic coupling values.

The second topic revolves around fundamental properties of bacterial nanowires that are still unknown, including their composition, structure, and physiological impact. This lack of basic understanding about nanowires was partially caused by the fact that all previous experimental investigations of bacterial nanowires were

performed under non-physiological conditions. In addition, *S. oneidensis* MR-1 nanowires were widely assumed, but never shown, to be type IV pili, proteinaceous filaments that are typically used for cell attachment and twitching motility. This assumption was based on the fact that *Geobacter* nanowires were previously shown to be type IV pili.

In chapter 4, we addressed these issues by developing a platform that, for the first time, allowed us to image *in vivo* growth of nanowires from live *Shewanella* cells. Through staining the structures with fluorescent dyes and localizing the Green Fluorescent Protein (GFP) to the cellular cytoplasm and periplasm, we showed that bacterial nanowires are extenions of the outer membrane that contain periplasm. In addition, using a fluorescent redox activity sensor, we measured an increase in the cellular respiration rate upon production of nanowires, hinting at the physiological impact of these structures.

Our study motivates future work in which, under physiological conditions (*i.e.* in live cells), electron transfer rates through nanowires that connect cells to electrodes are electrochemically measured. This experiment can quantitatively characterize the physiological impact of nanowires on live *Shewanella* cells. In light of our finding that nanowires are outer membrane extensions, it is possible that these structures are also used for molecular transport between cells through the extended periplasm contained within the nanowire structure. Future studies can shed light on this issue, potentially by monitoring *in vivo* transport of fluorescent proteins within nanowires that connect live cells to one another and revealing the exchange of periplasmic content between connected cells.

The third topic of this thesis is about visualization of cytochromes along nanowires as well as nanoscale characterization of these filaments. The role of

cytochromes in *Geobacter* and *Shewanella* nanowire conductivity has been the topic of controversy in recent years [45], mainly due to the alternative proposition of a 'metallic-like' transport mechanism in *Geobacter* nanowires [47] and the finding that the spacing between cytochromes bound to *Geobacter* nanowires is too large to sustain cytochrome-mediated electron transfer along nanowires [114, 115]. However, in *Shewanella*, the deletion of two outer membrane cytochromes MtrC and OmcA from the genome was shown to result in non-conductive nanowires [32].

In chapter 5, to investigate the involvement of cytochromes in nanowire conductance, we stained nanowires produced in our *in vivo* imaging platform with OmcA and MtrC-specific antibodies. Fluorescence microscopy revealed the presence of these two cytochromes along the entire length of bacterial nanowires. Furthermore, nanowires produced from a *Shewanella* strain lacking MtrC and OmcA were not stained by the antibodies. These results point at the possible role of outer membrane cytochromes in nanowire conductivity and are consistent with the proposed multistep hopping mechanism of long-range electron transfer in *Shewanella* nanowires [34]. In addition, in this chapter we demonstrated the development of a method for investigation of electron transfer characteristics of outer membrane cytochromes at the single-molecule level. This information can serve as the building block of a large scale physical model that describes nanowire conductance.

In future work, it would be necessary to examine the exact configuration and spacing between cytochromes along bacterial nanowires. This information will be beneficial in understanding the physics of long-range electron transport in nanowires as well as in building more accurate theoretical models describing this phenomenon.

Shewanella nanowires were previously reported to be smooth, quasi-one-dimensional structures that are about 10 nm in diameter [31, 32]. In light of our finding that nanowires are outer membrane extensions, we examined the dimension and various morphologies of these structures using atomic force microscopy (AFM) and transmission electron microscopy (TEM). Using live fluorescence microscopy, we report the observation of a transition from vesicle chain to smooth filaments during nanowire formation. The different stages of this transition were also captured in the AFM and TEM images.

An intriguing question that remains to be addressed by future studies is about the formation mechanism of bacterial nanowires. The fact that some nanowires initially appear as vesicle chains points at the important role of vesicles in nanowire formation. However, more work is required to elucidate how exactly nanowires are produced by *Shewanella* cells, both at the genetic regulation and biophysical level.

Bibliography

[1] Harry B Gray and Jay R Winkler. Electron flow through metalloproteins. *Biochimica et Biophysica Acta (BBA)-Bioenergetics*, 1797(9):1563–1572, 2010.

[2] R Al Marcus and Norman Sutin. Electron transfers in chemistry and biology. *Biochimica et Biophysica Acta (BBA)-Reviews on Bioenergetics*, 811(3):265–322, 1985.

[3] Peter Mitchell. Coupling of phosphorylation to electron and hydrogen transfer by a chemi-osmotic type of mechanism. *Nature*, 191(4784):144–148, 1961.

[4] Kristopher A Hunt, Jeffrey M Flynn, Belén Naranjo, Indraneel D Shikhare, and Jeffrey A Gralnick. Substrate-level phosphorylation is the primary source of energy conservation during anaerobic respiration of *Shewanella oneidensis* strain MR-1. *Journal of Bacteriology*, 192(13):3345–3351, 2010.

[5] Karrie A Weber, Laurie A Achenbach, and John D Coates. Microorganisms pumping iron: anaerobic microbial iron oxidation and reduction. *Nature Reviews Microbiology*, 4(10):752–764, 2006.

[6] Kenneth H Nealson and Daad Saffarini. Iron and manganese in anaerobic respiration: environmental significance, physiology, and regulation. *Annual Reviews in Microbiology*, 48(1):311–343, 1994.

[7] Derek R Lovley. Dissimilatory metal reduction. *Annual Reviews in Microbiology*, 47(1):263–290, 1993.

[8] Charles R Myers and Kenneth H Nealson. Bacterial manganese reduction and growth with manganese oxide as the sole electron acceptor. *Science*, 240, 1988.

[9] Charles R Myers and Kenneth H Nealson. Respiration-linked proton translocation coupled to anaerobic reduction of manganese (IV) and iron (III) in *Shewanella putrefaciens* MR-1. *Journal of Bacteriology*, 172(11):6232–6238, 1990.

[10] Derek R Lovley and Elizabeth JP Phillips. Novel mode of microbial energy metabolism: organic carbon oxidation coupled to dissimilatory reduction of iron or manganese. *Applied and Environmental Microbiology*, 54(6):1472–1480, 1988.

[11] Charles R Myers and Judith M Myers. Localization of cytochromes to the outer membrane of anaerobically grown *Shewanella putrefaciens* MR-1. *Journal of Bacteriology*, 174(11):3429–3438, 1992.

[12] Judith M Myers and Charles R Myers. Role for outer membrane cytochromes OmcA and OmcB of *Shewanella putrefaciens* MR-1 in reduction of manganese dioxide. *Applied and Environmental Microbiology*, 67(1):260–269, 2001.

[13] CR Myers and JM Myers. Cell surface exposure of the outer membrane cytochromes of *Shewanella oneidensis* MR-1. *Letters in Applied Microbiology*, 37(3):254–258, 2003.

[14] Liang Shi, David J Richardson, Zheming Wang, Sebastien N Kerisit, Kevin M Rosso, John M Zachara, and James K Fredrickson. The roles of outer membrane cytochromes of *Shewanella* and *Geobacter* in extracellular electron transfer. *Environmental Microbiology Reports*, 1(4):220–227, 2009.

[15] Robert S Hartshorne, Catherine L Reardon, Daniel Ross, Jochen Nuester, Thomas A Clarke, Andrew J Gates, Paul C Mills, Jim K Fredrickson, John M Zachara, Liang Shi, et al. Characterization of an electron conduit between bacteria and the extracellular environment. *Proceedings of the National Academy of Sciences*, 106(52):22169–22174, 2009.

[16] Robert S Hartshorne, Brian N Jepson, Tom A Clarke, Sarah J Field, Jim Fredrickson, John Zachara, Liang Shi, Julea N Butt, and David J Richardson. Characterization of *Shewanella oneidensis* MtrC: a cell-surface decaheme cytochrome involved in respiratory electron transport to extracellular electron acceptors. *JBIC Journal of Biological Inorganic Chemistry*, 12(7): 1083–1094, 2007.

[17] Thomas A Clarke, Marcus J Edwards, Andrew J Gates, Andrea Hall, Gaye F White, Justin Bradley, Catherine L Reardon, Liang Shi, Alexander S Beliaev, Matthew J Marshall, et al. Structure of a bacterial cell surface decaheme electron conduit. *Proceedings of the National Academy of Sciences*, 108(23): 9384–9389, 2011.

[18] Gaye F White, Zhi Shi, Liang Shi, Zheming Wang, Alice C Dohnalkova, Matthew J Marshall, James K Fredrickson, John M Zachara, Julea N Butt,

David J Richardson, et al. Rapid electron exchange between surface-exposed bacterial cytochromes and Fe (III) minerals. *Proceedings of the National Academy of Sciences*, 110(16):6346–6351, 2013.

[19] Marian Breuer, Kevin M Rosso, Jochen Blumberger, and Julea N Butt. Multi-haem cytochromes in *Shewanella oneidensis* MR-1: structures, functions and opportunities. *Journal of The Royal Society Interface*, 12(102): 20141117, 2015.

[20] Orianna Bretschger, Anna Obraztsova, Carter A Sturm, In Seop Chang, Yuri A Gorby, Samantha B Reed, David E Culley, Catherine L Reardon, Soumitra Barua, Margaret F Romine, et al. Current production and metal oxide reduction by *Shewanella oneidensis* MR-1 wild type and mutants. *Applied and Environmental Microbiology*, 73(21):7003–7012, 2007.

[21] Leonard M Tender, Clare E Reimers, Hilmar A Stecher, Dawn E Holmes, Daniel R Bond, Daniel A Lowy, Kanoelani Pilobello, Stephanie J Fertig, and Derek R Lovley. Harnessing microbially generated power on the seafloor. *Nature Biotechnology*, 20(8):821–825, 2002.

[22] Kenneth H Nealson, Andrea Belz, and Brent McKee. Breathing metals as a way of life: geobiology in action. *Antonie Van Leeuwenhoek*, 81(1-4):215–222, 2002.

[23] Derek R Lovley, Elizabeth JP Phillips, Yuri A Gorby, and Edward R Landa. Microbial reduction of uranium. *Nature*, 350(6317):413–416, 1991.

[24] Hong Liu, Ramanathan Ramnarayanan, and Bruce E Logan. Production of electricity during wastewater treatment using a single chamber microbial fuel cell. *Environmental Science & Technology*, 38(7):2281–2285, 2004.

[25] Daniel R Bond, Dawn E Holmes, Leonard M Tender, and Derek R Lovley. Electrode-reducing microorganisms that harvest energy from marine sediments. *Science*, 295(5554):483–485, 2002.

[26] Korneel Rabaey and René A Rozendal. Microbial electrosynthesisrevisiting the electrical route for microbial production. *Nature Reviews Microbiology*, 8(10):706–716, 2010.

[27] Kenneth H Nealson and B Lea Cox. Microbial metal-ion reduction and mars: extraterrestrial expectations? *Current opinion in microbiology*, 5(3): 296–300, 2002.

[28] Rudolph A Marcus. On the theory of oxidation-reduction reactions involving electron transfer. I. *The Journal of Chemical Physics*, 24(5):966–978, 1956.

[29] JJ Hopfield. Electron transfer between biological molecules by thermally activated tunneling. *Proceedings of the National Academy of Sciences*, 71(9): 3640–3644, 1974.

[30] Gemma Reguera, Kevin D McCarthy, Teena Mehta, Julie S Nicoll, Mark T Tuominen, and Derek R Lovley. Extracellular electron transfer via microbial nanowires. *Nature*, 435(7045):1098–1101, 2005.

[31] Yuri A Gorby, Svetlana Yanina, Jeffrey S McLean, Kevin M Rosso, Dianne Moyles, Alice Dohnalkova, Terry J Beveridge, In Seop Chang, Byung Hong Kim, Kyung Shik Kim, et al. Electrically conductive bacterial nanowires produced by *Shewanella oneidensis* strain MR-1 and other microorganisms. *Proceedings of the National Academy of Sciences*, 103(30):11358–11363, 2006.

[32] Mohamed Y El-Naggar, Greg Wanger, Kar Man Leung, Thomas D Yuzvinsky, Gordon Southam, Jun Yang, Woon Ming Lau, Kenneth H Nealson, and Yuri A Gorby. Electrical transport along bacterial nanowires from *Shewanella oneidensis* MR-1. *Proceedings of the National Academy of Sciences*, 107(42):18127–18131, 2010.

[33] Christian Pfeffer, Steffen Larsen, Jie Song, Mingdong Dong, Flemming Besenbacher, Rikke Louise Meyer, Kasper Urup Kjeldsen, Lars Schreiber, Yuri A Gorby, Mohamed Y El-Naggar, et al. Filamentous bacteria transport electrons over centimetre distances. *Nature*, 491(7423):218–221, 2012.

[34] Sahand Pirbadian and Mohamed Y El-Naggar. Multistep hopping and extracellular charge transfer in microbial redox chains. *Physical Chemistry Chemical Physics*, 14(40):13802–13808, 2012.

[35] Sarah M Strycharz-Glaven, Rachel M Snider, Anthony Guiseppi-Elie, and Leonard M Tender. On the electrical conductivity of microbial nanowires and biofilms. *Energy & Environmental Science*, 4(11):4366–4379, 2011.

[36] Nicholas F Polizzi, Spiros S Skourtis, and David N Beratan. Physical constraints on charge transport through bacterial nanowires. *Faraday discussions*, 155:43–61, 2012.

[37] Marian Breuer, Piotr Zarzycki, Jochen Blumberger, and Kevin M Rosso. Thermodynamics of electron flow in the bacterial deca-heme cytochrome MtrF. *Journal of the American Chemical Society*, 134(24):9868–9871, 2012.

[38] Marian Breuer, Piotr Zarzycki, Liang Shi, ThomasA Clarke, MarcusJ Edwards, JuleaN Butt, DavidJ Richardson, JamesK Fredrickson, JohnM Zachara, Jochen Blumberger, et al. Molecular structure and free energy

landscape for electron transport in the decahaem cytochrome MtrF. *Biochemical Society Transactions*, 40(6):1198, 2012.

[39] Marian Breuer, Kevin M Rosso, and Jochen Blumberger. Electron flow in multiheme bacterial cytochromes is a balancing act between heme electronic interaction and redox potentials. *Proceedings of the National Academy of Sciences*, 111(2):611–616, 2014.

[40] Hye Suk Byun, Sahand Pirbadian, Aiichiro Nakano, Liang Shi, and Mohamed Y El-Naggar. Kinetic Monte Carlo simulations and molecular conductance measurements of the bacterial decaheme cytochrome MtrF. *ChemElectroChem*, 1(11):1932–1939, 2014.

[41] Dianne K Newman and Roberto Kolter. A role for excreted quinones in extracellular electron transfer. *Nature*, 405(6782):94–97, 2000.

[42] Enrico Marsili, Daniel B Baron, Indraneel D Shikhare, Dan Coursolle, Jeffrey A Gralnick, and Daniel R Bond. *Shewanella* secretes flavins that mediate extracellular electron transfer. *Proceedings of the National Academy of Sciences*, 105(10):3968–3973, 2008.

[43] Nicholas J Kotloski and Jeffrey A Gralnick. Flavin electron shuttles dominate extracellular electron transfer by *Shewanella oneidensis*. *MBio*, 4(1):e00553–12, 2013.

[44] Thomas Boesen and Lars Peter Nielsen. Molecular dissection of bacterial nanowires. *Mbio*, 4(3):e00270–13, 2013.

[45] Sarah M Strycharz-Glaven and Leonard M Tender. Reply to the comment on on electrical conductivity of microbial nanowires and biofilmsby NS Malvankar, MT Tuominen and DR Lovley, Energy Environ. Sci., 2012, 5, doi: 10.1039/c2ee02613a. *Energy & Environmental Science*, 5(3):6250–6255, 2012.

[46] Nikhil S Malvankar and Derek R Lovley. Microbial nanowires for bioenergy applications. *Current Opinion in Biotechnology*, 27:88–95, 2014.

[47] Nikhil S Malvankar, Madeline Vargas, Kelly P Nevin, Ashley E Franks, Ching Leang, Byoung-Chan Kim, Kengo Inoue, Tünde Mester, Sean F Covalla, Jessica P Johnson, et al. Tunable metallic-like conductivity in microbial nanowire networks. *Nature Nanotechnology*, 6(9):573–579, 2011.

[48] Marina G Kalyuzhnaya, Mary E Lidstrom, and Ludmila Chistoserdova. Real-time detection of actively metabolizing microbes by redox sensing as applied to methylotroph populations in Lake Washington. *The ISME journal*, 2(7): 696–706, 2008.

[49] D Gray, RS Yue, Ching-Ying Chueng, and William Godfrey. Bacterial vitality detected by a novel fluorogenic redox dye using flow cytometry. In *American Society of Microbiology Meeting: Washington, DC, USA*, 2005.

[50] Bruce E Logan. Exoelectrogenic bacteria that power microbial fuel cells. *Nature Reviews Microbiology*, 7(5):375–381, 2009.

[51] Bruce E Logan and John M Regan. Microbial fuel cells-challenges and applications. *Environmental Science & Technology*, 40(17):5172–5180, 2006.

[52] Parish P Sedghizadeh, Satish KS Kumar, Amita Gorur, Christoph Schaudinn, Charles F Shuler, and J William Costerton. Microbial biofilms in osteomyelitis of the jaw and osteonecrosis of the jaw secondary to bisphosphonate therapy. *The Journal of the American Dental Association*, 140(10): 1259–1265, 2009.

[53] Greg Wanger, Yuri Gorby, Mohamed Y El-Naggar, Thomas D Yuzvinsky, Christoph Schaudinn, Amita Gorur, and Parish P Sedghizadeh. Electrically conductive bacterial nanowires in bisphosphonate-related osteonecrosis of the jaw biofilms. *Oral surgery, oral medicine, oral pathology and oral radiology*, 115(1):71–78, 2013.

[54] Erwin Schrodinger and Lewin. *What is life?* University Press, 1967.

[55] Koscak Maruyama. The discovery of adenosine triphosphate and the establishment of its structure. *Journal of the History of Biology*, 24(1):145–154, 1991.

[56] Rob Phillips, Jane Kondev, Julie Theriot, and Hernan Garcia. *Physical biology of the cell*. Garland Science, 2012.

[57] Rudolf K Thauer, Kurt Jungermann, and Karl Decker. Energy conservation in chemotrophic anaerobic bacteria. *Bacteriological Reviews*, 41(1):100, 1977.

[58] Mohamed Y El-Naggar and Steven E Finkel. Live wires. *The Scientist*, 27 (5):38–43, 2013.

[59] David J Richardson, Julea N Butt, Jim K Fredrickson, John M Zachara, Liang Shi, Marcus J Edwards, Gaye White, Nanakow Baiden, Andrew J Gates, Sophie J Marritt, et al. The porin–cytochrome model for microbe-to-mineral electron transfer. *Molecular Microbiology*, 85(2):201–212, 2012.

[60] Dan Coursolle, Daniel B Baron, Daniel R Bond, and Jeffrey A Gralnick. The Mtr respiratory pathway is essential for reducing flavins and electrodes in *Shewanella oneidensis*. *Journal of bacteriology*, 192(2):467–474, 2010.

[61] Nicholas S Wigginton, Kevin M Rosso, Brian H Lower, Liang Shi, and Michael F Hochella. Electron tunneling properties of outer-membrane decaheme cytochromes from *Shewanella oneidensis*. *Geochimica et cosmochimica acta*, 71(3):543–555, 2007.

[62] Gerd Binnig, Calvin F Quate, and Ch Gerber. Atomic force microscope. *Physical Review Letters*, 56(9):930, 1986.

[63] Gerd Binnig and Heinrich Rohrer. Scanning tunneling microscopy. *IBM Journal of research and development*, 44(1-2):279–293, 2000.

[64] Souichiro Kato, Kazuhito Hashimoto, and Kazuya Watanabe. Microbial interspecies electron transfer via electric currents through conductive minerals. *Proceedings of the National Academy of Sciences*, 109(25):10042–10046, 2012.

[65] Mohamed Y El-Naggar, Yuri A Gorby, Wei Xia, and Kenneth H Nealson. The molecular density of states in bacterial nanowires. *Biophysical Journal*, 95(1):L10–L12, 2008.

[66] H Liu, GJ Newton, R Nakamura, K Hashimoto, and S Nakanishi. Electrochemical characterization of a single electricity-producing bacterial cell of *Shewanella* by using optical tweezers. *Angewandte Chemie (International ed. in English)*, 49(37):6596–6599, 2010.

[67] Lucius S Fox, Mariusz Kozik, Jay R Winkler, and Harry B Gray. Gaussian free-energy dependence of electron-transfer rates in iridium complexes. *Science*, 247(4946):1069–1071, 1990.

[68] Michael R Wasielewski, Mark P Niemczyk, Walter A Svec, and E Bradley Pewitt. Dependence of rate constants for photoinduced charge separation and dark charge recombination on the free energy of reaction in restricted-distance porphyrin-quinone molecules. *Journal of the American Chemical Society*, 107(4):1080–1082, 1985.

[69] Christopher ED Chidsey. Free energy and temperature dependence of electron transfer at the metal-electrolyte interface. *Science*, 251(4996):919–922, 1991.

[70] Laurie J Jones, Richard P Haugland, and Victoria L Singer. Development and characterization of the nanoorange® protein quantitation assay: A fluorescence-based assay of proteins in solution. *BioTechniques*, 34(4):850–861, 2003.

[71] Hans-Peter Grossart, Grieg F Steward, Josefina Martinez, and Farooq Azam. A simple, rapid method for demonstrating bacterial flagella. *Applied and Environmental Microbiology*, 66(8):3632–3636, 2000.

[72] William J Betz, Fei Mao, and Corey B Smith. Imaging exocytosis and endocytosis. *Current opinion in neurobiology*, 6(3):365–371, 1996.

[73] S Bolte, C Talbot, Y Boutte, O Catrice, ND Read, and B Satiat-Jeunemaitre. FM-dyes as experimental probes for dissecting vesicle trafficking in living plant cells. *Journal of Microscopy*, 214(2):159–173, 2004.

[74] LR Griffing. FRET analysis of transmembrane flipping of FM4–64 in plant cells: is FM4–64 a robust marker for endocytosis? *Journal of microscopy*, 231(2):291–298, 2008.

[75] Valentina Rosu and Kelly T Hughes. σ28-dependent transcription in *Salmonella enterica* is independent of flagellar shearing. *Journal of Bacteriology*, 188(14):5196–5203, 2006.

[76] Kris M Blair, Linda Turner, Jared T Winkelman, Howard C Berg, and Daniel B Kearns. A molecular clutch disables flagella in the *Bacillus subtilis* biofilm. *Science*, 320(5883):1636–1638, 2008.

[77] Andrew C Lowenthal, Marla Hill, Laura K Sycuro, Khalid Mehmood, Nina R Salama, and Karen M Ottemann. Functional analysis of the *Helicobacter pylori* flagellar switch proteins. *Journal of bacteriology*, 191(23):7147–7156, 2009.

[78] Dena L Cologgi, Sanela Lampa-Pastirk, Allison M Speers, Shelly D Kelly, and Gemma Reguera. Extracellular reduction of uranium via *Geobacter* conductive pili as a protective cellular mechanism. *Proceedings of the National Academy of Sciences*, 108(37):15248–15252, 2011.

[79] Ian D Odell and Deborah Cook. Immunofluorescence techniques. *Journal of Investigative Dermatology*, 133(1):e4, 2013.

[80] Harry B Gray and Jay R Winkler. Electron tunneling through proteins. *Quarterly Reviews of Biophysics*, 36(03):341–372, 2003.

[81] George A Kowalchuk, Susan E Jones, and Linda L Blackall. Microbes orchestrate life on earth. *The ISME Journal*, 2(8):795–796, 2008.

[82] Harald Von Canstein, Jun Ogawa, Sakayu Shimizu, and Jonathan R Lloyd. Secretion of flavins by *Shewanella* species and their role in extracellular electron transfer. *Applied and environmental microbiology*, 74(3):615–623, 2008.

[83] Rachel M Snider, Sarah M Strycharz-Glaven, Stanislav D Tsoi, Jeffrey S Erickson, and Leonard M Tender. Long-range electron transport in *Geobacter sulfurreducens* biofilms is redox gradient-driven. *Proceedings of the National Academy of Sciences*, 109(38):15467–15472, 2012.

[84] Ferdinand C Grozema and Laurens DA Siebbeles. Mechanism of charge transport in self-organizing organic materials. *International Reviews in Physical Chemistry*, 27(1):87–138, 2008.

[85] Alessandro Troisi. The speed limit for sequential charge hopping in molecular materials. *Organic Electronics*, 12(12):1988–1991, 2011.

[86] James C Bellowsa and Paras N Prasadb. Dephasing times and linewidths of optical transitions in molecular crystals. Temperature dependence of line shapes, linewidths, and frequencies of Raman active phonons in naphthalene. *The Journal of Chemical Physics*, 70(4):1864–1871, 1979.

[87] Aleksandr M Kuznetsov, Peter Sommer-Larsen, and Jens Ulstrup. Resonance and environmental fluctuation effects in STM currents through large adsorbed molecules. *Surface science*, 275(1):52–64, 1992.

[88] Carlo Augusto Bortolotti, Magdalena E Siwko, Elena Castellini, Antonio Ranieri, Marco Sola, and Stefano Corni. The reorganization energy in cytochrome c is controlled by the accessibility of the heme to the solvent. *The Journal of Physical Chemistry Letters*, 2(14):1761–1765, 2011.

[89] Stefano Corni. The reorganization energy of azurin in bulk solution and in the electrochemical scanning tunneling microscopy setup. *The Journal of Physical Chemistry B*, 109(8):3423–3430, 2005.

[90] Madeline Vargas, Nikhil S Malvankar, Pier-Luc Tremblay, Ching Leang, Jessica A Smith, Pranav Patel, Oona Synoeyenbos-West, Kelly P Nevin, and Derek R Lovley. Aromatic amino acids required for pili conductivity and long-range extracellular electron transport in *Geobacter sulfurreducens*. *MBio*, 4(2):e00105–13, 2013.

[91] Y Gorby, J McLean, A Korenevsky, K Rosso, Mohamed Y El-Naggar, and Terrance J Beveridge. Redox-reactive membrane vesicles produced by *Shewanella*. *Geobiology*, 6(3):232–241, 2008.

[92] Sahand Pirbadian, Sarah E Barchinger, Kar Man Leung, Hye Suk Byun, Yamini Jangir, Rachida A Bouhenni, Samantha B Reed, Margaret F Romine, Daad A Saffarini, Liang Shi, et al. *Shewanella oneidensis* MR-1 nanowires are outer membrane and periplasmic extensions of the extracellular electron

transport components. *Proceedings of the National Academy of Sciences*, 111 (35):12883–12888, 2014.

[93] Rachida A Bouhenni, Gary J Vora, Justin C Biffinger, Sheetal Shirodkar, Ken Brockman, Ricky Ray, Peter Wu, Brandy J Johnson, Eulandria M Biddle, Matthew J Marshall, et al. The role of *Shewanella oneidensis* MR-1 outer surface structures in extracellular electron transfer. *Electroanalysis*, 22 (7-8):856–864, 2010.

[94] Qixia Luo, Yangyang Dong, Haijiang Chen, and Haichun Gao. Mislocalization of rieske protein PetA predominantly accounts for the aerobic growth defect of Tat mutants in *Shewanella oneidensis*. *PloS one*, 8(4):e62064, 2013.

[95] Ann G Matthysse, Serina Stretton, Catherine Dandie, Nicholas C McClure, and Amanda E Goodman. Construction of GFP vectors for use in Gram-negative bacteria other than *Escherichia coli*. *FEMS microbiology letters*, 145(1):87–94, 1996.

[96] Jeffrey S McLean, Greg Wanger, Yuri A Gorby, Martin Wainstein, Jeff McQuaid, Shunichi Ishii, Orianna Bretschger, Haluk Beyenal, and Kenneth H Nealson. Quantification of electron transfer rates to a solid phase electron acceptor through the stages of biofilm formation from single cells to multicellular communities. *Environmental Science & Technology*, 44(7): 2721–2727, 2010.

[97] William G Miller, Johan HJ Leveau, and Steven E Lindow. Improved *gfp* and *inaZ* broad-host-range promoter-probe vectors. *Molecular Plant-Microbe Interactions*, 13(11):1243–1250, 2000.

[98] In Seop Chang, Hyunsoo Moon, Orianna Bretschger, Jae Kyung Jang, Ho Il Park, Kenneth H Nealson, and Byung Hong Kim. Electrochemically active bacteria (EAB) and mediator-less microbial fuel cells. *J Microbiol Biotechnol*, 16(2):163–177, 2006.

[99] VA Rhodius and CA Gross. Using DNA microarrays to assay part function. *Methods in enzymology*, 497:75–113, 2010.

[100] Kar Man Leung, Greg Wanger, Qiuquan Guo, Yuri Gorby, Gordon Southam, Woon Ming Lau, and Jun Yang. Bacterial nanowires: conductive as silicon, soft as polymer. *Soft Matter*, 7(14):6617–6621, 2011.

[101] Kar Man Leung, Greg Wanger, Mohamed Y El-Naggar, Yuri Gorby, Gordon Southam, Woon Ming Lau, and Jun Yang. *Shewanella oneidensis* MR-1 bacterial nanowires exhibit p-type, tunable electronic behavior. *Nano Letters*, 13(6):2407–2411, 2013.

[102] Jeffrey A Gralnick, Hojatollah Vali, Douglas P Lies, and Dianne K Newman. Extracellular respiration of dimethyl sulfoxide by *Shewanella oneidensis* strain MR-1. *Proceedings of the National Academy of Sciences of the United States of America*, 103(12):4669–4674, 2006.

[103] Erinn C Howard, Emily R Petersen, Lisa A Fitzgerald, Paul E Sheehan, and Bradley R Ringeisen. Optimal method for efficiently removing extracellular nanofilaments from *Shewanella oneidensis* MR-1. *Journal of microbiological methods*, 87(3):320–324, 2011.

[104] Catherine L Reardon, AC Dohnalkova, Ponnusamy Nachimuthu, David W Kennedy, DA Saffarini, Bruce W Arey, Liang Shi, Zheming Wang, D Moore, Jeffrey S Mclean, et al. Role of outer-membrane cytochromes MtrC and OmcA in the biomineralization of ferrihydrite by *Shewanella oneidensis* MR-1. *Geobiology*, 8(1):56–68, 2010.

[105] Liang Shi, Baowei Chen, Zheming Wang, Dwayne A Elias, M Uljana Mayer, Yuri A Gorby, Shuison Ni, Brian H Lower, David W Kennedy, David S Wunschel, et al. Isolation of a high-affinity functional protein complex between OmcA and MtrC: two outer membrane decaheme c-type cytochromes of *Shewanella oneidensis* MR-1. *Journal of Bacteriology*, 188(13):4705–4714, 2006.

[106] Liang Shi, Jiann-Trzwo Lin, Lye M Markillie, Thomas C Squier, and Brian S Hooker. Overexpression of multi-heme c-type cytochromes. *Biotechniques*, 38:297–299, 2005.

[107] Nicholas S Wigginton, Kevin M Rosso, and Michael F Hochella. Mechanisms of electron transfer in two decaheme cytochromes from a metal-reducing bacterium. *The Journal of Physical Chemistry B*, 111(44):12857–12864, 2007.

[108] Edward S Reynolds. The use of lead citrate at high ph as an electron-opaque stain in electron microscopy. *The Journal of Cell Biology*, 17(1):208–212, 1963.

[109] John H Venable and Richard Coggeshall. A simplified lead citrate stain for use in electron microscopy. *The Journal of Cell Biology*, 25(2):407–408, 1965.

[110] Adam Kulp and Meta J Kuehn. Biological functions and biogenesis of secreted bacterial outer membrane vesicles. *Annual Review of Microbiology*, 64:163, 2010.

[111] Jonathan P Remis, Dongguang Wei, Amita Gorur, Marcin Zemla, Jessica Haraga, Simon Allen, H Ewa Witkowska, J William Costerton, James E

Berleman, and Manfred Auer. Bacterial social networks: structure and composition of *Myxococcus xanthus* outer membrane vesicle chains. *Environmental Microbiology*, 16(2):598–610, 2014.

[112] Gerhard Wanner, Kajetan Vogl, and Jörg Overmann. Ultrastructural characterization of the prokaryotic symbiosis in *Chlorochromatium aggregatum*. *Journal of Bacteriology*, 190(10):3721–3730, 2008.

[113] Michael H Buckstein, Jian He, and Harvey Rubin. Characterization of nucleotide pools as a function of physiological state in *Escherichia coli*. *Journal of bacteriology*, 190(2):718–726, 2008.

[114] Ching Leang, Xinlei Qian, Tünde Mester, and Derek R Lovley. Alignment of the c-type cytochrome OmcS along pili of *Geobacter sulfurreducens*. *Applied and Environmental Microbiology*, 76(12):4080–4084, 2010.

[115] Nikhil S Malvankar, Mark T Tuominen, and Derek R Lovley. Lack of cytochrome involvement in long-range electron transport through conductive biofilms and nanowires of *Geobacter sulfurreducens*. *Energy & Environmental Science*, 5(9):8651–8659, 2012.